SPATIAL FIELD CONTROL OF BROAD AREA SEMICONDUCTOR LASERS WITH INTEGRATED GRATING COUPLERS

by

Viktor Olegovich Smolski

A dissertation submitted to the faculty of
The University of North Carolina at Charlotte
in partial fulfillment of the requirements
for the degree of Doctor of Philosophy in
Electrical Engineering

Charlotte

2012

Approved by:

_____
Dr. Eric G. Johnson

_____
Dr. Edward Stokes

_____
Dr. Michael A. Fiddy

_____
Dr. Glenn Boreman

_____
Dr. Ian Ferguson

_____
Dr. Maciej Noras

DISCLAIMER

ABSTRACT

In this research, a method of designing a grating outcoupler to obtain the desired 2D-intensity profile and improved field distribution of the optical beam emitted by a grating coupled surface emitting laser is presented. The method is based on variation of the periodicity, duty cycle, and the groove tilt angle of the grating. Grating design involves numerical analysis of the optical field propagated through the grating, by applying the Rigorous Coupled Wave Approach method. Experimental evaluation of the designed grating components was done by fabrication and testing the broad area semiconductor lasers with the monolithically integrated grating outcouplers. Another grating design is presented that provides the spreading of a single optical output into multi-beams at different outcoupling angles in the emitting plane. Using field distribution presentation, an approach to provide uniform optical intensity profile from the grating outcoupler based on varying duty cycle is described.

Furthermore, this work presents experimental evaluation of 1D, and 2D (8x8) square, arrays of phase-locked surface-emitters including semiconductor optical amplifiers spaced by grating outcouplers. The phase-locked multi-emitter design was based on the master oscillator power amplifier (MOPA) array approach. As the MO for the 1D array we used a monolithically integrated grating coupled laser with wavelength stabilization and a fiber coupled external laser source was used for the 2D array. Mutual coherence was experimentally evaluated by interference investigation and the obtained results were compared to numerical modeling.

DEDICATION

To my family, friends and coworkers for their support throughout my graduate school

journey.

ACKNOWLEDGEMENTS

TABLE OF CONTENTS

LIST OF ABBREVIATIONS

ASE	Amplified Spontaneous Emission
AR	Antireflection
CCD	Charge-Coupled Device
COMD	Catastrophic optical mirror damage
CW	Continuous Wave
DI	Deionized
DE	Diffraction Efficiency
dB	Decibels DOE Diffractive Optical Element
DBR	Double Bragg Reflector
DFB	Distributed Feedback
DGR	Dual Grating Reflector
DH	Double Heterostructure
DQE	Differential Quantum Efficiency
EBPG	Electron Beam Pattern Generator
ECR	Electron Cyclotron Resonance
FF	Far Field
FP	Fabry-Perrot
FD-BPM	Finite Difference Beam Propagation Method
FDTD	Finite Difference Time Domain
FIB	Focused Ion Beam FP Fabry-Perot
FWHM	Full Width Half Maximum

GCSEL	Grating-coupled Surface Emitting Laser
GCSOA	Grating-Coupled Semiconductor Optical Amplifier
GRINSCH	Graded index separate confinement heterostructure
HR	High Reflection
ICP	Inductively-Coupled Plasma
IPA	Isopropanol
LOC	Large Optical Cavity
MOPA	Master Oscillator Power Amplifier
NF	Near Field
NPGS	Nabity Pattern Generator System
OSA	Optical Spectrum Analyzer
PML	Perfectly Matched Layer
RCWA	Rigorous Coupled Wave Analysis
SQW	Single Quantum Well
SQW-GRINSCH	Single Quantum Well Grating Refractive Index Separate Confinement Heterostructure
TE	Transverse Electric
TEC	Thermo-Electric Cooler
TIR	Total Internal Reflection
VCSEL	Vertical-Cavity Surface-Emitting Laser
QCW	Quasi-Continuous Wave

CHAPTER 1: INTRODUCTION

The first reported coherent light emission from a semiconductor laser was in 1962 by group from General Electric led by Robert N. Hall (Hall et al. 1962) and a little later IBM T.J. Watson Research Center's Marshall Nathan (Nathan et al. 1962). Although theoretical understanding was already in place, it was not until 1970's that a continuous wave operation was demonstrated in a double heterojunction structure. Achievement of a continuous lasing in lasers with stripe geometry was reported by Zhores Alferov et al. (Alferov et al. 1970) and in independent work reported shortly after by Izuyo Hayashi et al. (Hayashi et al. 1970). Such success is a part of both: great physicist's mastermind and a sufficient technological progress in fabrication.

Semiconductor Laser technology has been around for half a century and has proven to be extremely useful in modern day electronics. Just to list a few these are telecommunications, scanners, readers, pointers, CD, DVD, material processes etc. Moreover, an emerging applications field is laser medicine.

At first, the construction of an efficient emitter was considered as almost impossible. With progress of deposition techniques such as vapor-phase epitaxy (VPE), liquid-phase epitaxy (LTE), molecular beam epitaxy (MBE), MOCVD etc, first results proved otherwise (Alferov et al. 1967). As mentioned before, double heterojunctions (DH) are advantageous due to operation in the CW conditions by significant increased efficiency of stimulated radiative recombination in semiconductor-based structure. To build a double heterostructure many conditions have to be met with the right thermal,

electrical, crystal properties and band structures. Mainly, the material pair had to be at closest proximity of the lattice constants, however electrical and optical properties may be different. Most promising pairs studied at first were AlAs-GaAs with further advancement to $Al_xGa_{1-x}As$-GaAs materials. It was demonstrated by Alferov (Alferov et al. 1970) and also later by Antipas (Antipas et al. 1973) that III-V material solutions are suitable for variation of bandgap widths. Current popular compound combinations and trends are in III-V, II-IV, II-VI and IV-VI heterostructures such as AlGaAs-GaAs, InGaAs-GaAs, InGaN-GaN and more.

General knowledge of Semiconductor Lasers consists of understanding several fundamental ideas of operation. Such are optical gain, optical resonators, waveguide, followed by characterization in terms of lasing threshold, light-current, voltage-current, spectral characteristics, emission profile, etc.

This work presented herein will incorporate the use of Grating Coupled Surface Emitting Lasers (GCSELs). Beam outcoupling properties of such are explored with advanced designs for beam formation, focusing, mode discrimination and other methods highly interesting in further research.

1.1 Semiconductor Lasers

The electronic states of crystals form energy bands. Active material consists of two energy levels – conduction and valence bands. In the lower energy bandgap of the material, electrons are trapped in the conduction band whereas holes are trapped in the valence band. Figure 1.1 demonstrates a direct bandgap energy band of semiconductors used for optoelectronic devices. This is where the lower energy level of the conduction band and the higher energy level of the valence band are at the Γ-point or the center of

the Brillouin zone. In this case process of radiation recombination, responsible for optical gain, is most efficient.
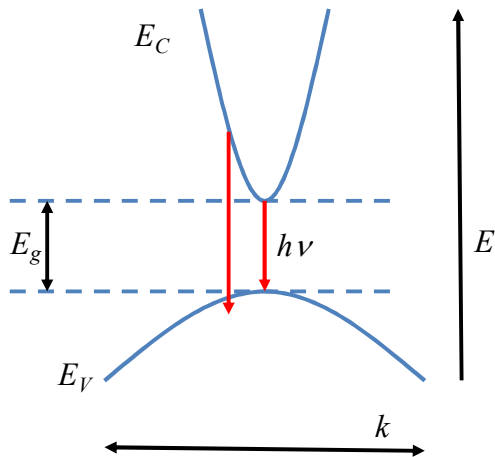
Figure 1.1 Carrier energy Band Structure of a direct bandgap semiconductor

Optical gain in the semiconductor is based on stimulated emission caused by radiative recombination of electron-hole pairs emitting a photon. The energy of the generated photon corresponds to the difference in two energy levels. Therefore the wavelength of semiconductor lasers is determined by the bandgap size. Under stimulated emission the photons have same properties of frequency, direction, phase and polarization.

For efficient transfer electrical current driven through semiconductor laser, a structure consisted p-n junction is normally used. Energy band diagram of p-n homojunction is illustrated in figure 1.2. Applying voltage across the p-n diode, electrons and holes begin flowing to the p-n junction, causing population inversion. The optical gain is generated in the junction area. Electron – hole radiative recombination then provides the photon emission, or light.
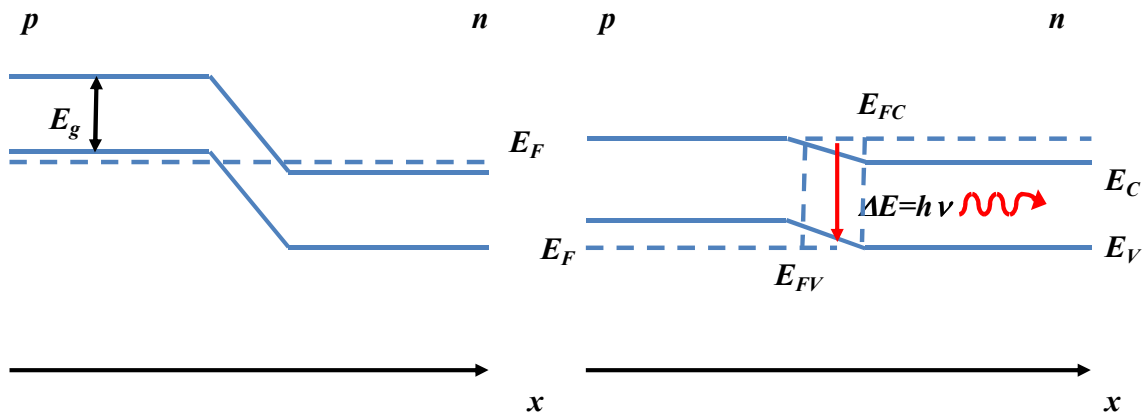
Figure 1.2 Energy band diagram of a p-i-n junction. a) under no bias (V=0) b) under forward bias V=hv/q

Another important parameter to take into account is that there's little to no efficiency of recombination in just a simple p-n homojunction. To improve the carrier's confinement and so it's recombination efficiency, heterostructures must be used. Therefore extensive research was performed to improve this performance and a double heterostructures (DH) were introduced with addition of epitaxial growth and lower band gap materials. Heterostructure consists of materials with different energy bandgap, such as AlGaAs with wide gap and GaAs with narrow gap. Figure 1.3 (a) shows band diagram for p-n junction involved the heterostructure. Since energy barriers formed on heterojunctions, the carriers are trapped inside a narrow band-gap material, called carrier confinement. Biasing the device allows a high carrier (electrons and holes) density at the p-n junction region, called superinjection. Along with the carrier confinement, optical confinement is present due to refractive index profile creating a waveguide in transverse direction for the DH increasing total optical gain of active medium, Figure 1.3 (b). So, the heterostructures are advantageous due to three common interests: continuous

superinjection of carriers, carrier confinement (electron and hole), and optical confinement in transverse direction. Further intensive research in the field resulted in advanced semiconductor-based active media included quantum wells. The effect of trapping the carrier in very narrow QW layer results in more efficient radiative recombination and so higher gain. Such structure, in which carries and optical filed are confined in different layers, accordingly in QW and in waveguide, usually called a Separate Confinement Heterostructure (SCH).
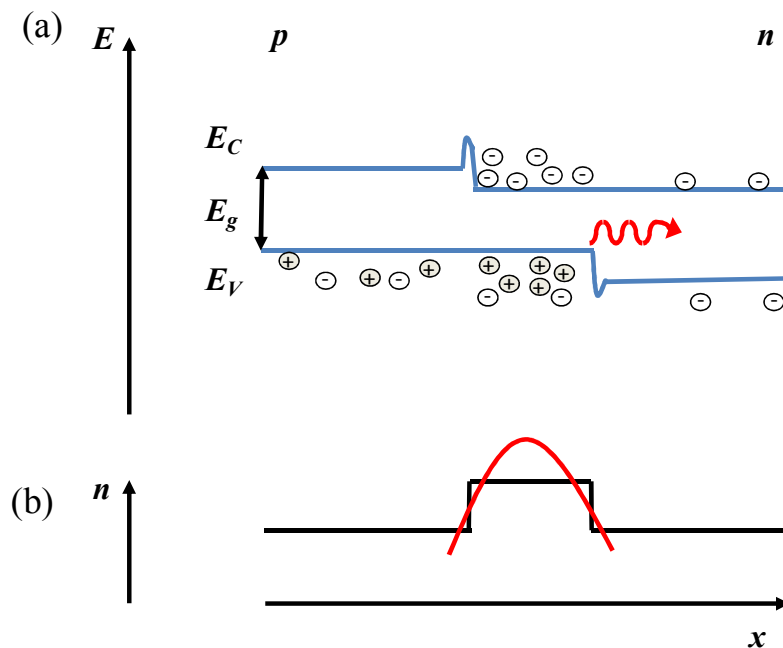
Figure 1.3. (a) Band Diagram of the DH structure creating electrical confinement (b) refractive index profile of DH creating optical confinement

Diode lasers designs separated by two principals: in-plane cavities and vertical cavity. Figure 1.4 shows the in-plane, edge-emitting type of the device that serves the base of the work presented here. The device consists of a GaAs n-substrate, followed by epitaxially grown n-$Al_xGa_{1-x}As$ cladding, Single Quantum Well $In_xGa_{1-x}As$ inside GaAs

waveguide, p-Al$_x$Ga$_{1-x}$As cladding, p+-GaAs, surrounded by p- and n- side contacts. Such design requires lateral confinement for a practical laser operation to satisfy emission in a narrow beam. Multiple lateral confinement methods are possible, example illustrated involves a wet/dry etch of the p-cladding layer and use of silicon nitride layer (SiN) serving as an insulating layer.

100μm

metal p-contact
dielectric (SiN)
p+-GaAs (~0.2μm)
p-Al$_x$Ga$_{1-x}$As (~1μm)
WG GaAs (~0.4μm)
SQW In$_x$Ga$_{1-x}$As (8nm)
n-Al$_x$Ga$_{1-x}$As (~1μm)
n-GaAs (~150μm)
metal n-contact

1mm
500μm
cleaved facet (HR)
cleaved facet (AR)
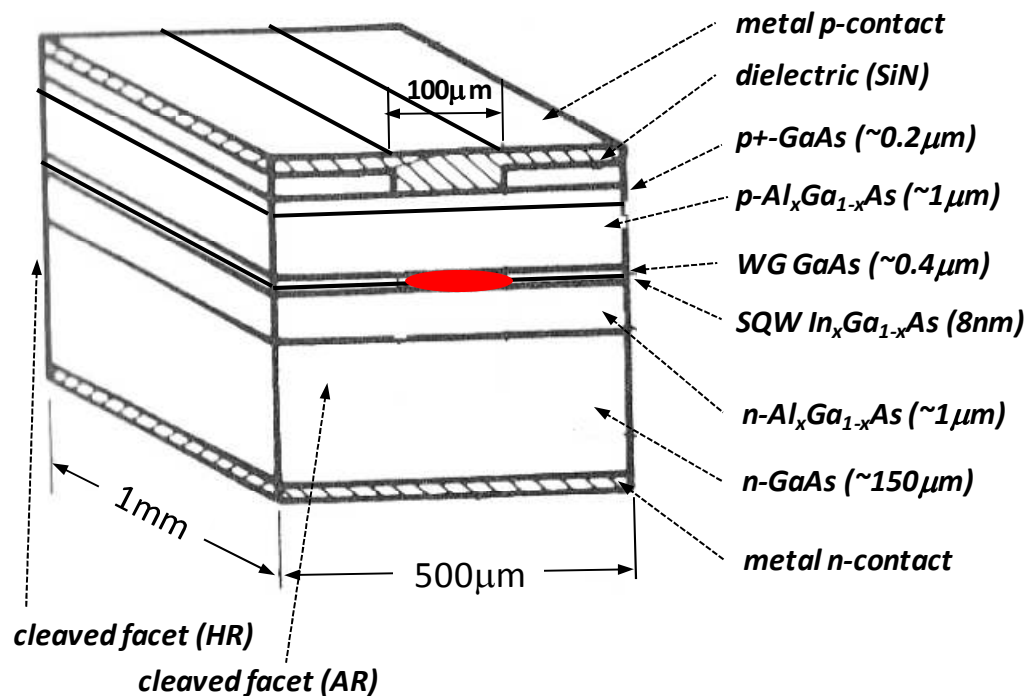
Figure 1.4 Schematic of an in-plane Semiconductor Diode Stripe Laser

1.2 Laser Diode Types

Conventional in-plane laser fabricated from the structure mentioned in previous section consists of a QW and a waveguide establishing transverse optical confinement. Optical resonator is created by two mirrors located on both sides of the semiconductor diode, illustration of which is in Figure 1.5. Waveguide between the mirror reflectors provides light confinement and travel. Typically the mirrors are built by high reflection

(HR) and anti-reflection (AR) coating the facets after cleaving the structure along crystal axis, and since $r_1>r_2$, so that the mirror #2 has high output though the facet. The advantage of such in-plane structures is high amplification factor resulted from long length, but output occurs from facet. These devices are commonly known as edge-emitters.
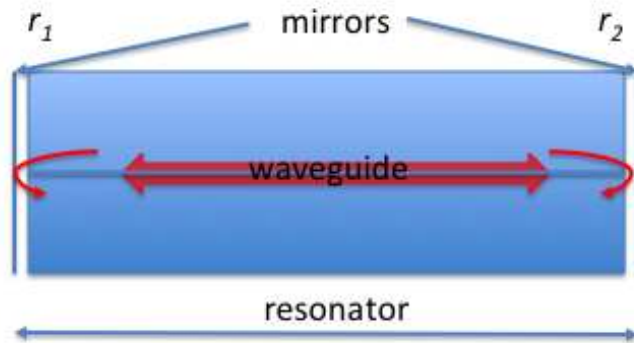
Figure 1.5. Schematic of optical resonator

Waveguide within the resonator is typically based on $Al_xGa_{1-x}As$ compound. In the case of lasers described in this work, the optical confinement for the waveguide is provided by variation of Al mole fraction in the $Al_xGa_{1-x}As$ creating a graded refractive index profile (GRIN) in transverse direction. Since a QW was used as active layer providing separate carrier's trapping, a common name for such design in laser diodes is Graded Refractive Index Separate Confinement Heterostructure (GRINSCH).

As mentioned earlier, most simple lasers cavities are defined by the cleaved edges of the crystal, called facets. Edges form reflectivity profiles and through use of additional fabrication techniques, it is possible to increase or decrease the feed-back reflectivity. That is done by several methods like coatings of high or low reflection coatings, typically made of dielectric layers. The two parallel edges form a Fabry-Perot (FP) resonator.

Cleaved facets provide no spectral selectivity and therefore conserving the broad emission spectrum of the laser. Spectrally selective feedback reflectors are introduced to reduce spectral bandwidth. Figure 1.6 illustrates three most common basic semiconductor resonators: FP type, Distributed Bragg Reflector (DBR), and Distributed Feedback (DFB). Although these ideas were proposed in early 1970's (Alferov et al. 1971) it took several years for technology to catch up to create high quality DBR and DFB devices.
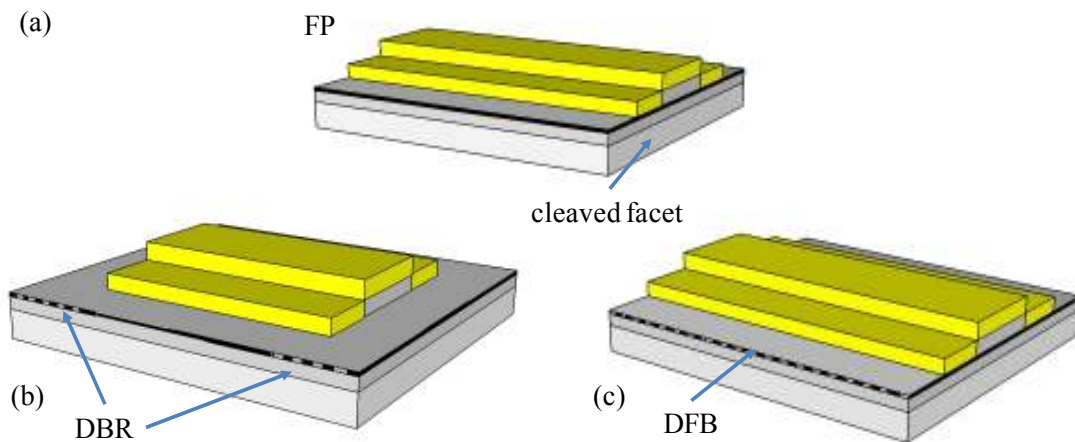
Figure 1.6 Schematic of three types of edge emitting lasers (a) Fabry Perrot (b) first order Distributed Bragg Reflector and (c) Distributed Feedback

Design of surface emitting lasers is based on semiconductor heterostructures similar to those used for edge emitting lasers, however typically employ an optical component allowed to emit light from a surface parallel of angled to p-n junction plane. Advantage of surface emitters is the use of large area for output, eliminating narrow, less than wavelength, emitting size of the FP emitter in the transverse direction (fast axis). Due to the increase in surface emitting area, the divergence angle reduced. Examples of such devices are: Vertical Cavity Surface Emitting Lasers (VCSEL), Turning Mirror

Lasers, and Grating-Coupled Surface Emitting Lasers (GCSEL). Although these configurations are significantly harder to fabricate and implement, each can be a numerous advantages over standard FP device in such terms as "high brightness", "high efficiency", "high power", etc.

VCSEL technology is a relatively new type of light emitters. Introduced in late 1970's, it is not until 2001 (Miller et al. 2001) that VCSEL's could be considered as a high power optical source. The idea behind the technology is to build a resonator allowing light propagation in the direction perpendicular to p-n junction. High efficiency Bragg mirrors of high and low reflection profiles on "bottom" and "top" of the device respectively are then employed. Refer to Figure 1.7 for illustration. Bragg mirrors are needed of high efficiency since the light amplification is then obtained through a relatively narrow quantum well section. Because of the low amplification factor for a narrow SQW, a MQW is used to create a high-Q resonator resulted in lower laser threshold.
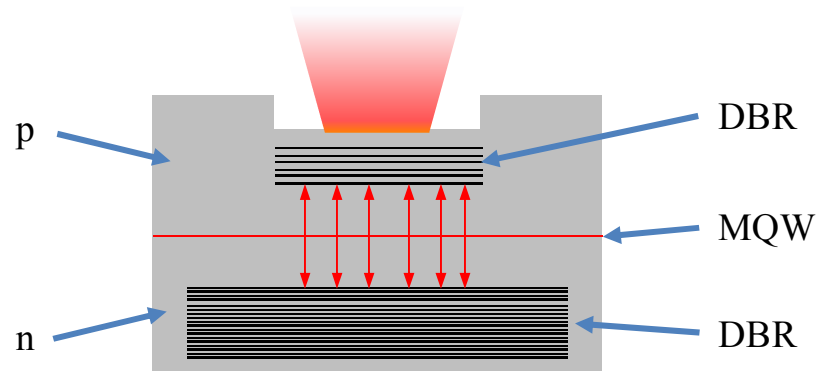
Figure 1.7 VCSEL Illustration

Turning Mirror outcoupling scheme is to use a surface etched at the angle to the waveguide for beam output. Typically this is a 45^0 mirror (Evans et al. 1993). Example of structure is depicted in figure 1.8. Such devices are rare, since hard and nonstandard fabrication techniques must be implemented. These are specific wet chemical etching and advanced analog lithography with selective reactive ion etching combination.

Figure 1.8 Turning Mirror Illustration

1.3 Basic operation characteristics of laser diodes

Laser diode characteristics can be summarized in several categories: electrical, spatial, spectral, optical, dynamic and reliability. Optical properties of the devices vary by application and are valued measurements in interferometry applications, dynamic is for complex circuit modeling and its aspects and reliability is a lifetime of the devices usually measured by burn-in tests. In the scope of the work due to research aspects the most critical parameters are electrical, spatial and spectral.

Electrical and optical properties of a laser diode involve the light-current-voltage characteristics under given current driving conditions (L-I-V). Electrical-optical transition of laser diode characterization is the light-current (L-I) curve. The plot represents output light power to the device versus applied driving current. Figure 1.9 represents a sample light current plot for a general laser diode device in operation. From

the L-I curve, the following characteristics are extracted: threshold current (I_{tr}), slope efficiency ($\frac{dP}{dI}$ in Watts/Amp), and appropriate operating point at a set current. Threshold current and slope efficiency of typical laser is also a function of Temperature, typically operating conditions of the device are at room temperature (20°C).
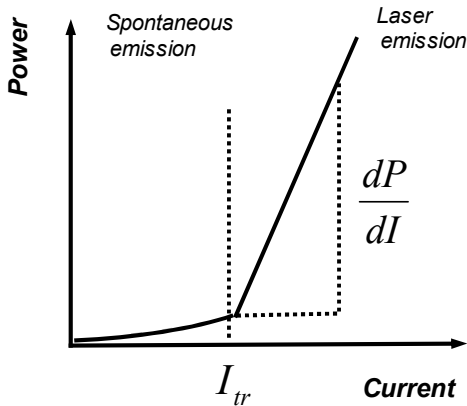
Figure 1.9. L-I Characteristics of the edge-emitting laser diode

Another important electrical property is the current-voltage (I-V) curve, illustrated as an example in Figure 1.10. This curve is typically acquired during the L-I characterization and symbolizes laser electrical property in terms of resistance, R_s and shows the nominal voltage drop across the diode. For 975nm emitters, typical nominal drop corresponds to the bandgap of the active layer (QW) and is of 1.1 Volts and operating value range is around 1.5V. From the L-I-V plots, another important parameter can be determined, wall plug efficiency (WPE) defined as the power ratio of the optical power out vs. electrical power in, defined in equation 1.2

$$WPE = \frac{P}{IV} \qquad\qquad 1.1$$

Practical examples with FP type devices and basic L-I-V characteristics acquisition will be presented in the device testing and characterization chapter 5, specifically section 5.2
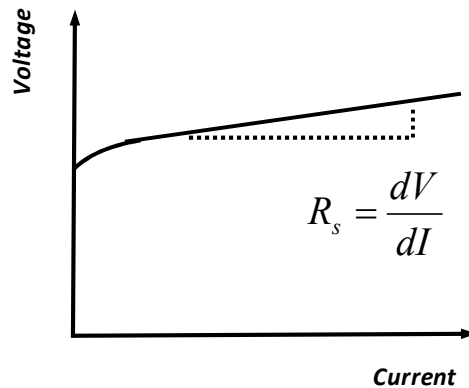
Figure 1.10 V-I Characteristics of the edge-emitting laser diode

Spectral characteristics are a very important parameter of the laser diode. There are two types of laser diode devices: single-mode and multi-mode. Broad area multimode lasers may consist of a number of longitudinal as well as lateral modes. Spectrally, for narrow area type laser diodes these are longitudinal modes. Lasing wavelength,λ_0 of the device occurs when the modal gain is equal or higher than the threshold gain that is necessary to overcome the intrinsic absorption and the losses in the two mirrors of the resonator. Only the modes that are closest to the gain peak are amplified while other longitudinal modes are suppressed by losses. The center wavelength may also shift due to thermal effects and drive currents. Typically, with increase of temperature, the center wavelength red shifts. For the AlGaAs-GaAs compound structures with InGaAs QW operating at 980 nm, shift to longer wavelength is in the order of $\Delta\lambda/\Delta T = 0.3$nm/°C. For single-mode devices, this effect may occur in terms of "mode hopping" when the center

wavelength shifts are not gradual. Figure 1.11 shows the spectrum of a sample FP type device with a center wavelength, spectral width and longitudinal mode spacing at operating current past the threshold. The device stripe dimensions are 1 mm long and 100 μm wide. In this example, center wavelength is λ_0 = 974.8 nm with spectral width of full width half maximum of $\Delta\lambda_{FWHM}$ = 0.8 nm. The longitudinal mode spacing for given mode number can be estimated in terms of cavity length, L and the waveguide group refractive index, n_{gr} defined by the following formula:

$$\delta\lambda_0 = \frac{\lambda_0^2}{2L \cdot n_{gr}}$$ 1.2
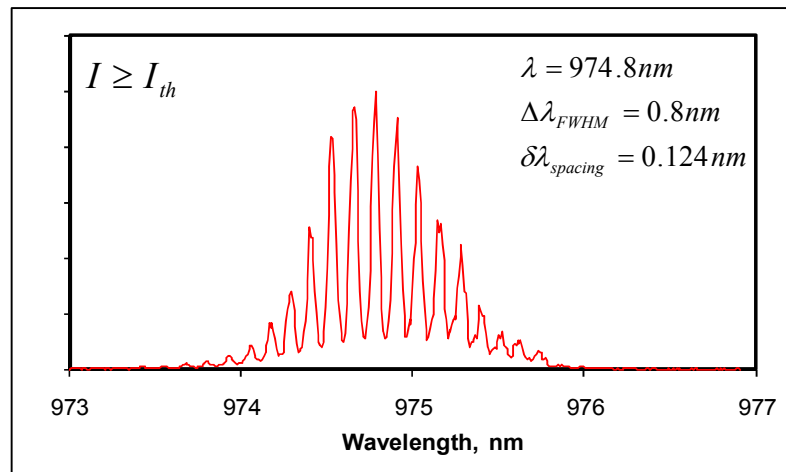
Figure 1.11. Sample spectrum measurements of a 1mm long, 100mm wide device operating at current higher than threshold with center wavelength of 974.8 nm

In terms of spatial emitting characteristics of laser diodes, the far field (FF) profiles have an asymmetric beam shape. This is due to the geometrical shape of the near field (NF) where the size of emitting area in transverse direction is smaller than the wavelength resulting in the light divergence at higher angle than that of lateral direction divergence. The "fast axis" corresponded to transverse direction is located along θ and

"slow axis" corresponded to lateral direction is along ϕ directions. Figure 1.12 depicts a schematic of the laser diode with emission output representation. It is then advantageous to use grating outcouplers since the NF output profile can be shaped in the lateral and the longitudinal direction avoiding high divergence angle numbers. However, although there is improvement in the divergence distribution, this does not imply beam quality since the mode distribution within the cavity is defined by the design of active structure.
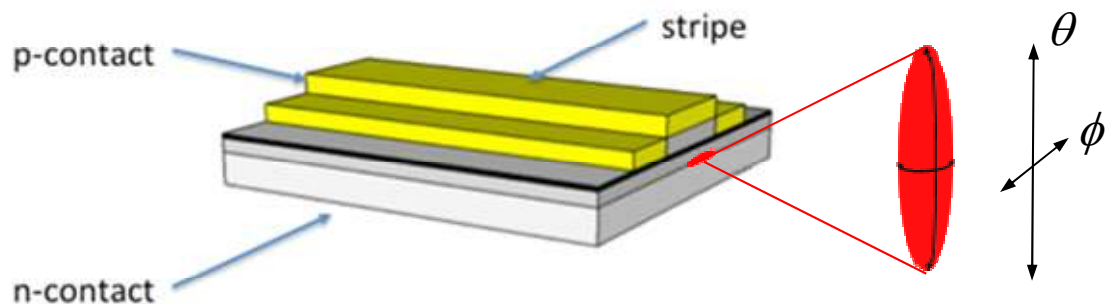
Figure 1.12 Schematic illustration of the beam profile from a broad area Fabry Perot diode laser

1.4 Grating coupler

In-plane structures still remain of high interest as due to the longer cavity length and therefore high total amplification factor resulting in higher power output, the achievable output power from single emitter is greater than that of VCSEL technology. VCSELs are also limited in terms of output region dimensions; with large emitting area beam quality suffers sufficiently. Several types of devices incorporating in-plane structure and creative surface output were also studied over the years.

Surface outcoupling can be performed using grating couplers. Gratings fabricated can also be used for feedback, depending on the necessity. These are second order DBR, DFB, blazed gratings, or grating couplers detuned from Bragg condition. Grating period Λ of second order DBR of DFB is a function of the desired wavelength λ and waveguide effective refractive index n_{eff}:

$$\Lambda = \frac{\lambda}{n_{eff}} \qquad\qquad 1.2$$

For second order Bragg grating couplers, 1st order reflection acts as a feed-back element while 2nd order serves as output perpendicular to p-n junction plane. For a proper grating design, the power ratio of the reflected light between the first order and output light in the second order are considered. Figure 1.13 shows a surface emitter using the DBR grating for light outcoupling, labeling 1st and 2nd reflected orders. Sufficient work was been performed with DBR gratings, implementing second, and even nth order Bragg conditions for wavelength stabilization and outcoupling. Blazed grating fabrication (Hagberg et al. 1995), high reflection coatings (Evans et al. 1993) are among numerous techniques for efficient output in one direction only. Section 1.5 discusses grating coupled surface emitters (GCSEs) with a grating detuned from Bragg condition, outcoupling light at an angle.
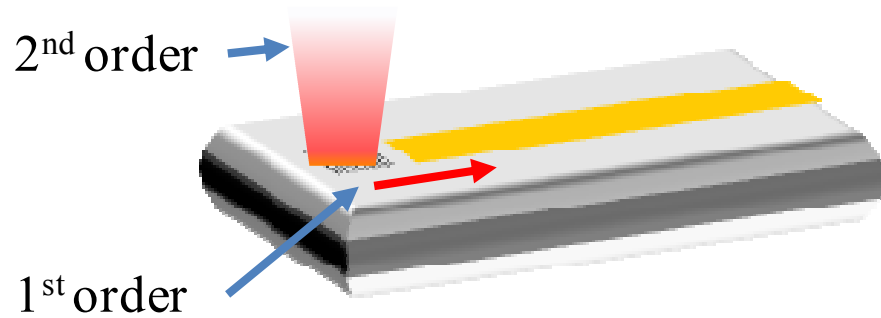
Figure 1.13 Surface Emitter with 2nd-order DBR

Alternative to DBR structures are surface-emitting devices achieved by fabricating grating outcouplers, with a grating period detuned from the Bragg condition. Grating period can be selected between the 1st and second Bragg orders for outcoupling light at an angle. Another condition to be considered is to eliminate all but one order diffractions in the substrate. This provides low residual reflectivity, example of which will be discussed in section 5.3.2. The low grating residual reflectivity provides ability to operate as an SOA and in s-LED mode, where the spontaneous emission bandwidth is still in the order of 20nm. This is advantageous to build different type of emitters by use of feedback advantage of detuned grating couplers are over 2nd order gratings. Examples of such are presented in section 1.5. The period, d_{gc}, of the grating conditions are then summarized in equation 1.3

$$\frac{\lambda}{2n_{eff}} < d_{gc} < \frac{2\lambda}{n_s + n_{eff}} \qquad\qquad 1.3$$

Where, n_{eff} is the effective refractive index of the grating region; n_s is the refractive index of the substrate; and λ is the operating wavelength. Figure 1.14 depicts a schematic of a broad area single sided grating coupled surface emitting laser (GCSEL).
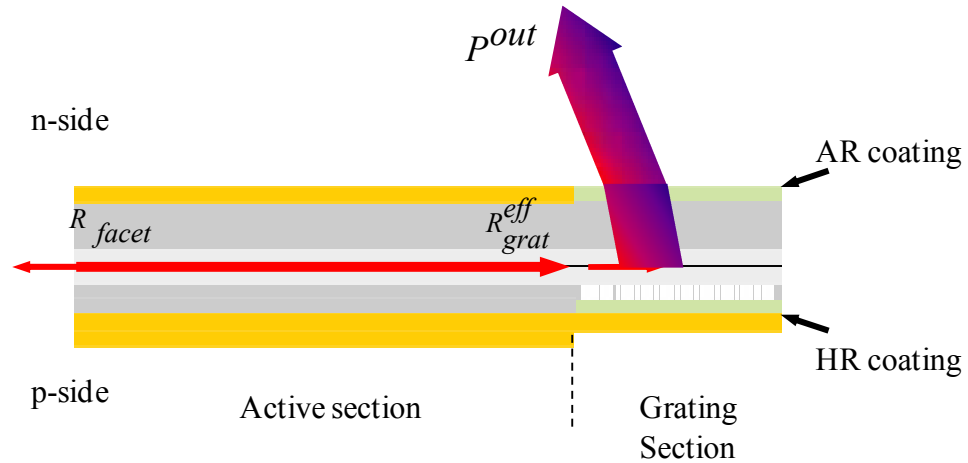
Figure 1.14 Schematic of a single sided grating coupled surface emitting laser (GCSEL)

1.5 Types of Grating Coupled Surface Emitters

Based on the detuned grating technology different types of grating coupled surface emitters (GCSE) were designed and experimentally evaluated by Microphotonics Laboratory group. Employing a broad-area semiconductor laser diode with two monolithically integrated optical elements was presented (Vaissié et al. 2003). A detuned 275-nm period second-order diffraction grating on the p- side was combined with a refractive lens fabricated on the n-side. The device produced a circular focused output spot demonstrating ability of dual optics integration with a broad area semiconductor diode.

A high efficiency tapered grating surface-emitting laser with an antireflection-structured (ARS) n-side substrate (Vaissié et al. 2005). Figure 1.14 shows the device sketch incorporating a grating coupler. Optical feed-back in these lasers was formed by reflection from cleaved facet and by low residual effective reflection from grating side. A high reflection (HR) coating on p-side provided output in single direction for

performance enhancement. Device has exhibited a 64% improvement in efficiency with monolithically integrated sawtooth-shaped ARS on the GaAs substrate.
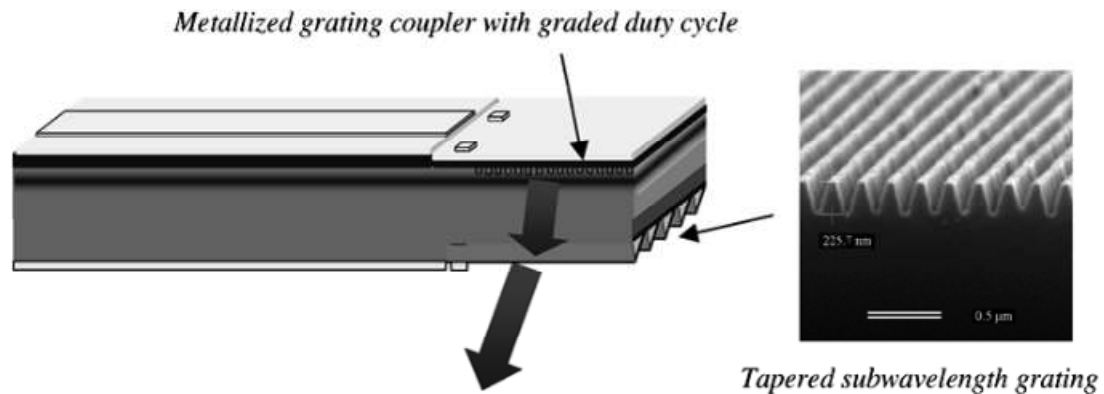
Figure 1.15 GCSEL device sketch and SEM micrograph of the tapered antireflection SWG integrated on the GaAs substrate. Light is coupled out by a 270-nm period grating coupler with varying duty cycle to improve the near-field intensity profile. The tapered profile of the subwavelength structure is obtained by a mask erosion technique.

Further dual optics integration was performed by a novel wavelength-stabilization scheme for broad stripe surface-emitting lasers (O'Daniel et al. 2006). The method was based on two gratings fabricated on p- and n- sides of a device in which the first grating disperses light into the substrate at the angle greater than total internal reflection (TIR), where the second surface has a grating that operates in the Littrow condition to provide optical feedback into the gain medium. With this dual grating reflector (DGR), a single lasing line was achieved with spectral band width of 0.2 nm. Figure 1.15 (a) shows the schematic device incorporating grating couplers and a feedback grating, while figure 1.15 (b) shows the fabricated device in operation. The grating outcoupler fabricated on the other side of the DGR, provided efficient surface emitting output through the GaAs substrate. The paper has also demonstrated high slope along with a narrow spectral line.
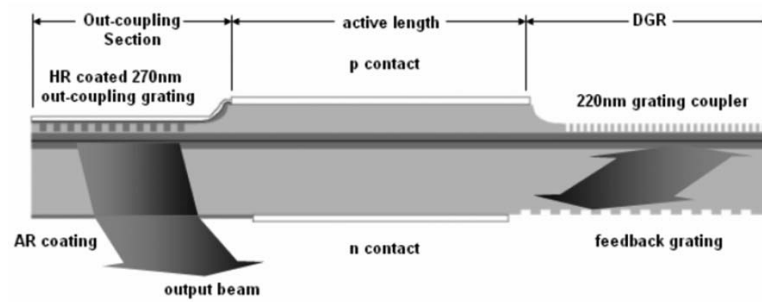
(a)
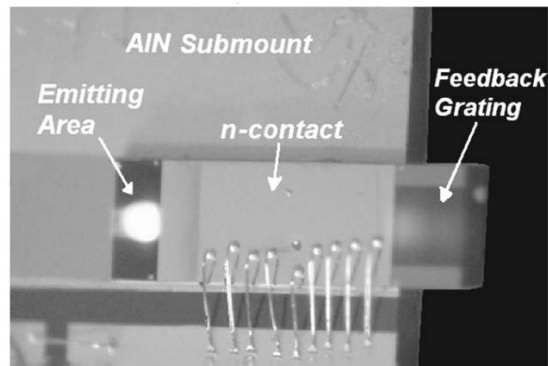
(b)

Figure 1.16 (a) Schematic of fabricated device incorporating a DGR and a 270 nm outcoupling grating with a HR coating providing output. (b) Image of the fabricated device in operation mounted p-side down upon a submount.

Along with a monolithically integrated feedback element, an external dual grating reflector coupled surface emitting laser array was demonstrated. The emitters were also wavelength locked by means of an external diffraction grating array in Littrow arrangement fabricated on a silicon die (Yilmaz et al. 2010). Figure 1.16 depicts the device schematic.
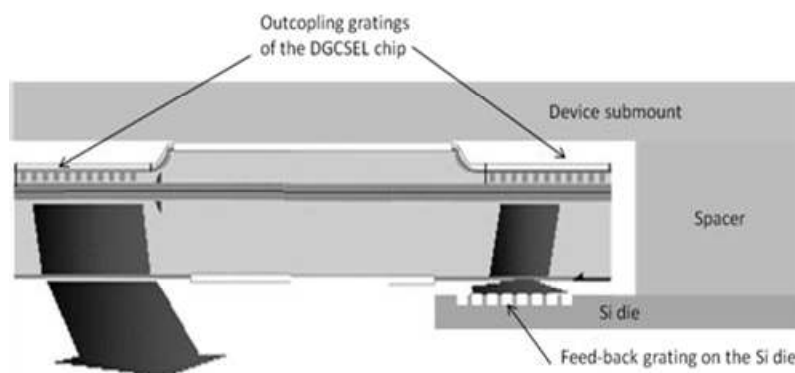
Figure 1.17. GCSEL device with external wavelength selective element

Two-dimensional array based on vertically stacked grating coupled surface-emitting laser bars (Yilmaz et al. 2011). The emitters in the array were individually wavelength stabilized using external Littrow gratings fabricated on silicon-based spacers. Figure 1.17 demonstrates a 2D stacked array assembled and in operation.
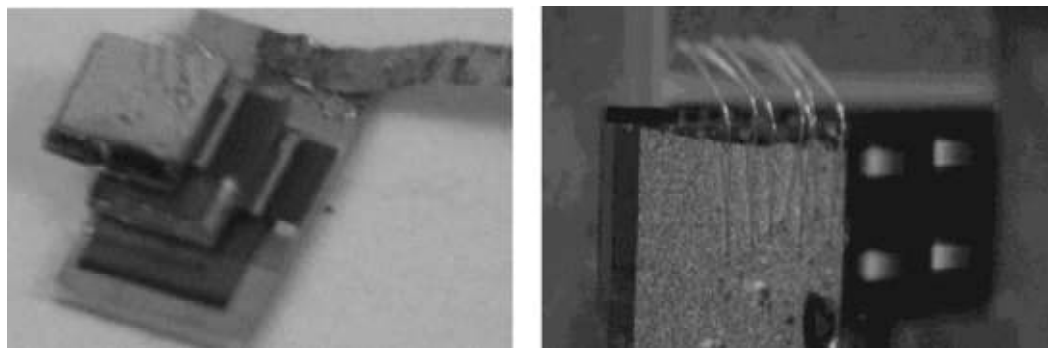
Figure 1.18 (left) Assembled 2-D array device; (right) 2-D array device in operation

Grating couplers were also researched for a master oscillator power amplifier (MOPA) configuration (Smolski et al. 2006). Figure 1.18 demonstrates vertically stacked laser diodes with optical coupling provided by identical in-plane integrated gratings. Low beam divergence, large emitting and input areas of the grating coupled devices simplify

the assembling technique over the fabrication of MOPA devices based on edge-emitting laser diodes. The master oscillator also incorporates a dual-grating reflector providing a wavelength-selective feedback resulting in a narrow emission spectrum at a wavelength of 975nm. The power amplifier was a tapered chip with two integrated gratings which were used for in- and out-coupling of the light.
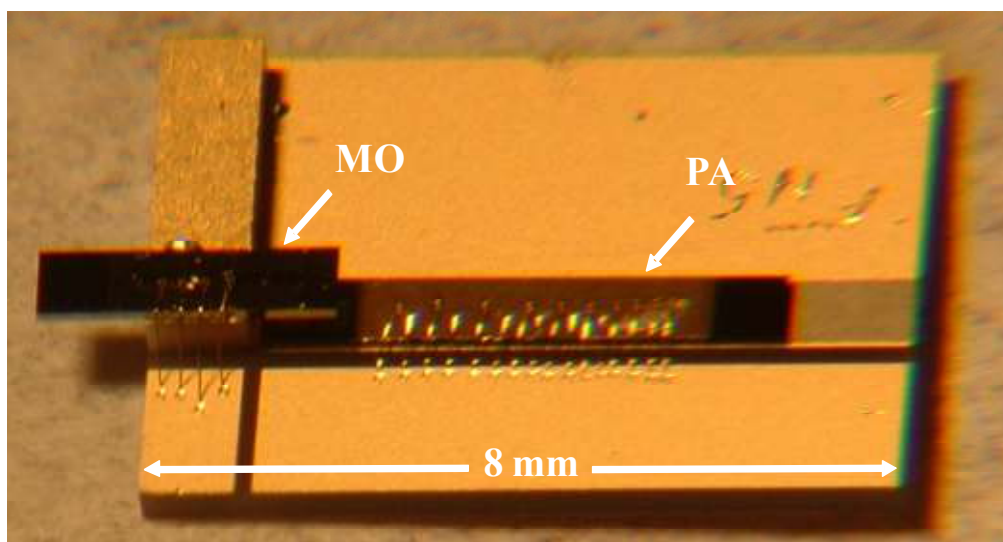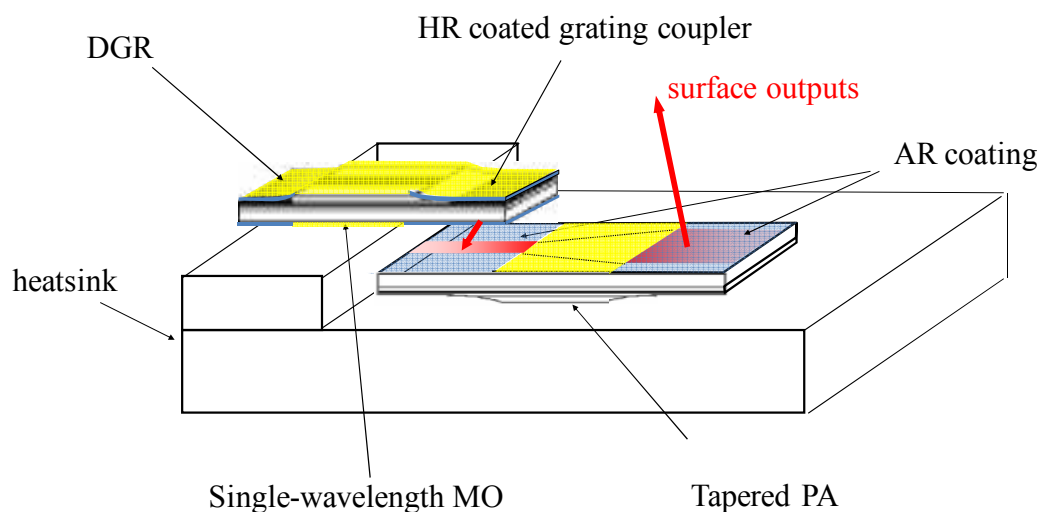
Figure 1.19 Schematic (top) and actual devices image (bottom) of MOPA assembly operating at a wavelength defined by the DGR section

1.6 Summary and Work Outline

A lot of great research was done in developing technology of the outcoupling gratings and applications. Numerous conceptual designs of the emitters with monolithically integrated grating couplers were studied and some were demonstrated in section 1.5. The study involves more details regarding variation of the grating coupler parameters to obtain the desired 1D and 2D intensity profile of the optical beam emitted by a grating coupled surface emitting lasers. Improved near field distribution of the optical beam from the grating was suggested. An outcoupling grating was also used to spread a single optical output into multiple beams at different outcoupling angles in the emitting plane. This was done by variation of the periodicity, duty cycle, and the groove tilt angle of the grating. Grating design involves numerical analysis of the optical field propagated through the grating, by applying the Rigorous Coupled Wave Approach method. Experimental evaluation of the designed grating components was done by fabrication and testing the broad area semiconductor lasers with the monolithically integrated grating outcouplers. Chapter 2 presents the study and experimental evaluation of the designed devices. Section 2.3 depicts the design of the grating using varying fabrication parameters to form a Gaussian shape near field (NF) output profile. Section 2.4 presents the study of the 2D splitting grating implemented with single broad area stripe device. The obtained results show the close match of the designed output parameters, given angle separation between individual output beams. To further explore grating outcoupler as a spatial controlling parameter of the output beam, the design is made for uniform field profile across the grating in section 2.5

Due to limiting parameters and absorption losses, grating couplers may be used in conjunction with power amplifier sections. Arrays of phase locked surface-emitters including semiconductor optical amplifiers spaced by grating outcouplers were designed and fabricated in 1D and 2D configurations. Mutual coherence of the multi-emitters was experimentally evaluated by interference investigation and the obtained results were compared to numerical modeling. Study of the 1D and 2D arrays is presented in sections 2.6-2.8.

CHAPTER 2: RESEARCH

2.1 Introduction

As discussed in chapter 1, surface emitting diode lasers have packaging advantages over conventional edge emitters where the vertical emission enables the easy integration of the output beam with fibers and/or other optical elements.

One approach of surface-emitter designs is a grating coupled surface emitting laser (GCSEL) based on in-plane structure with a monolithically integrated grating outcoupler (Vaissié et al. 2005). The grating, which periodicity is detuned from the Bragg resonance, exhibits low feedback reflectivity that makes GCSEL attractive for various applications. The advantage of outcoupling the light by a grating, include the ability to shape the Near-Field (NF) intensity distribution, thus allowing for control of the output beam characteristics through small variations of the processed grating parameters, such as periodicity, duty cycle, tooth height, and groove tilt angle. Numerous approaches were investigated theoretically (Miyanaga et al. 1981 and Touam et al. 1997) and experimentally (Bates et al. 1993) to control the outcoupled beam distribution.

In practice, the variation of the duty cycle parameter is the most preferable method to shape optical intensity within the outcoupler. This method is easily implemented by the use of e-beam lithography, capable of making the desired grating layout on resist, which is based upon the file created with standard binary mask design tool. Fabrication of advanced grating outcouplers does not introduce more complexity in

relation to processing the uniform grating due to the same etching process. In our previous work, we used this practice to modify the GCSEL longitudinal NF from an exponential decay to a more symmetric bell-shaped profile (Vaissié et al. 2005). In another study, we applied a similar approach to change the duty cycle in the lateral direction for the Littrow grating used in combination with a grating outcoupler for wavelength locking (Smolski et al. 2010). With the functionality of this technique, the optical feed-back element was enhanced by providing laterally variable reflectivity allowing us to improve the beam divergence from the broad area lasers. In this paper we present further investigation of this method aimed for precise control of the NF intensity profile. This effort was motivated by our findings that etch depth, and grating tooth height, strongly depend on the resist opening width. This effect significantly amplifies the impact of duty cycle variation on the grating outcoupling strength, also on the grating radiation factor, defined as the outcoupled optical power per unit length of the grating. Along with the obtained experimental data we also present a numerical simulation analysis used for the design of the grating outcouplers.

Variation of the grating parameters is also attractive in forming of the Far-Field (FF) of the outcoupled beam. As examples, curvature-shaped (Kristj´ansson et al. 2000) or circular (Kristj´ansson et al. 1997) gratings were used for the outcouplers designed to focus the output beam above the grating surface. More advanced beam shaping was demonstrated by using a dislocated grating design (Li et al. 1996), which implements spatial variation of the phase shift to the outcoupled light. However, these outcouplers, based on spot-array generation, tend to produce optical feedback even while the grating periodicity is detuned from Bragg condition (Modh et al. 2002). In this case, the device

design should involve engineering the optical feedback (Modh et al. 2002) which potentially reduces the applications of this approach. To provide multiple beams outcoupled at different angles from one grating, we used a spatially sectioned grating, but in our approach each pixel is designed for specific output angle by varying grating periodicity and groove tilt angle. In this paper we introduce the multi-sectioned grating design along with experimental evaluation of the concept.

2.2 GCSEL Design and fabrication

For experimental evaluation of the grating design, a number of GCSEL devices incorporating a broad area active section and grating outcouplers were fabricated and tested. The emitters were processed from an AlGaAs graded index separate confinement heterostructure (GRINSCH) with a strained 976-nm InGaAs single quantum well, grown by metal organic chemical vapor deposition. The waveguide region was undoped $Al_xGa_{1-x}As$ with Al composition, graded from x=0.05 to x=0.40. To reduce transverse optical loss, we used $Al_{0.4}Ga_{0.6}As$ cladding layers with graded p and n doping respectively. The epi-structure also included a lattice matched InGaP etch stop layer. The etch stop was used for precise localization of the grating processed in the p-cladding and it's position, 250nm above the waveguide, was verified with detailed analysis of the optical field propagated through the grating.

The grating performance was analyzed using numerical modeling with the Rigorous Coupled Wave Approach (RCWA). RCWA has an advantage due to the fast computation time and high accuracy, and it is specifically designed for analysis of the diffractive optics structures. The simulation tool allowed extraction of the outcoupling length in terms of the grating layout with respect to optical field confined in the GRIN

waveguide. The optical field is propagated through the structure and the outcoupling length is the unit length, at which the power of the propagated mode is decayed by 1/e. For the grown epi structure and the specified position of the etch stop, the refractive index profile was first calculated. RCWA model was then run with varying the features for feasible duty cycle and etch depth. A two dimensional plot in Figure 2.3 (a) illustrates the sensitivity of the outcoupling length versus duty cycle and etch depth. Simulation results combined with fabrication tolerances and semiconductor properties served as the base to the design of the feature.

Prior to grating fabrication, the p-side of the blanked epi wafer was processed for bars of the 100μm- and 200μm-wide p-contact stripes. Mesa formation was done by deep wet-etching the Al$_x$Ga$_{1-x}$As p+- and p-clad layer down to the InGaP etch-stop. Ti-Pt-Au contacts on the top of the mesas were patterned by lift-off of the metal deposited by e-beam evaporation technique. The grating outcouplers were fabricated close to p-contact edges by applying e-beam lithography. For this purpose we used JEOL JBX-9300FS E-Beam tool which instrumentation file was made following grating design specifics, including spatial distribution of the grating's parameters such as periodicity, duty cycle, and groove tilt angle. After exposure and developing of the resist, the gratings were etched on the top of GRIN waveguide applying the BCl$_3$/Ar based RIE. We used a 130nm-thick SiN dielectric deposited by one PECVD process as an insulator layer outside the mesas, also serving as a buffer layer on the top of processed gratings. After RIE etching the SiN openings for p-contacts, a Cr/Au metallization completed the p-side processing. The top metal layer was also used as a high reflection coating for the grating that enhanced light outcoupling in one direction through the GaAs substrate. The p-

processed samples were thinned to a thickness of ~150µm and n-side surface was polished to the mirror finish quality. The Ni-Ge-Au n-contact patterns were aligned to the p-contact using a Quintel front-to-back mask aligner. To reduce reflectivity at the GaAs/air interface, a λ/4-thick SiN layer was deposited by PECVD and then patterned for output ports at the substrate surface.

For experimental evaluation of the grating outcoupler performance, GCSELs devices with uniform grating outcouplers were cleaved, bonded p-side down on the AlN-based submount and tested. The test GCSELs consisted of a 2mm-long active section with the 100µm-wide stripe and a 260nm-periodicity grating outcoupler. An optical feedback for the laser diode was provided by reflections from the cleaved facet on one side of active section and from an integrated grating on the other side. Similar to those described in [1], the grating duty cycle for test samples was tailored from ~80% to 50% in the longitudinal direction on the initial 80 µm of the grating coupler closest to the active section. Fig 2.1 (a) presents the NF profile measured at the driving current above the lasing threshold. The estimated value of exponential decay was ~110 µm, which was close to predicted outcoupling length by simulating the 260nm period grating with 50% of duty cycle and 260nm of etch depth. The processed GCSEL exhibited a grating output slope of 0.73W/A with pulse driving conditions. Based on the performance analysis of the broad area edge-emitters fabricated from the same processing lot, the internal quantum efficiency and the internal optical loss were estimated of 85% and 1.5cm^{-1} accordingly. The free-carrier absorption for the lasing light propagated through the GaAs substrate was evaluated of 8.5cm^{-1} in separate experiments resulting in a total optical loss

of 12% for a 150μm-thick wafer. Given the above parameters, the maximum achievable

optical power slope output from the grating was estimated of 0.81W/A, which resulted in

a 91% of grating outcoupling efficiency achieved from the processed GCSELs.
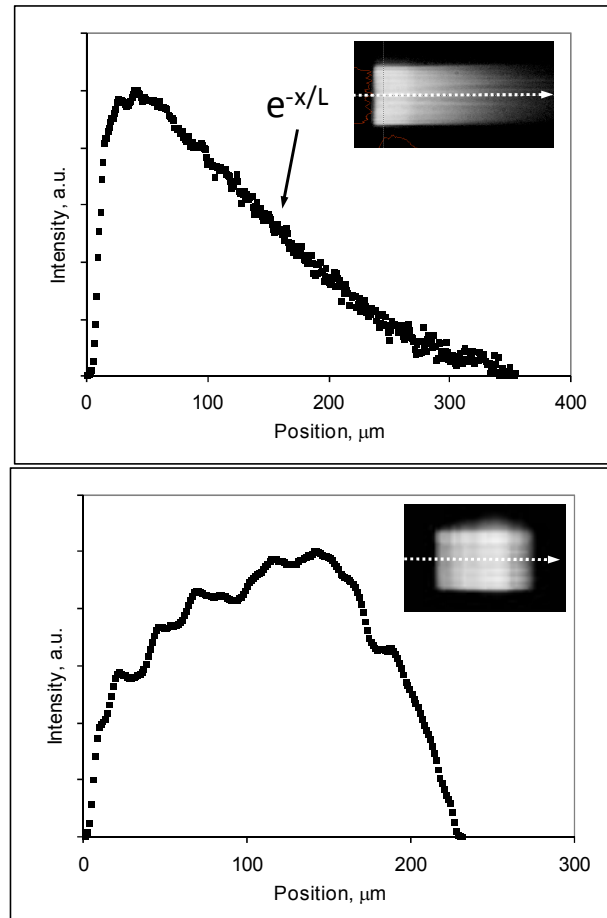
Figure 2.1: Near-Field profile along the grating in the longitudinal
direction for the GCSEL devices with different designs of the grating
outcoupler (inserted are images of the outcoupling area): a) uniform
grating with the 80 μm-long tailored duty cycle from 80% to 50%; b).
grating with smooth variation of the duty cycle

2.3 Variable duty cycle Grating design

For detailed investigation into the impact of the resist opening width to the etch

depth, we simply used a grating with smooth variation of duty cycle from 90% to 60% in

the longitudinal direction for a length of 200 μm. The Near-Field profile recorded from a GCSEL with such a grating outcoupler is presented in Fig1. (b). The NF intensity distribution had a rippled shape that took place due to patterning of the grating. This effect could be explained by the grating layout in the CAD file, which was divided on several grating subsections stitched together. The similar processed grating was cleaved in a direction perpendicular to the grooves for further investigation of the etched profile with a scanning electron microscope (SEM). The obtained results are shown in Fig.2 demonstrating significant reduction of the etch depth with decreasing the resist opening. Such an effect resulted from a specific recipe process of a shallow GaAs RIE etching given the grating parameters of 270nm-periodicity and 50% - duty cycle. It was expected that the etch rate would significantly decrease with the increase of the material duty cycle, and thus the resist opening reduction. Following our simulation, the outcoupling length was changed from 650 μm to 130 μm for the grating parameters variation shown in Figure 2.2. Therefore the achieved grating radiation factor had almost three times of a stronger effect compared to those estimated in the conditions of a constant etch depth with a varying duty cycle.
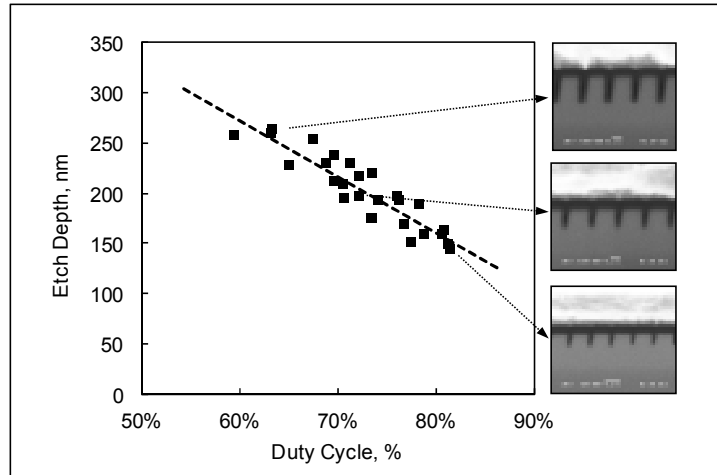
Figure 2.2: Etch depth vs. grating duty cycle obtained from SEM analysis of the processed grating with smooth variation of duty cycle (inserted are SEM images of the selected area of the grating).

Based on the obtained results, a grating outcoupler with a desired distribution of the radiation factor could be accurately designed. Figure 2.3 (b) presents an example of the grating duty cycle variation which predicted a symmetric bell-shaped NF profile. On the plot in Figure 2.3 (a), the dashed line points up the range of the grating parameters used for the design and their ratio were matched with the data from the previous experiment.
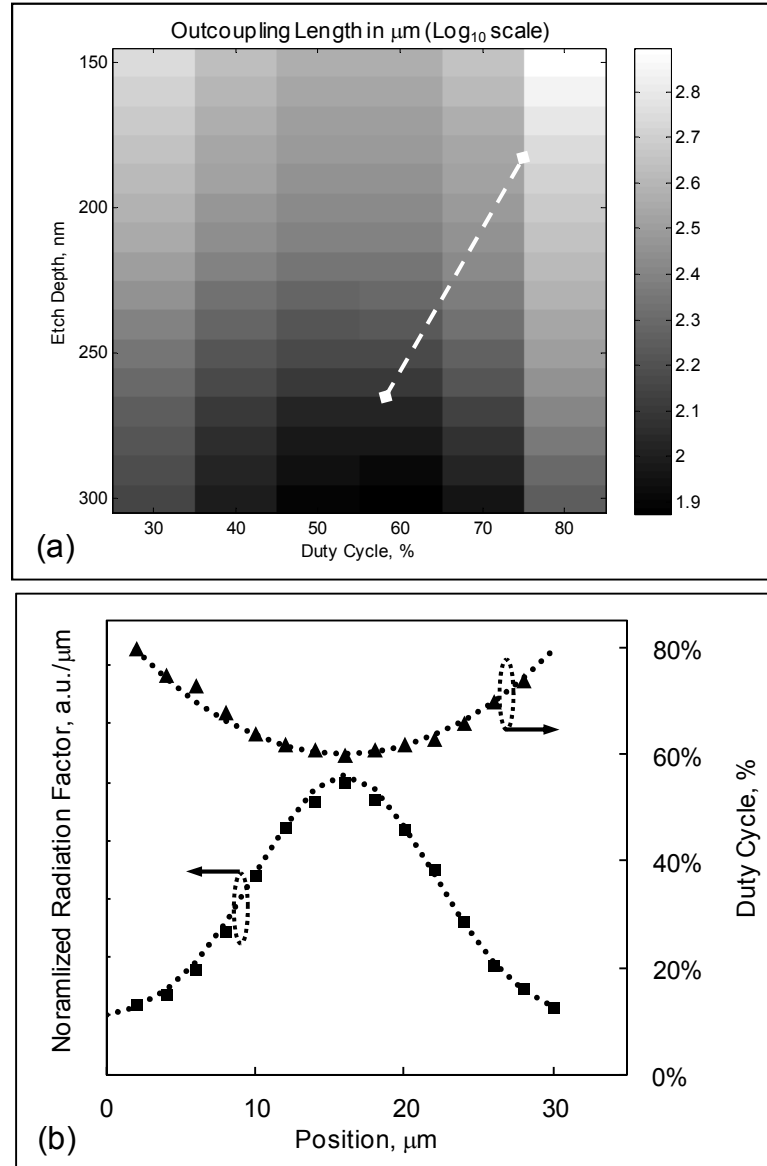
Figure 2.3: a) Grating outcoupler simulation data: Outcoupling Length parameter vs. etch depth and duty cycle (dashed line shows the grating parameters range used for design shown on plot (b)); b). Design of the grating for Gaussian NF profile with given etch process.

2.4 2D splitting Grating

Fig.4 shows a schematic diagram of the method to shape the beam outcoupled from in-plane laser diode by a monolithically integrated grating splitter. An optical planar-wave propagated through waveguide hits a multi-sectioned grating in which each

section had a grating periodicity and groove tilt angle designed for specific output angle. These grating parameters are linked together by the vector diagram in the junction plane as shown in Fig. 4(b):

$$\vec{k}_{xy} = \vec{k}_o - \vec{k}_{grat} \qquad\qquad 2.1$$

where $\vec{k}_o, \vec{k}_{grat}, \vec{k}_{xy}$ are the incident wave vector, the grating vector, and the outcoupled beam vector projected on the X-Y plane, respectively. Solving equation (1) for $\left|\vec{k}_{xy}\right|$, dependence can be shown on grating periodicity $\Lambda = \dfrac{2\pi}{\left|\vec{k}_{grat}\right|}$ and groove tilt angle φ. The outcoupling angle θ can be estimated from $\left|\vec{k}_{xy}\right| = \left|\vec{k}\right| \cdot \sin\theta$, where $\left|\vec{k}\right| = \dfrac{2\pi}{\lambda}$ is wave vector of the output beam in the air.
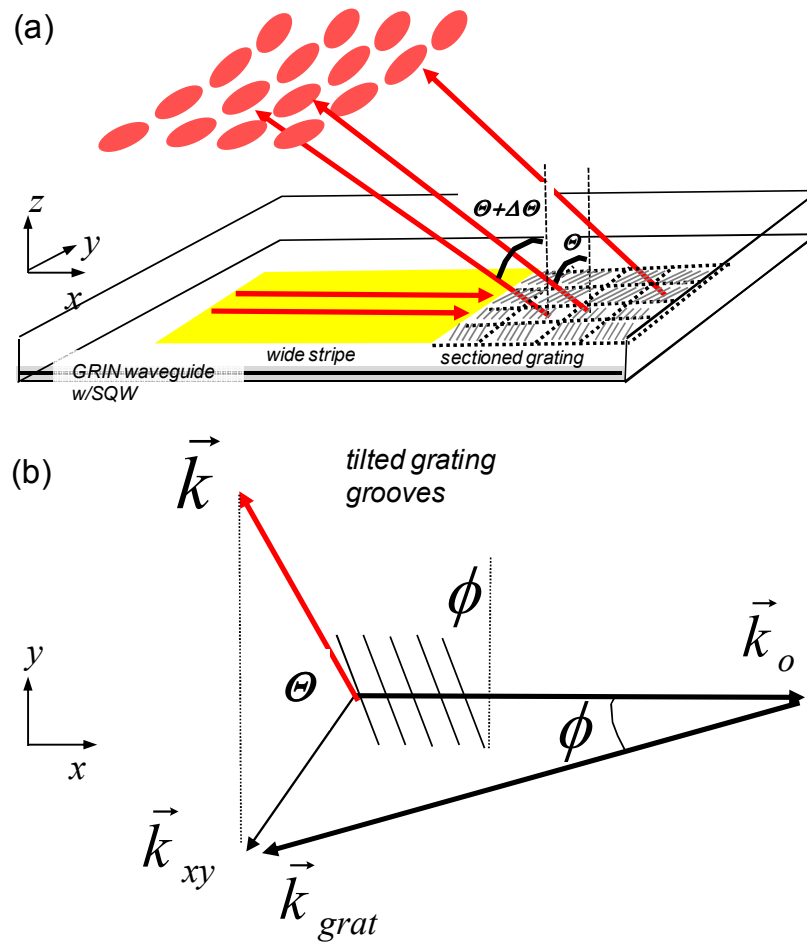
Figure 2.4: a) Schematic diagram of the multi-sectioned grating for splitting an output beam; b) vector diagram in the junction plane for the tilted grating.

For evaluation of the concept, a (8x8)-sectioned grating splitter was designed in such a way that outcoupling angles from neighboring sections differ by ~2 degrees in x and y direction. Single section dimensions were (25x25) μm^2 and so the total size of the grating outcoupler was (200x200) μm^2. The grating splitter was processed close to one side of 2mm-long active section with 200 μm-wide stripe, while on the other side; a 260 nm period grating coupler was fabricated. Since grating outcouplers exhibited low feed-back reflections, the active section was operated as semiconductor optical amplifier.

The fabricated device was tested by using an external laser source which provided a narrow lasing line at 976 nm with spectral bandwidth of 0.04 nm. The high quality laser beam output from a single mode fiber was collimated by a lens and it was coupled in the device waveguide through the uniform grating applying an external mirror. The injected light was amplified by the active section driven below the internal lasing threshold. The grating splitter emitting area and the outcoupled beams were investigated with an infrared camera. Fig.5 (a) shows the NF intensity profiles measured from the splitter in both longitudinal (bottom plot) and lateral (plot on left side) directions. The scanning lines are shown on the inserted image of the emitting area; the active stripe edge is close to the left side of the emitter. As with a standard grating coupler, NF intensity in the longitudinal direction falls off moving away from active section, which can be further compensated with the method described in section 2. The measured FF distribution of the beam shaped by the grating is shown in Fig.5 (b). On the inserted image, a multi-spot array outcoupled by individual sections of the grating splitter was observed. The plotted bars illustrate the intensity distribution measured in the directions as shown on the image. The bar heights were normalized to the intensity averaged by single spot. The bottom plot corresponds to the longitudinal direction and the averaged angular distance between the spots in that way was estimated to be~2 degrees, which matches with the original design. The angular distributions of the spots in lateral direction along with the corresponded intensity profiles were not symmetric, as shown on the left plot. Such splitting distortion was most probably due to imperfection of lateral alignment of the injected light from external laser.
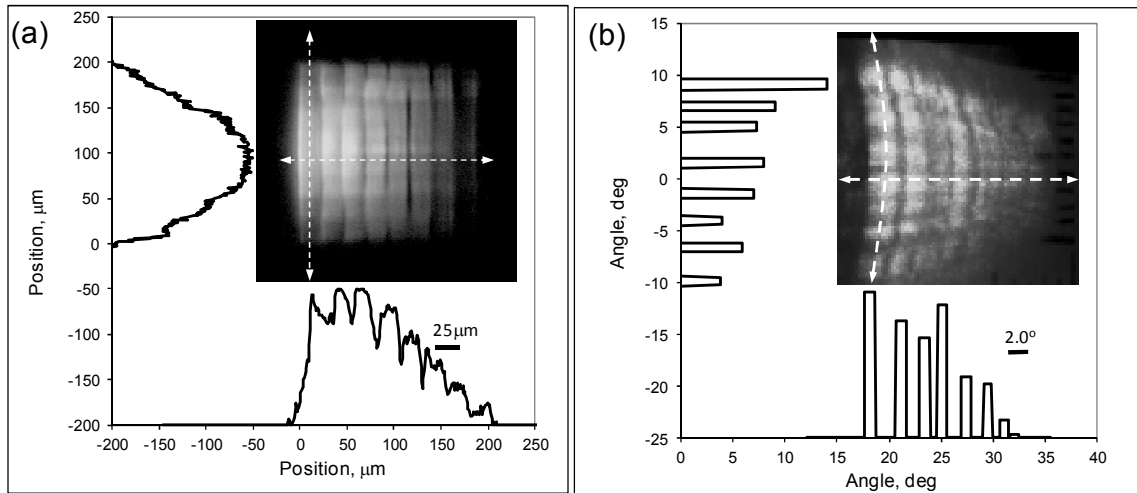
Figure 2.5: a) Near-Field intensity profiles measured in the selected longitudinal and lateral directions from the (8x8) splitting grating array (inserted image of the emitting area); b). Far-Field distribution in two perpendicular directions obtained from the same grating (inserted image of the outcoupled beam)

2.5 2D Uniform outcoupler

Based on the obtained results and taking into consideration the microloading effect, a grating outcoupler with a uniform distribution of the radiation factor could be accurately designed. This technology can be further implemented in the two dimensional splitting grating to reconstruct an 8x8 array. Fig. 2.6 presents an example of the grating duty cycle control with the predicted uniform radiation factor distribution in the longitudinal direction for a 200um grating length. The radiation parameter strength is carefully matched with a corresponding grating duty cycle.
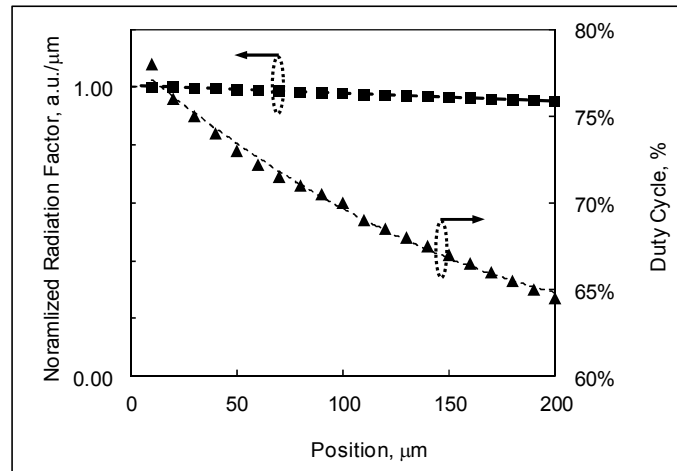
Figure 2.6: Design of the grating for Uniform Near Field profile in the 2D splitting grating

2.6 Multi-emitter array devices

The development of semiconductor based coherent multi-emitters is still of great interest, not only for building compact high brightness light sources applying beam-combining technology (Fan 2005), but is also attractive for design of novel optical scanning systems based on phased array beam steering technique (Wight et al. 1991). Both of these applications will require development of an architecture that is scalable to large sizes, which leads accordingly to higher power and better beam shape. From this perspective, an approach utilizing a two-dimensional (2D) array of phase-locked emitters becomes preferable compared to a linear bar of coherent edge-emitters (Osinski et al. 1994). The most attractive 2D array designs are based on single-wafer processed devices consisting of multiple phase-locked in-plane gain sections spaced by monolithically integrated elements for surface-emitting output, such as 45° deflecting outcoupling mirrors (Mawst et al. 1993) or grating outcouplers (Evans 1991).

Optical outcoupling by gratings has obvious advantages over deflecting mirrors

for coherent surface emitters. Light extraction from an epi waveguide, as well as reflection and transmission, can be controlled by varying the grating parameters. Proper design of transmission through the grating ensures coupling, and thus phase-locking, of neighboring active sections in the direction of light propagation. Depending on outcoupler reflection, coherent operation of individual gain elements varies from a seeded laser in the case of second order Bragg gratings (Evans et al. 1991) to a traveling-wave amplifier for gratings detuned from the Bragg condition (Welch et al. 1990 and Carlson et al. 1990). In the latter case, a monolithic master oscillator power amplifier (MOPA) array approach is utilized to achieve phase-locked multiple outputs.

In this letter, we present a novel 2D MOPA array design providing multiple phase-locked outputs with detuned grating outcouplers. In contrast to 1D linear arrays (Welch et al. 1990 and Carlson et al. 1990), the present device consists of a broad area pre-amplifier connected with a high density 2D array of PAs spaced by grating outcouplers, see Fig. 2.9(a). This pre-amplifier is fed by a high-quality beam from an external light source, which acts as the MO common to all PA waveguides. This approach ensures coherence of the multiple outputs in the lateral direction. The emphasis of this paper is placed on experimental verification of the individual output coherence by investigating the interference pattern between arbitrarily selected emitters. To facilitate a comparison between longitudinal and lateral phase-locking, 1D and 2D arrays were processed in a single lot and interference patterns then compared to a numerical model developed for this purpose.

2.7 1D and 2D MOPA array designs

MOPA multi-emitters were fabricated in 1D and 2D array configurations, see Fig. 1(a) and Fig. 3(a). Each array design consists of a set of 300-µm-long gain elements operated as traveling wave amplifiers. The PAs were patterned with 30-µm- and 10-µm-wide stripes for the 1D and the 2D array, respectively. The periodicity of the gratings between the PAs was detuned from the Bragg condition for efficient outcoupling and low residual reflectivity (Vaissié et al. 2005). This approach is advantageous over the use of second-order Bragg gratings for surface emitting (Carlson et al. 1987). In the latter case, each individual gain section operates as a seeded laser that potentially reduces the mutual coherence. Component fabrication details and specifics of the 976 nm epi can be found elsewhere (Smolski et al. 2012).

Both array designs included a 2-mm-long gain element surrounded on both sides by detuned grating outcouplers. For the 1D array, the stripe width of the long gain section is the same as that of subsequent PAs. As shown in Figure 2.7 (a), in combination with an external mirror providing optical feedback through one of the gratings, this gain element acts as the MO lasing at a narrow spectral line. The processed 1D array chip was flip-chip bonded p-side down on a submount with patterned contacts allowing separate driving of the MO and each PA. Individual adjustment of driving current through each section allows uniform optical power output by precise compensation of the outcoupling and internal optical losses for propagated light. The MO with external wavelength locking defines the spectrum and lateral modal distribution of the multi-emitters. The image of Fig. 1(b) shows the assembled 1D array with inserted near field (NF) image, in operation.
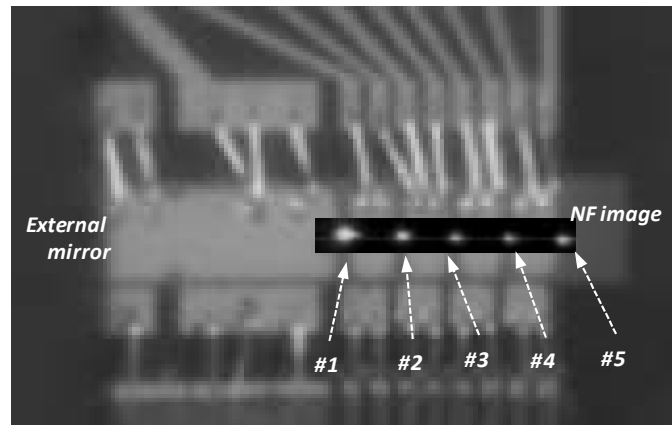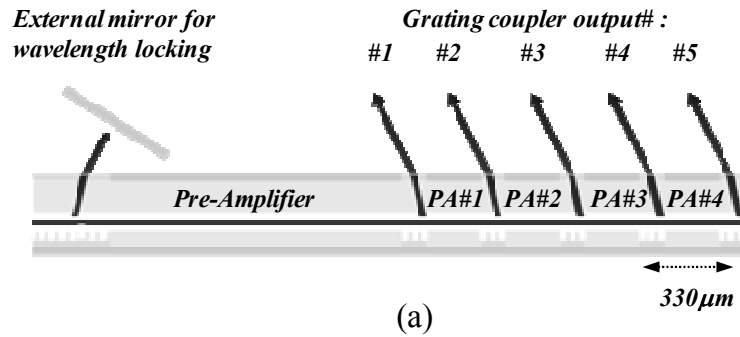
Fig. 2.7 (a) 1D MOPA array cross-section schematics (b) Image of the multi-emitting device with external feedback mirror (inserted: NFs image of the array in operation).

The MO for the 2D array was based on a 900 μm-wide gain section monolithically integrated with multiple PA waveguides. A tilted in-plane configuration of the subsequent grating outcoupler array allows for high density 2D outputs with 100-μm-pitch in each dimension; although individual PA lengths are ~300 μm, see Fig. 2.9 (c) (top). The relatively longer gain sections provide optimum compensation of optical losses arising from out-coupling, scattering, and absorption. The chip was also bonded p-side down on the patterned submount allowing individual driving of MO and 2D PA sections, see the device image of Fig. 2.0 (b). To improve the lateral coherence of the 2D emitters, the broad area amplifier was fed by a high quality beam from a commercial single-

wavelength 976-nm-wavelength diode laser (Innovative Photonic Solutions, Inc.). External optics consisted of spherical and cylindrical lenses designed for amplitude and phase shape matching with the in-coupling grating on the chip.

2.8 Multi-Emitter Experimental results

For experimental evaluation of phase locking the fabricated multi-emitters, we investigated the interference pattern from combination of pairs of array elements. The coherence strength of the selected emitters was determined by the fringe visibility V of resulting interference intensity profile by:

$$V = \frac{I_{max} - I_{min}}{I_{max} + I_{min}} \qquad 2.2$$

where, I_{max} and I_{min} are the maximum and minimum intensity of the fringe patterns respectively, and in the case of equal intensities of overlapped beams $I_1 = I_2$, total coherence between elements corresponds to V = 1.0 [9].

Figure 2.8 presents the interference patterns recorded by a digital CCD infrared camera which was placed in overlapping spots from different pairs of 1D array emitters at a distance of 165 mm from the device. Figures 2.8 (a), (b), and (c) illustrate interference for pairs of farthest, two-PA-spaced, and neighboring outputs. The measured interference periodicities were matched to those estimated from the geometry of the interacting beams. All fringe patterns had maximum visibility of V≅1.0 indicating a high degree of coherence of the emitters in longitudinal direction.
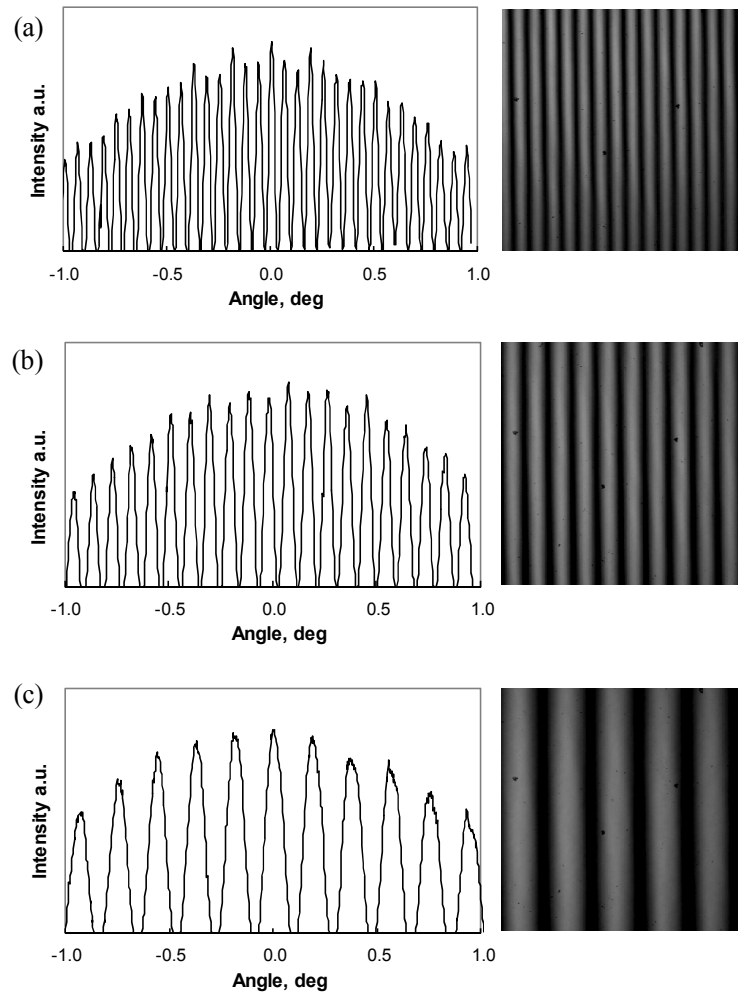
Fig. 2.8. Images of the interference fringes (right) along with corresponding intensity profiles (left) measured in the center of the overlapping spots from different pairs of 1D array outputs shown in Fig 2.7: (a) PA outputs from beams #2 and #5 left open (b) PA outputs from beams #3 and #5 left open (c) PA outputs from beams #3 and #4 left open.

For evaluation of the 2D array coherency, including emitters in the lateral direction, we used a shadow mask with 100 μm diameter holes to select a few discrete outputs located along different narrow-stripe waveguides. Fig. 2.9 (c) (bottom) shows four emitters arbitrary chosen from the 2D array for interference investigation.

(a)

(b)   (c)
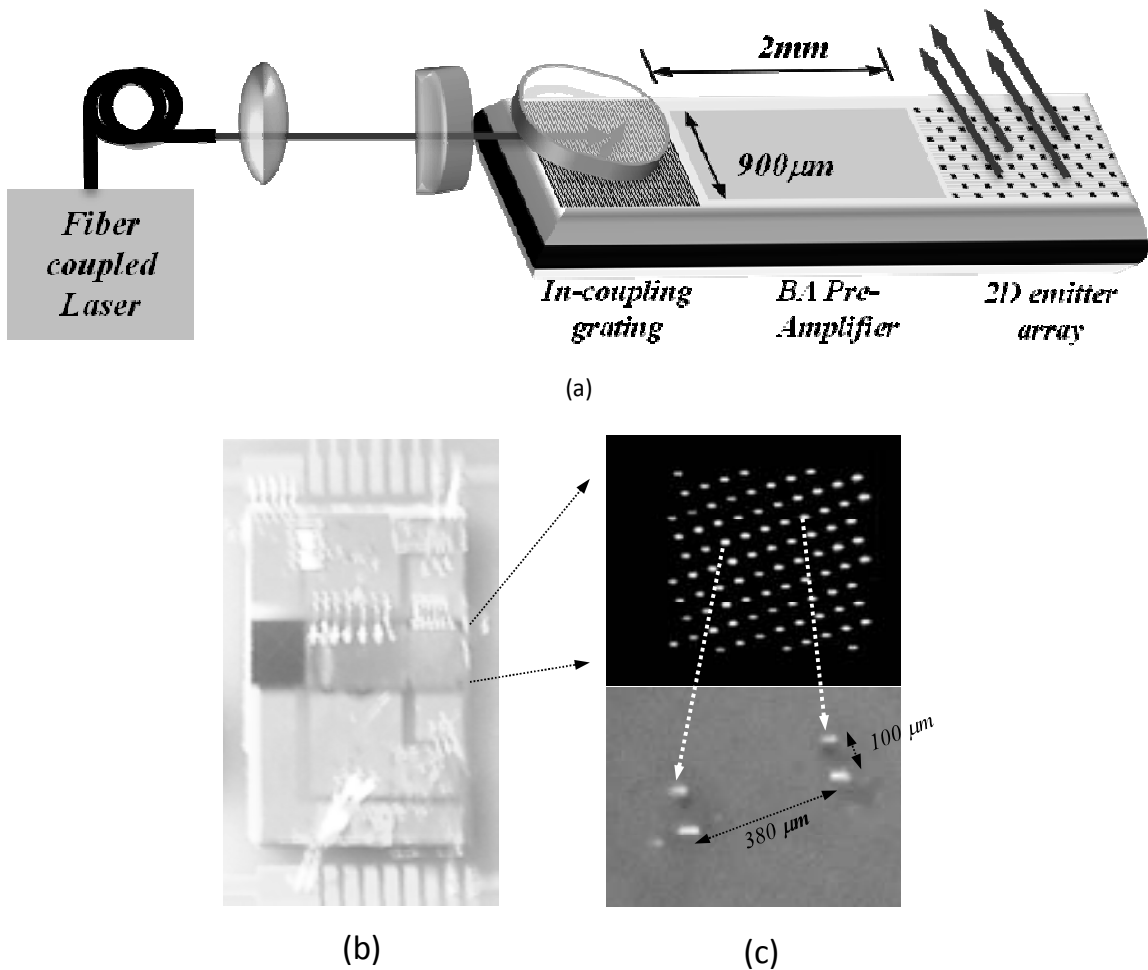
Fig. 2.9 (a) Schematics of the experiment with 2D MOPA array
(b) Image of the bonded 2D multi-emitting device (c) Near Field images of the full two
dimensional sections under pumping conditions (top) and four selected emitters for
coherency measurements (bottom)

The measured interference pattern is shown in Fig. 2.10 (a). The CCD camera was

placed in the overlapping spot on the distance of 117 mm away from the device. Since

the observing plane was in the Fresnel zone, the recorded interference configuration was

compared with the data obtained using a numerical model tool based on the Rayleigh-

Sommerfeld (RS) approach. For numerical simulation, we used an input aperture plane

consisting of four sources as in the experiments and the intensity distribution in the

interference plane was estimated using the RS double integral function. Experimental and modeling results presented in Fig. 2.10 show a close match of the fringe patterns layout. Periods estimated experimentally and numerically for two furthest output spots were accordingly of 0.13° and 0.15°, whereas the interference periods defined by two neighboring spots were 0.53° and 0.54°. The observed interference fringes with periodicities matched with the simulated data, evidence of phase-locking among diverse emitters at various lateral and longitudinal positions, including those situated along different waveguides. However more quantitative analysis of 2D coherence was compromised by low optical intensity from the selected outputs. The weak CCD camera response makes difficult proper profiling of the interference patterns compared with the 1D array.

(a)   (b)
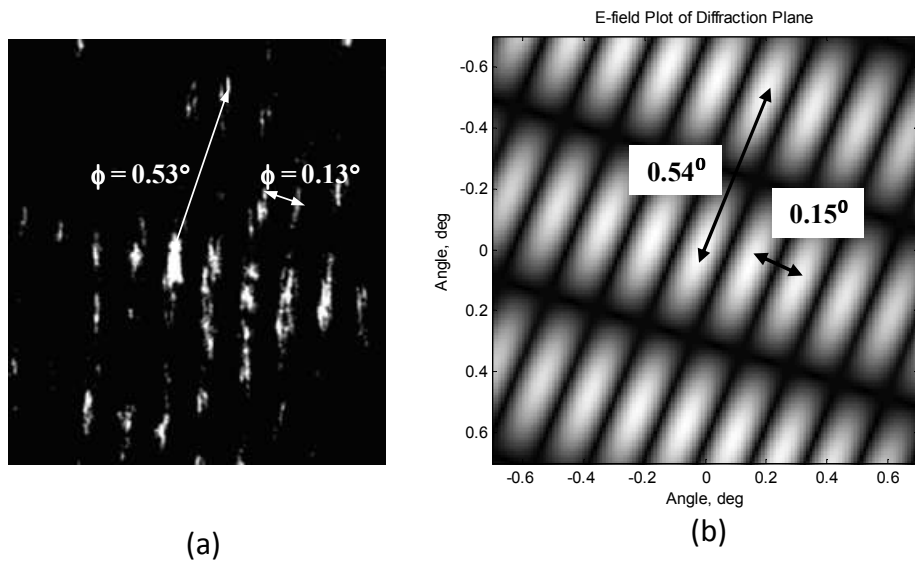
Fig. 2.10 Experimental (a) and simulated (b) interference pattern in the center of overlapping spot from four emitters selected on 2D array.

2.9 Conclusion

The work presented in this chapter has experimentally demonstrated coherent multi-emitter sources based on a MOPA array approach and surface-emission provided by grating outcouplers. High visibility interference fringes were achieved from outputs in both the longitudinal and the lateral direction. To enhance lateral coherence of the 2D array, a broad area gain section was used as the MO seeded by high quality beam from an external laser source.

CHAPTER 3: MODELING

Designing an efficient outcoupling grating structure requires numerical modeling analysis prior fabrication. This step is performed to design and verify AlGaAs/GaAs single-quantum-well graded-index separate confinement heterostructure (SQW GRINSCH) waveguide in terms of confinement and its efficiency with the grating coupler prior to any processing of the wafer. The graded index profile in the waveguide is important as it provides the electric field confinement within the waveguide with no significant change of the Electric field position and profile after mesa was etched. Also, the epitaxial structure of the wafer contains an etch stop layer for the wet etch, allowing precise positioning of the gratings with respect to the waveguide. These dimensions were used in the numerical modeling of the confinement factor and grating coupler design. In this chapter, modeling methods will be used to research the confinement factor; design optimum grating parameters; and discuss the Near- and Far- field diffraction. Detailed descriptions of the modeling methods discussed here can be found elsewhere, (Vaissié, 2005), (O'Daniel 2006).

3.1 Waveguide Numerical Modeling

The wafer refractive index profile is given by the epitaxial grown layers composed of AlGaAs/GaAs GRINSCH. The structure was studied using two methods: Finite Difference (FD) and Galerkin (Kanawo et al. 2001). These methods are based on

the wave equations derived from Maxwell equations, with a given refractive layer distribution:

$$\frac{\partial^2}{\partial x^2}E_0 + \frac{\partial^2}{\partial y^2}E_0 + (k_0 n^2 - \beta^2)E_0 = 0 \qquad 3.1$$

In laser diode structures, lasing polarization is in transverse electric (TE) direction, therefore the field is a function of y, $E_0(y)$ and therefore $\frac{\partial^2}{\partial y^2}E_0 = 0$. Here, x, y, and z are the lateral, transverse, and longitudinal directions of the structure. In case of Galerkin method, for this purpose, let Dirichlet boundary conditions be satisfied. Considering a set of orthogonal functions through the domain of interest

$$\varphi_m(y) = \sqrt{\frac{2}{L}}\sin\left(\frac{m\pi y}{L}\right), \text{where } m = 1,2,3 \dots N \qquad 3.2$$

Where L is the domain width and the condition:

$$\int_0^L \varphi_m \varphi_n \, dy = \begin{cases} 1 & m = n \\ 0 & m \neq n \end{cases} \qquad 3.3$$

Now, substitute the sinusoidal function for the field, $E_0 = \sum_{m=1}^N a_m \varphi_m$ in the wave equation definition and intergrate. The integral can then be simplified using integration by parts resulting in an eigenvalue problem that can be written as:

$$[A][\varphi] = \beta^2[\varphi] \qquad 3.4$$

Galerkin method described serves basis for waveguide structure analysis. Solving the eigenvalue equation 3.4, eigenvalues of the matrix used to determine the propagation constant and therefore the effective refractive index for any given the mode. The corresponding eigenvectors to the solved eigenvectors represent matching electric field profile. The fundamental mode was studied using the waveguide defined by the epitaxial

structure; the refractive index profile is shown in Figure 3.1(a). The structure is labeled on the plot and composed of a 1 μm long p-cladding layer, 0.5 μm GRINSCH with Single Quantum Well (SQW), 1.2 μm long n-cladding followed by GaAs substrate. The design of the epitaxially grown waveguide also incorporated an etch-stop layer allowing precise location placement of the grating couplers with respect to the waveguide. The SQW layer is a 20 nm thick InGaP lattice matched to $Al_xGa_{1-x}As$ layers, with high etch selectivity to GaAs. This position is necessary for the grating coupler designs discussed in section 3.2. The location of the etch stop is 250nm above the GRIN and it is visible as a notch in the refractive index profile on figure 3.1 (a). The dotted line represents the etch stop layer for reference. The two conditions considered are the un-etched structure representing the active region, and wet-etched profile representing the grating coupler region.
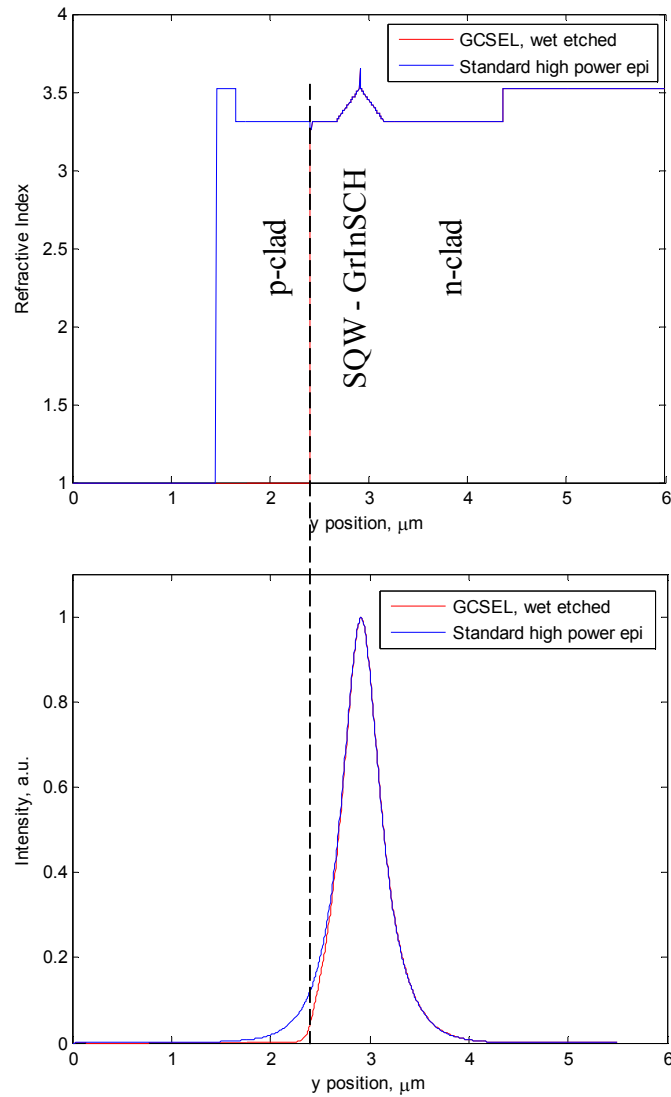
Figure 3.1 (a) Refractive Index profile of GaAs/AlGaAs structure (b) Intensity
distribution comparison between a High Power Laser

Figure 3.1(b) presents the numerical results of the corresponding fundamental
mode field intensity profiles for the two refractive index structures. Unlike most other
epi- structures, after p-clad removal the waveguide remained single-mode due to
advantageous GRINSCH design. It is also important to note that the electric field does

not move into the n-cladding, retaining the confinement within the waveguide. The effective refractive index of the mode was computed to be of 3.317.

The transverse QW confinement factor Γ is defined as an overlap of the optical-mode profile with the gain region of the laser. Here, the relation between modal gain g_{modal} and material gain g is $g_{modal} = g\Gamma$. In the active layer consisting of a quantum well with a thickness of around 10nm, confinement factor values are normally in the order of a few percent, 2-3%. The general equation for the quantum well confinement factor is expressed as:

$$\Gamma_{QW} = \frac{\int_{QW} |E(x)|^2 dx}{\int_{-\infty}^{\infty} |E(x)|^2 dx} \qquad\qquad 3.5$$

From above equation, the Quantum Well Confinement Factor is estimated of ~2.3% for both selections. Additional analysis shows that further etching into 250-300nm the p-cladding, closer to waveguide, also does not significantly affect the confinement factor leaving room to design the next step, specifics for grating outcoupler.

3.2 Outcoupler Grating Modeling

Grating coupled surface emitting lasers (GCSEL) were introduced in Chapter 1.5. Surface-emission is achieved by fabricating grating outcouplers, with a grating period detuned from the Bragg condition. Another condition is to select only the first order to be diffracted in the substrate. This is necessary to reduce the effective reflection from the grating back into the cavity. Choosing the period, d_{gc}, of the grating between the first

order Bragg condition and condition of one diffraction order, the conditions to be satisfied are:

$$\frac{\lambda}{2n_{eff}} < d_{gc} < \frac{2\lambda}{n_s + n_{eff}}$$ 3.6

Where, n_{eff} is the effective refractive index of the grating region; n_s is the refractive index of the substrate; and λ is the operating wavelength. The substrate refractive index is 3.52; the effective refractive index was computed in section 3.1 and is 3.317. For a wavelength of operation of 975 nm, the grating period should be between 145 and 285 nm. Three grating periods were chosen for numerical optimization of the grating coupler fabrication parameters, $d_{gc} = 260$ nm, 270 nm, and 275 nm. These selections were done due to reasonable fabrication tolerances, while remaining within a small outcoupling angle, θ of less than 25°, defined by:

$$\sin(\theta) = \frac{\lambda}{d_{gc}} - n_{eff}$$ 3.7

The grating coupler was studied in terms of the outcoupling length parameter with a Rigorous Coupled Wave Analysis (RCWA). The outcoupling length L (μm), or sometimes referred to as the grating strength, is defined in terms of the power leakage rate, α_{grat}^{out} specifying the 1/e intensity fall-off point. The relation between outcoupling length and leakage rate is the following:

$$\alpha_{grat}^{out} = \frac{1}{L_{grat}^{out}}$$ 3.8

Formulation for the RCWA numerical algorithm for a similar refractive index profile was described elsewhere, (O'Daniel, 2006). As in section 3.1, due to nature of the

SQW only the TE polarization is supported in the structure and therefore numerical formulation is performed for TE case.

(a)

(b)
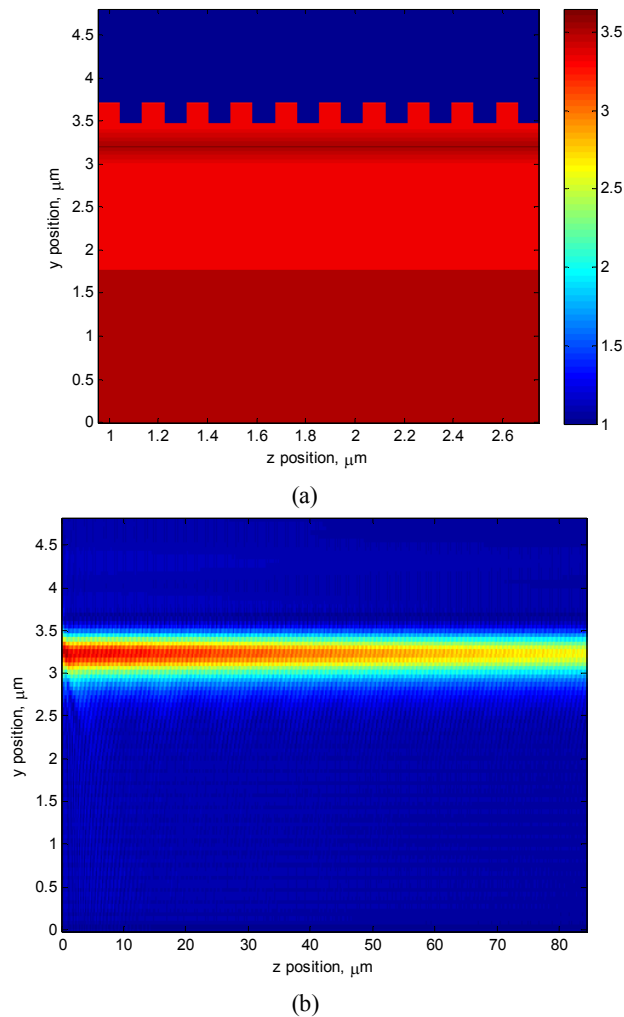
Figure 3.2 :(a) Real Refractive Index profile of the first ten grating periods in GaAs substrate, $d_{gc} = 270$nm with etch depth of 250nm, 50% Duty Cycle (b) Field intensity in the laser waveguide for the first 85μm.

Figure 3.2 illustrates the numerical computation analysis of a sample grating with fixed grating parameters: 270nm grating period, 250nm etch depth with 50% Duty Cycle. Figure 3.2(a) shows the refractive index of the first ten grating periods in the simulated

profile. Figure 3.3(b) demonstrates how the field intensity couples into the substrate and the intensity falls off as the light propagates through the waveguide in the z-direction. The intensity of the propagating mode along the z-direction may be expressed in terms of power as:

$$P(z) = P_0 e^{-\alpha z}$$

3.9

The grating efficiency is optimized in terms of the outcoupling length, which should be less than waveguide absorption (Chapter 5.3.3). The outcoupling length simulated results for the fabrication design can be expressed as a function of etch depth and duty cycle, $L(\mu m) = f(ED, DC)$. Here, the duty cycle is defined as the tooth width per period width multiplied by 100. The effective coupling length requirement to be satisfied is on the order of $100 - 200um$. Shorter grating sections designed for the array devices require a shorter outcoupling length to provide high power output in the region. A Point of interest is that to have an outcoupling close to or less than $100\mu m$, which is significantly shorter than waveguide absorption. The three chosen gratings were numerically simulated in terms of etch depth and duty cycle. Two dimensional arrays of outcoupling length parameter were obtained for each case. Figure 3.3(a) illustrates a two dimensional plot of the Outcoupling length of a 270nm period grating in terms of etch depth vs. duty cycle. The Outcoupling Length plotted in Figure 3.3(a) is in logarithmic scale, hence any value x represents an actual outcoupling length of 10^x (μm). The plot was extracted in details for two fixed duty cycles and represented in terms of etch depth only, Figure 3.3(b), where blue and red curves represent duty cycle of 50% and 60%, respectively. From these plots, the duty cycle in the range of 30% to 50% does not affect the grating performance significantly and the optimal grating etch depth should be on the

order of 250nm. This is not the case for duty cycle range of 50% to 80% where small variations can significantly reduce the grating performance. This effect was considered during the electron beam lithography and grating etch steps to stay in aforementioned range.
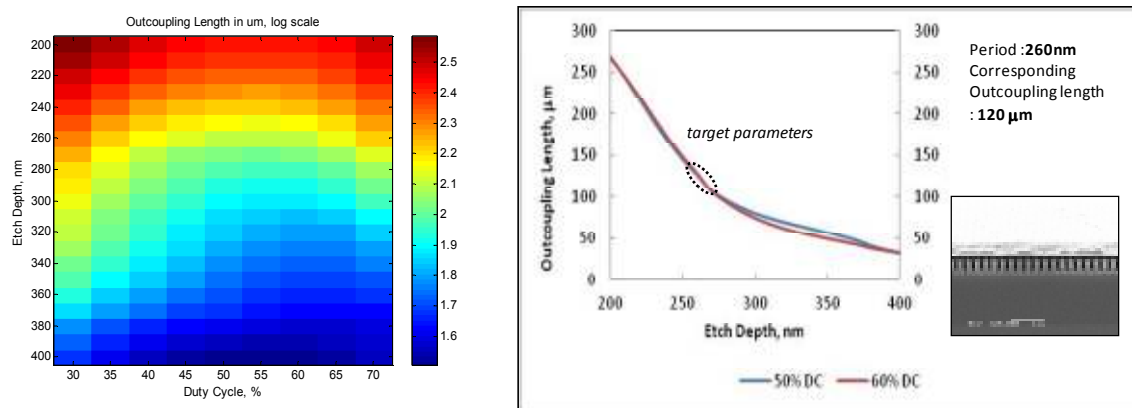
Figure 3.3 (a) Outcoupling length simulation as a function of the Etch Depth and Duty cycle of the outcoupling grating, represented in logarithmic scale (b) outcoupling length distribution for two selected Duty Cycles, 50% and 60%

Two more periods were modeled similar to 270nm period grating, represented in figure 3.4. Grating performance was plotted in terms of outcoupling length given a range of etch depths. For feasibility and fabrication tolerances, the duty cycle parameter was fixed at 50%. Resulting plot of the three designs shows a similar trend in all three cases. Therefore, already chosen etch depth of 250nm is suitable for outcoupling length to be shorter than 100mm for all three grating periods. These patterns parameters of three grating periods with duty cycle of 50% and grating etch depth of 250nm were further processed, studied and characterized; data will be presented in chapters 4 and 5.
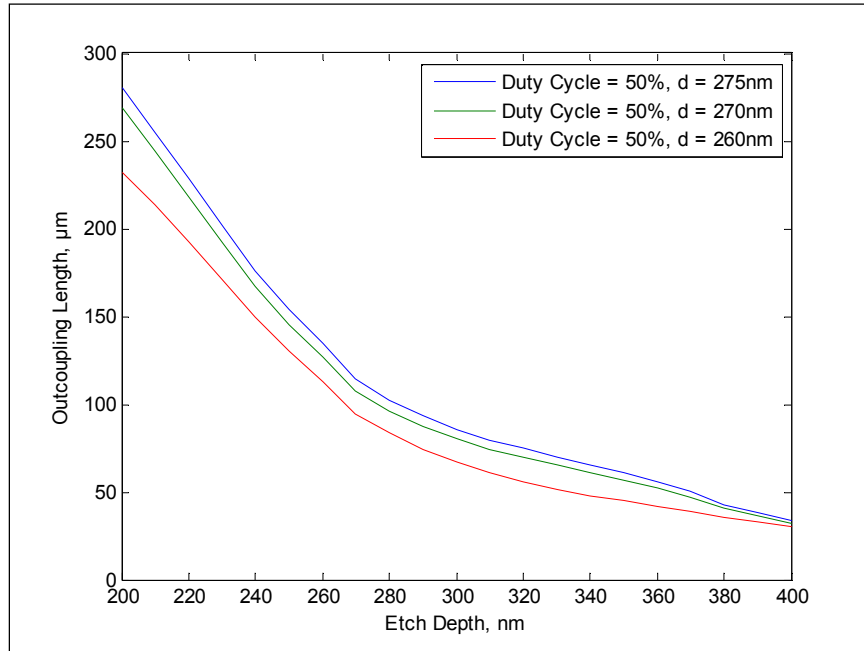
Figure 3.4 Outcoupling length depending based on the grating etch depth, given three different periods with Duty Cycle of 50%

3.3 Far Field Propagation

The Work discussed herein also requires numerical simulations of Near- and Far-Field profiles to understand the device performance and characterize the coherence strength. Chapter 2 presented results of 1D and 2D arrays of devices with experimental and numerical results. These and more results were studied and compared using the Fraunhoffer and Rayleigh − Sommerfeld diffraction formulations. The Fraunhoffer approximation is defined in (Goodman, 1996). Taking function $U(x', y')$ on a given input aperture distribution in coordinates x' and y', the far field profile $U(x, y)$ at distance z away can then be calculated in the observation plane, x and y as following:

$$U(x, y) = e^{jk_0 z} \frac{e^{j\frac{k_0}{z}(x^2 + y^2)}}{j\lambda z} \iint\limits_{-\infty}^{\infty} U(x', y') e^{-j\frac{k_0}{z}(xx' + yy')} dx' dy' \qquad 3.9$$

Where, $k_0 = \frac{2\pi}{\lambda}$ and λ is operating wavelength. However, provided aperture dimension, D, Fraunhoffer approximation is only valid at distance:

$$z > \frac{2D^2}{\lambda} \qquad\qquad 3.10$$

where D is the input plane aperture. For a example: for two outputs spaced 330 mm apart at operating wavelength of 980 nm, the observation distance z must be larger than 220 mm. In order to compare the results or study intensity profile in the Fresnel range, another numerical approach used was Rayleigh – Sommerfeld (RS) diffraction. RS approach is advantageous due to its compatibility in Fresnel and Fraunhoffer range. This numerical approach is based on the Kirchhoff boundary conditions and implementation of Greens function (Gaskell, 1978). The far field distribution may be estimated as:

$$U(x,y) = \iint\limits_{-\infty}^{\infty} U(x',y') \frac{z}{j\lambda(r_{12})^2} e^{jk_0 r_{12}} \, dx'dy' \qquad\qquad 3.11$$

Where, while z is the distance between the aperture and observation planes, r_{12} is defined as a slant distance between two points in aperture and observation planes

$$r_{12} = z\left[1 + \left(\frac{x-x'}{z}\right)^2 + \left(\frac{y-y'}{z}\right)^2\right]^{1/2} \qquad\qquad 3.12$$

In both scenarios, the integrals were computed using numerical trapezoidal integration in Matlab. The comparison of modeling and experimental results was presented earlier, Chapter 2.3.

CHAPTER 4: FABRICATION

Grating Coupled semiconductor device fabrication is an involved process. Sections of this chapter will discuss important aspects of fabrication and process parameters used for this research. Mask designs are drawn to meet the specified criteria for mesa-formation, contact metallization, and patterning. Figure 3.1 depicts a general flowchart diagram of the device fabrication. First, the wafer was cleaned and cleaved into 1 in by 1 in samples of devices, also referred in this dissertation as a block. The block is thinned down to a thickness of 150 μm to reduce absorption by the GaAs substrate. Mesa formation was done by photolithography for patterning and wet chemistry etch down to etch stop. Next, a silicon nitride (Si_xN_y) was deposited as an insulating layer. Openings were patterned for the p-contact and grating sections. The p-contact metallization required negative photoresist patterning prior to deposition and a liftoff process was performed after metal deposition. The grating couplers were patterned using electron beam lithography and etched in Chlorine (Cl) – based process in III-V ICP system. To finish the p-side processing, a high reflection coating composed of Si_xN_y and Gold (Au) were deposited [Vaissié, 2005]. Similar to previous steps, the n-side was patterned with contact followed by rapid thermal annealing (RTA). The fabrication of a block is completed with a deposition of a SiN antireflection coating (AR) to improve device efficiency. Each step summarized in the flowchart is described in this chapter. In this research, up to eight lithography steps must be performed to process a full block of devices. Due to the fragility of the GaAs material, and to improve the yield, most

processes involve the mounting of a piece onto a Silicon wafer substrate with a planarizing Futurrex PC3 resist.

p- Side Process:	n- Side Process:
Mesa Formation	Wafer Lapping / Polishing
SiN Insulating Layer	n – Contact Metallization
p – Contact Metallization	RTA
E-beam Lithography	SiN Antireflection coating
Grating Couplers Etch	
High Reflection Coating	Assembly and Test
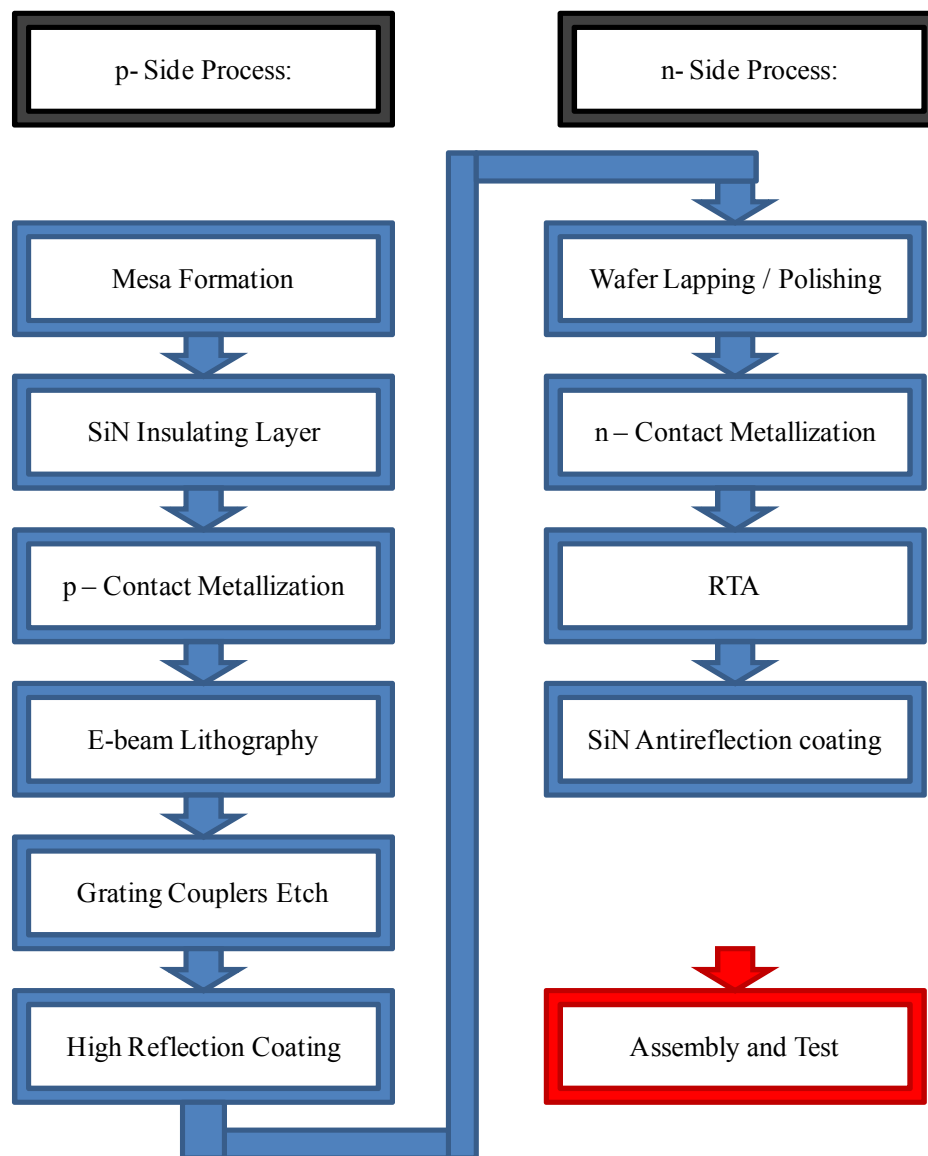
Figure 4.1 Grating coupled surface emitting laser diode fabrication flowchart

4.1 Lapping and Polishing

Thinning the device is necessary to reduce the absorption of the light as it propagates through the substrate. The lapping step is the process of thinning the device, while polishing is performed to produce a mirror-like surface finish on the n-side of the wafer. It is also a helpful step for future scribe and brake the block into individual diodes prior to assembly and bonding. For that purpose, a process recipe was developed to thin down the wafer from ~650 μm to ~150 μm thick. A South Bay Technologies 920 8" lapping and polishing machine with a lapping fixture was used allowing mounting and processing samples with diameters up to2". A GaAs substrate was first cleaved to a processing size of 2cm by 2cm square piece and mounted p-side (epi-side) down on a Silicon wafer holder using PC3 resist. An Si carrier is necessary to eliminate GaAs from breaking; to keep the epi p-side of the wafer clean from polishing residue; and to mount to a stainless steel polishing mounting block. The puck was then mounted onto fixture and placed on a 30mm grit diamond polishing pad. The micrometer on the fixture was adjusted to remove ~300μm and the sample block was then lapped down to ~200-220 μm thickness allowing another ~50-70 μm for fine polishing of the n-side to a mirror finish. The diamond polishing pad was swapped to a Pace Technologies NYPAD pad for fine polishing. Diamond paste grit 6-12μm was deposited onto a pad and the block was further polished to a thickness of ~170-180μm. The NYPAD polishing pad was swapped to a DACRON polishing cloth. Diamond paste grit 2-4μm was deposited onto cloth and the block was polished to a mirror finish. Several inspections were made under an Olympus microscope to make sure the n-side was polished with no surface scratches or

defects. The final step is to prepare the sample for the lithography process using a MasterTex polishing cloth, colloidal silica slurry and diluted NaOCl solution. This step removes the GaAs residue as well as provides a chemical-mechanical polishing to smooth out any grooves (Higuchi et al. 1989, O'Daniel 2006).

4.2 Contact Lithography

Photolithography is an essential process during the laser diode fabrication. In the scope of this work all seven exposure steps, excluding the e-beam, were covered by two photoresist types and therefore two matching recipes. The two photoresist types used in contact lithography are a Futurrex NR7-1000PY negative and a Shipley 1813 positive photoresists. Table 4.1 depicts the basic assignment of the resist for an individual process step. The necessary resist layers perform: (1) mesa wet etching masking, (2) open p-side Silicon Nitride protective and isolating layer for contact, (3) p-side contact metal liftoff, (4) p-side Silicon Nitride high reflection layer opening for contact, (5) p-side high reflection metal coating alignment marks liftoff opening, (6) n-side contact metal liftoff, and (7) Antireflection Silicon Nitride coating opening for the contacts and assembly.

Table 4.1. Process steps depicting use of resist and its purpose in fabrication steps

#	Process Description	Purpose	Resist Type
	P-Side Processing:		
1	Mesa etch	Mesa Formation	S1813
2	P-side Si_xN_y opening	p- Si_xN_y open	NR7-1000PY
3	P-side contact lift-off	p-contact	NR7-1000PY
4	P-side HR (opening for contact)	p-HR Si_xN_y	NR7-1000PY
5	P-side HR metal deposition	p-HR Metal	NR7-1000PY
	N-Side processing:		
6	n-side contact lift-off	n-contact	NR7-1000PY
7	AR n-side Si_xN_y (open for contacts)	n-AR Si_xN_y	NR7-1000PY

The sample was prepared and cleaned with an acetone and isopropanol rinse prior each photolithography step. Once clean, the sample was mounted onto a Silicon carrier piece using planarizing Futurrex PC3 resist to provide mechanical stability of the GaAs block. The resist was spun at 3000rmp on a Silicon piece and placed on a hotplate at a temperature of 115C. The GaAs block was then carefully mounted on top of the Si-carrier, making sure there were no air gaps between two surfaces. Excess resist was

cleaned off by an acetone and isopropyl rinse. The clean sample was then ready for photolithography.

For the mesa formation a positive Shipley 1813 photoresist was used as an etch-mask. The sample was spin coated at 3000RMP and prebaked on a hotplate at 115C for 90 seconds. The block was then carefully aligned to the contact photomask for the matching pattern configuration, in this case mesa. In this step the alignment was performed by the edge of the cleaved sample such that the patterns are along the $(01\bar{1})$ direction in crystal plane. This alignment is important due to the sidewall profile of the crystal formed by wet etch. In this research, the stripes are oriented so that the longitudinal direction is along $(01\bar{1})$ so that there is a smooth index change profile from diode to grating. The contact lithography exposure was performed using a Quintel Ultra7000 i-Line mask aligner. The sample was exposed with a 125 mJ/cm^2. The block was then post-exposure baked at 115°C for 60 seconds. Resist was developed using mixed one part MICROPOSIT 351 developer to five parts water for 90 seconds. The sample was rinsed with DI water and blown dry with nitrogen and was then ready for the mesa wet etch.

For processes such as metal liftoff and nitride etch, a negative photoresist, Futurrex NR7-1000PY was used. The block was first treated with a Hydrogen Chloride (HCl) solution to remove the natural oxide layer for future adhesion of metal deposition step. A bath was performed for 60 seconds, followed by de-ionized (DI) water rinse. The sample was inspected to see if the water beads up on the surface as it runs across GaAs. The process may be repeated if the effect is not observed. The resist was coated on GaAs at 4000RPM and prebaked at 150C for 70 seconds. The block was then carefully aligned

on the Quintel contact mask aligner by using alignment marks to the next desired mask and exposed at 150mJ/cm^2. For the n-side contact patterns, a backlit IR source front-to-back alignment feature was used when p-side metal contacts and alignment marks are visible. The block was then post-exposure baked at 100C for 70 seconds. Resist was developed using mixed three parts Futurrex RD6 developer to one part water for 120 seconds. The sample was rinsed with DI water and blown dry with nitrogen and bathed in HCl solution to remove any formed excess natural oxide layer. The sample was now ready for metal deposition or nitrides etch, depending on step order.

4.3 GaAs Wet etch

A mesa is required for current confinement and the excess p-cladding was removed by the wet etching technique. The wet etch step was designed with an In$_x$Ga$_{1-x}$P etch stop layer to prevent etching too deep into the waveguide ensure. The block was patterned with a positive Shipley S1813 photoresist with the process described earlier. Wet etching was then performed by one part phosphoric acid (H$_3$PO$_4$), one part hydrogen peroxide (H2O2) and six parts DI water solution. The sample was submerged into the etch solution for 90 seconds to remove ~1μm of the Al$_x$Ga$_{1-x}$As cladding layer. The masking layer of resist was removed by an acetone and isopropyl solvent rinse. Fig 4.2(a) depicts a cross section of the single device, while Fig 4.2(b) shows the cross section of a (01$\bar{1}$) orientation after wet etch.
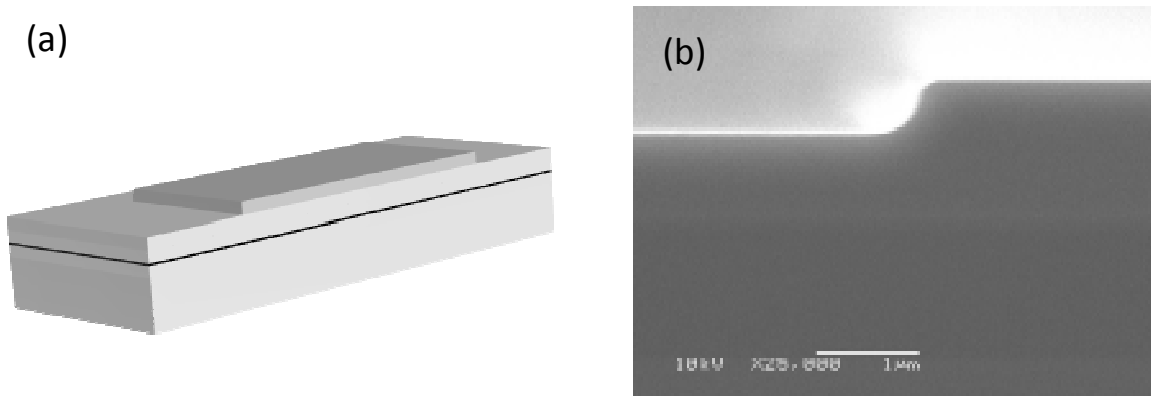
Figure 4.2: Mesa formation (a) Illustration of the wafer sample wet etched (b) SEM image of the cross section sample after wet etching in ($01\bar{1}$) orientation

4.4 Metallization and RTA

The p-side and n-side metallization procedure of the sample are similar and therefore are described in this single section. The block was prepared with a NR7-1000PY resist for a future liftoff process, where the photoresist under the film was removed with solvent taking the unnecessary film with it. This resist has a negative sidewall profile and therefore is great for liftoff. Prior to metal deposition, the block was again treated with HCl solution to remove the oxide layer. A chlorine bath was performed for 30 seconds, followed by DI water rinse. Contacts were mounted on a carousel and deposited using Kurt J. Lesker PVD 75 thin film deposition system. The sample was deposited with ~20 nm titanium (Ti) as an adhesion layer, ~20nm nickel (Ni) for a diffusion layer and ~150nm gold (Au) as a conducting layer.

The sample was then ready for a liftoff step. It was then placed in the acetone bath for 6 hour period allowing acetone to reach and dissolve resist under the deposited metal. Typically, time-frames required for this process are six hours or more. The block was carefully removed from acetone and rinsed with IPA. This is a crucial and very

challenging step as metal may stick back on surface and become impossible to remove. In some cases, a low power Ultrasonic bath in Acetone may be helpful to remove excess metal.

After metal contacts were deposited on both n- and p-sides, a Rapid Thermal Annealing (RTA) process designed specifically for these devices was performed. The block was cleaned with Acetone and IPA rinse and was annealed at a temperature of 400°C for 30 seconds.

4.5 Grating Fabrication

Depending on preferences or requirements, the process flow may be interchanged, where grating fabrication may be performed after the mesa wet etch, described in 4.3 or after p-contact metallization. The grating outcouplers designed have periods from 260 nm to 275 nm, with line-widths ranging from 50 nm to 130 nm. These periods are relatively small and cannot be patterned using conventional photolithography techniques. In order to realize such small features, electron beam (ebeam) lithography was chosen. In our previous works (Vaissié, 2005 and O'Daniel, 2006) the Leica 5000+ EBPG was used located in University of Central Florida. For the purpose of this work, a JEOL JBX-9300FS tool located at Georgia Tech was chosen. JEOL system is preferable and advantageous in terms of remote access for job-file creation and compilation capabilities as well as its close commute location.

Grating patterning was done with ZEP-520A positive ebeam resist. The resist performs well as a masking layer for shallow etch-depths of GaAs. For e-beam lithography, the GaAs block was again mounted on a Si carrier wafer. Once the excess PC3 resist is removed, it is important to perform a short O_2 'descum' process to ensure

the sample is free of any resist residue from previous sources. The sample was then coated with ZEP-520A and spun at 4000 rpm, followed by post-applied bake on a hotplate at 180C for 2 minutes. Next, the sample block was mounted onto a piece cassette carrier and the angle aligned to the nearest ½ of a degree. This is necessary for accurate grating patterning alignment with respect to alignment marks. This angle was further improved once in the chamber by the stage system alignment prior to lithography. The cassette was placed onto the platform from which it is automatically loaded onto the stage in the chamber.

To optimize the grating patterning and take into an account microloading effect, described in Chapter 2.5, in the fabrication a dose matrix was performed with necessary correction parameters due to proximity effect for GaAs substrate. The appropriate dose for gratings ranges from 165 to 180 $\mu C/cm^2$ depending on the period size. The patterns can then be written at 165 $\mu C/cm^2$ and a sample grating patterned is demonstrated in Fig. 4.3(b).
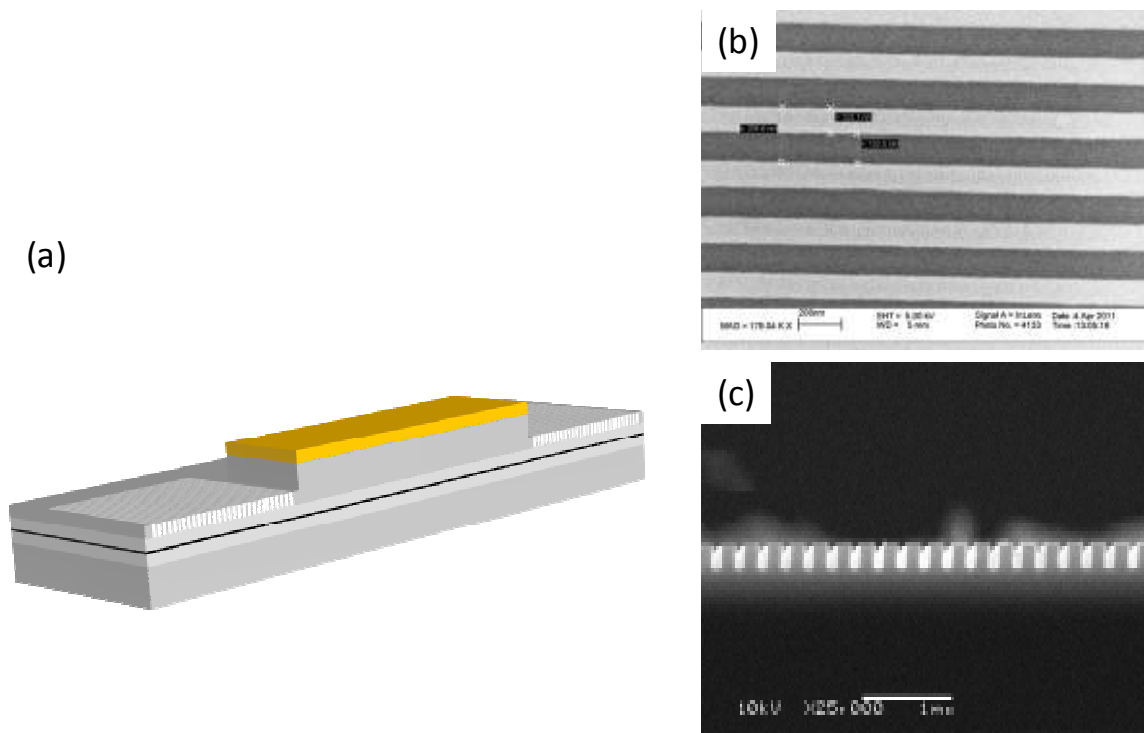
Figure 4.3: Grating fabrication step (a) SEM Illustration of a wafer after grating etch (b) ZEP520 resist profile after exposure and develop (c) SEM of the transfer etched grating section

4.6 GaAs DRIE etching

Once the gratings were patterned with ZEP-520A, the patterns were transfer etched into the substrate. The etch was carried out using Surface Technology System (STS) Inductively Coupled Plasma (ICP) system with a Chlorine based plasma. Process parameters are as follows: 40 sccm Boron trichloride (BCl_3) and 16 sccm Helium (He) flow rates; at a chamber pressure of 10mT with an ICP power of 400W and a RIE power of 60W. Since the chamber is used frequently, etch rates vary and therefore a control sample etch was performed. Etch rates were approximately of 100nm per minute with etch selectivity to resist ~3:1. Excess resist was removed by rinse with Acetone and IPA. Figure 4.3(a) illustrates the device cross-section schematic after Grating Couplers have

been etched into the substrate. Fig. 4.3(c) shows a cross section SEM image of a grating coupler after etch and clean.

4.7 High Reflection Coating

Once p-side gratings were patterned, high reflection silicon nitride (Si_xN_y) and metal layers were deposited onto the surface. This is a necessary step to improve the device performance as demonstrated in (Evans et al. 1989, Vaissié et al. 2005). For efficient high reflection coating, the gratings were then covered by quarter wave dielectric layer using Surface Technology System (STS) Plasma Enhanced Chemical Vapor Deposition (PECVD) system. The coating thickness required was 130nm and was calculated based on refractive index of a substrate and a silicon nitride layer. Deposition was performed for 12 minutes and 54 seconds at a rate of 0.1679 nm/second. The process parameters used to deposit silicon nitride (Si_xN_y) are: 2% Silane (SiH_4) flow rate of 1980 sccm; Ammonia (NH_3) flow rate of 55 sccm; a chamber pressure of 900mT; and a high frequency RF power of 20W.

(a)

(b)
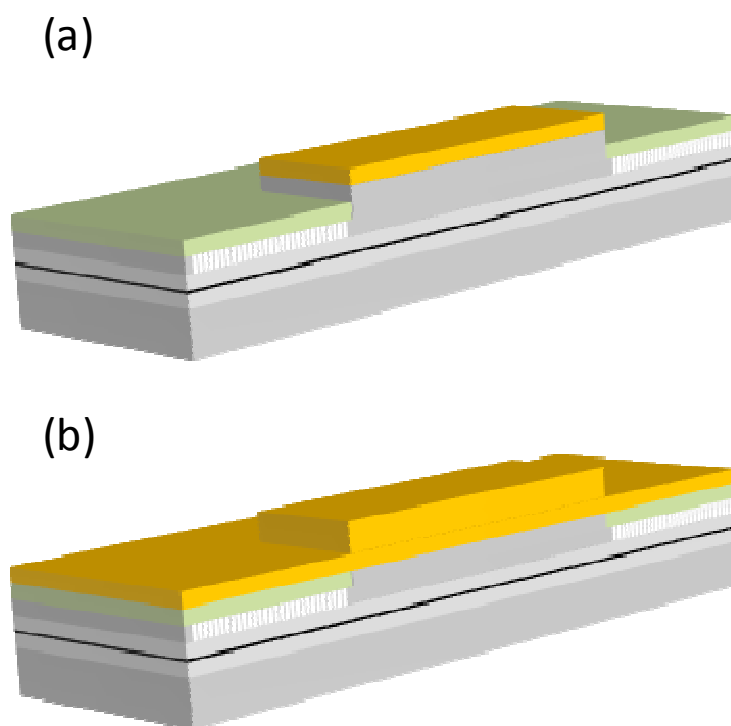
Figure 4.4: High reflection coating illustration (a) Si_xN_y layer deposited and contact pads are opened (b) Metal deposited over the nitride

After the Si_xN_y deposition, a lithography step was performed using NR7-1000PY photoresist, described in Section 4.2. The resist acts as a masking layer to open the p-side contact pads. The nitride layer was etched using a Uniaxis Versaline ICP with: 36sccm CF_4 and 4sccm O_2 flow rates at a pressure of 40mT and RIE power of 100 W. Etch rates are on the order of 170nm/min. Excess resist was removed with Acetone and IPA. Figure 4.4(a) shows a cross-section of the sample after the nitride deposition is complete and contact pads are opened. Fig. 4.5 shows an actual block image after high reflection nitride (Si_xN_y) layer was deposited prior p-side high reflection metallization and completion.

High reflection metal contacts were deposited using a Kurt J. Lesker PVD 75 thin film deposition system. The sample was deposited with ~5nm chrome (Cr) for metal

adhesion to GaAs and ~250nm gold (Au) layers. This completes the High Reflection coatings and p-side fabrication. This stage of process is illustrated in fig. 4.4(b).
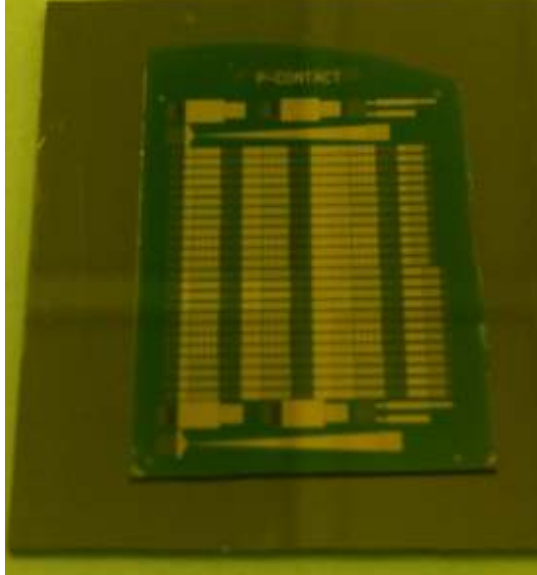
Figure 4.5. Sample block image with devices after p-contact, grating etch and high reflection nitride (Si_xN_y) deposition

4.8 Antireflection coating

Once n-side contacts are deposited, an anti-reflection nitride (Si_xN_y) sub-wavelength layer was deposited onto the block. The details of device performance improvement are described elsewhere [Vaissié, 2005]. Surface Technology System (STS) Plasma Enhanced Chemical Vapor Deposition (PECVD) system was again used to deposit 125 nm nitride. Futurrex NR7-1000PY resist was patterned and contact pads were opened with the same RIE process as in previous section. Excess resist was removed using Acetone and IPA baths. This step concludes the n-side and overall fabrication routine of the block. Fig 6 gives a cross-section illustration of a fully processed sample and Fig. 4.7 is an image of n-side of the fully processed block.
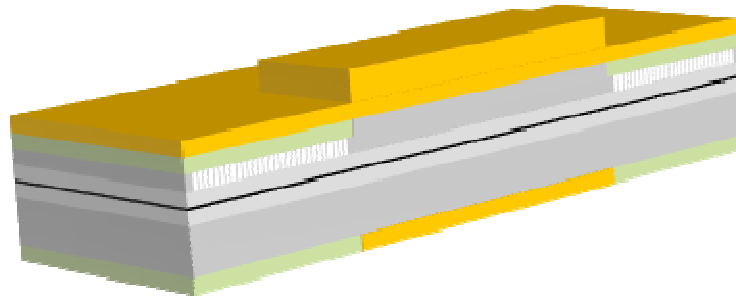
Figure 4.6: Sample cross-section device depiction after n-side processing is complete with contact and antireflection coating.
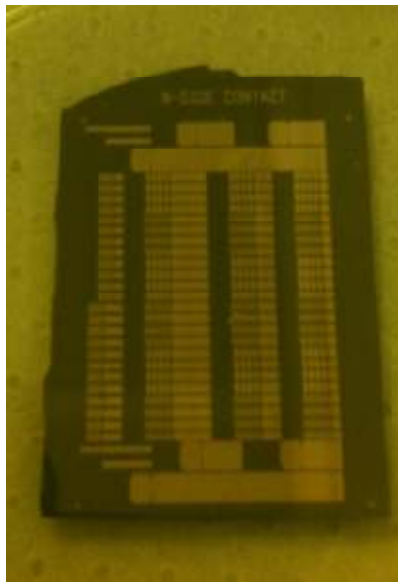
Figure 4.7. Sample block image of the n-side after the fabrication processes are complete.

4.9 Device Assembly

After the lithographic, etching, and deposition steps are complete, the block was cleaved into devices using a Loomis Industries LSD-100 scribe and break tool. The devices were then bonded p-side down on a Beryllium Oxide (BeO) submount with pre-deposited gold-tin (Au-Sn) solder using a Fine Tech Flip Chip Bonder. The n-contacts

were wired to the submount with a 1 mil diameter gold wire using a K&S wire bonder. These devices were then ready for testing and characterization.

4.10 Conclusion:

In this Chapter, the entire routine performed for device fabrication was described. The processes outlined are: lapping and polishing, lithography steps, mesa etch, contact deposition, grating patterning and etching, high reflection and antireflection coatings.

CHAPTER 5: CHARACTERIZATION

5.1 Device Assembly and Instrumentation:

The previous chapter described the fabrication process involving GCSELs. This chapter presents the performance characteristics of the processed devices. The block was first cleaved into devices using a scribe and break tool and bonded p-side down on a BeO submount with patterned gold contacts and pre-deposited Au-Sn solder. The device's n-side was wired to the separate contact pad on a submount with a 1 mil diameter gold wire. The device was then mounted onto a holder with a Thermo-Electric Cooler (TEC) and water cooled copper heat sink. Normal operating temperature of the device was maintained at 20°C. The holder was mounted to a stage with two or more degrees of translation freedom necessary for data recording. Light-current (L-I) and Voltage-Current (V-I) measurements were performed using a PC-controlled automated testing setup including a Newport 5060 laser diode driver, Newport 8008 modular controller with multiple Newport 8600C laser diode drivers for array testing, and a DEI PCX7410 Laser diode pulse driver. Depending on the pumping requirements based on the structure of individual device, CW or a pulse mode operation can be chosen. Cooling was performed by a closed-loop liquid chiller by Melcor and a Newport 350 TEC controller. Optical power measurements were done using Ophir LaserStar Optical power meter and compatible photodiode IR sensors and thermal heads. Near- and Far-Field data was recorded using a Spiricon framegrabber and compatible cameras by IR Sony and COHU.

Spectrum analysis were performed by fiber-coupled optical spectrum analyzer (OSA). The characterization chapter overviews the performance evaluation of each proposed concept introduced in Chapter 2. Concepts are the uniform coupler grating, two dimensional splitting grating, 1-D Preamplifier/SOA arrays, and Preamplifier/2-D SOA arrays. For a performance analysis of the semiconductor devices and arrays, some basic parameters must first be obtained by testing conventional edge-emitting devices and GCSELs. For the epi-structure a standard characterization procedure of edge-emitters was performed to find the following parameters: inverse differential efficiency and internal absorption losses, modal gain and transparent current density. For the specifics of GCSELs, those parameters are free carrier absorption in the GaAs material, and grating outcoupling efficiency.

5.2 Edge-Emitters Standard Laser Diode Characterization

Since we were investigating the specific gain sections of variable stripe widths and lengths designed for this research, it is necessary to gain an understanding of processed devices. This is why the particular epi-structure was first characterized. This was done by measuring the standard light-current characteristics of several edge-emitting devices with varying lengths and a constant stripe width. The basic operating parameters estimated from testing are the threshold current, differential efficiency, wall-plug efficiency, and serial resistance.

$$Slope = \frac{dP}{dI} [\frac{W}{A}] \qquad\qquad 5.1$$

$$\frac{E_{ph}}{q} = E_{ph}[eV] = \frac{1.24}{\lambda[\mu m]} \qquad\qquad 5.2$$

$$\eta_d = \frac{Slope[\frac{W}{A}]}{E_{ph}[eV]}$$ 5.3

Where, P – optical power out, I – electrical driving current, E_{ph} is photon energy,

and η_d - differential quantum efficiency. The threshold current was defined and described

earlier in section 1.3. Wall plug efficiency is defined as the optical power output per

electrical power input for the laser device:

$$WPE = \frac{P}{IV}$$ 5.4

Serial resistance is defined as:

$$R_s = \frac{dV}{dI}[I > I_{th}]$$ 5.5

In the R&D environment, these parameters are obtained by detailed

statistical research with numerous devices. This research concentrates on the most

valuable parameters obtained for further discussion of multi-emitter sections. For this

purpose, Fabry-Perot (FP) sample devices were assembled and characterized based on the

cavity length and stripe widths. The L-I-V characteristic was recorded using continuous

wave pumping of the diodes.

(a)   (b)
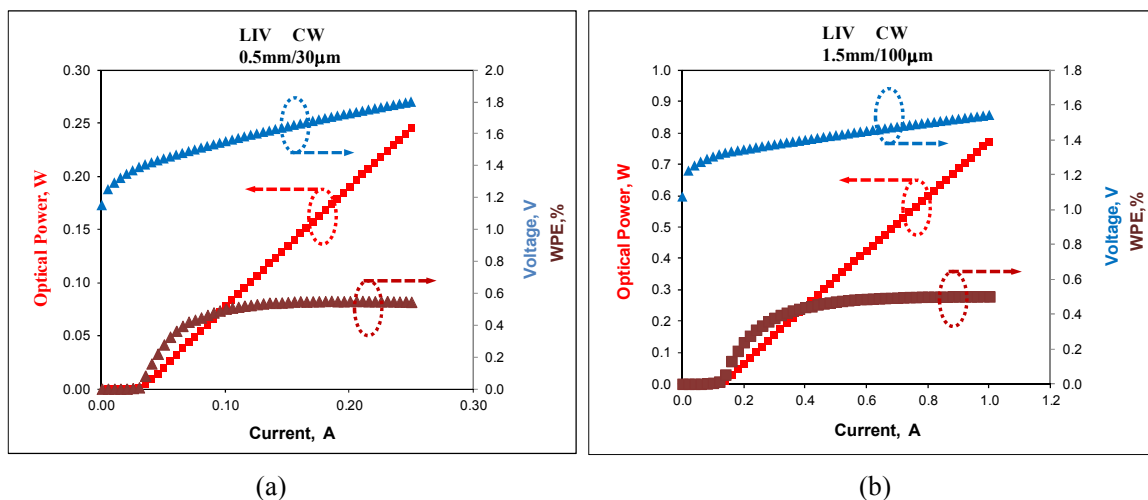
Figure 5.1 Total optical edge emitters L-I-V plot stripe of (a) 0.5mm long with 30μm stripe width, (b) 1.5mm long device with stripe width of 100μm

Figure 5.1 graphs demonstrate the total optical power-current-voltage performance plots of two sample stripe edge-emitters: 1.5mm long with 100μm stripe width and 0.5mm long with 30μm stripe width. The 30μm stripe device exhibited a total slope efficiency of 1.14 W/A, threshold current of 32.3 mA, and a total differential efficiency of 89.5% with a wall plug efficiency of 55%. The 100μm stripe device exhibited a total slope efficiency of 0.9 W/A, threshold current of 129.5 mA, and a total differential efficiency of 70.9% with a wall plug efficiency of 50%. The average serial resistance, defined by the slope of the voltage versus current, is approximately $R_s = 3 \cdot 10^{-4}$ Ω-cm^2. Further testing was performed on several devices with various active lengths of the semiconductor. A Summary of the tested devices' performances is presented in table 5.1.

Table 5.2 30μm and 100μm stripe widths edge-emitter's test data summary

Chip#	Units	#23-2(2)	#24-2	#24-3		#4-18F	#4-10F	#4-20F
					Device Specs			
Active Length	mm	0.50	1.00	2.00		1.00	1.50	2.00
Stripe Width	μm		30				100	
LIV & Spectral Summary								
Threshold current	mA	32.3	41.6	59.3		100.4	129.5	158.1
Threshold current density	kA/cm²	0.215	0.139	0.099		0.100	0.086	0.079
Total Slope	W/A	1.14	0.79	0.73		0.95	0.90	0.85
Total diff eff	%	89.5%	62.0%	57.6%		75.2%	70.9%	57.5%
Max WPE	%	55%	42%	41%		52%	50%	48%
Lasing wavelength	nm	973.8	978.1	978.0		977.6	978.8	980.5

The device operating parameters in table 5.1 were used to determine the differential quantum efficiency of the two stripe widths of 30 μm and 100 μm. Given the modal gain conditions as a sum of mirror losses and internal losses, the total output power leaving the laser facets, can be calculated as

$$P_{out} = \eta_d \frac{E_{ph}}{q}(I - I_{th})$$ 5.6

Here, the output power above the threshold is a linear function of the current. Rearranging equation 5.6 and solving for η_d:

$$\eta_d = \frac{q}{E_{ph}}\frac{dP}{dI} = \frac{(dP)/(E_{ph})}{(dI)/q}$$ 5.7

Here, η_d is the differential increase in photons per time divided by the differential increase in injected electrons per time. From the theory of laser diodes η_d in steady-state operation (above threshold) can be re-written to (Chapter 1.5):

$$\eta_d = \eta_i \frac{\alpha_m}{\alpha_i + \alpha_m} \qquad\qquad 5.8$$

The mirror losses, α_m can be estimated as

$$\alpha_m = \frac{1}{2L} \ln\left(\frac{1}{R_f^2}\right) \qquad\qquad 5.9$$

Where R_f is the mirror reflection and L is the cavity length. Now, the internal efficiency, η_i, and internal losses, α_i, can be estimated by taking the inverse of equation 5.8:

$$\frac{1}{\eta_d} = \frac{1}{\eta_i}\frac{\alpha_i + \alpha_m}{\alpha_m} = \frac{1}{\eta_i} + \frac{\alpha_i}{\eta_i \alpha_m} \qquad\qquad 5.10$$

Internal laser parameters such as the internal efficiency, η_i, and internal absorption losses, α_i, can be determined by plotting the inverse differential efficiencies. Figure 5.2 demonstrates plots of the differential efficiency with respect to cavity lengths. From the plot, it was determined that the internal efficiency of 30 μm wide stripe is 90% and the internal absorption is 3.6cm^{-1}, while the internal efficiency of 100 μm stripe is 85% and the internal absorption is 1.5cm^{-1}. In the narrower stripe width, internal absorption parameters are sufficiently higher due to an increased portion of the waveguide optical losses in the lateral direction. While for Broad Area stripe devices, i.e. ≥100μm wide stripes, optical losses are mostly in the transverse direction.
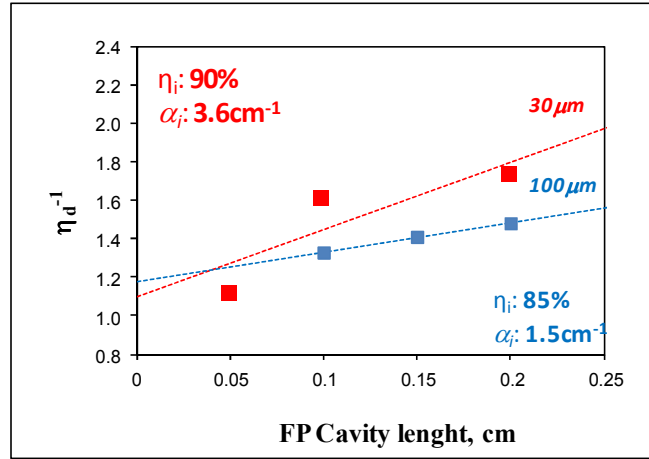
Figure 5.2 Inverse differential efficiency vs. cavity length. red is 30µm and blue is 100µm stripe widths

Modal gain parameter $g_m(n)$ is the modal optical gain provided by the product of the material gain, $g(n)$ and the optical confinement factor, Γ. Modal gain can also be estimated by threshold current analysis of the device where J_{th} and J_{tr} are threshold and transparent current densities, respectively.

$$\Gamma g_{th} = \Gamma g_0 \ln\left(\frac{J_{th}}{J_{tr}}\right) = \Gamma g_0 \ln(J_{th}) - \Gamma g_0 \ln(J_{tr}) \qquad 5.11$$

$$\Gamma g_{th} = \alpha_i + \alpha_m = \alpha_i + \frac{\ln\left(1/R\right)}{L} \qquad 5.12$$

Solving for $\ln(J_{th})$ from equations 5.11 and 5.12, gives

$$\ln(J_{th}) = \frac{\ln\left(1/R\right)}{\Gamma g_0}\frac{1}{L} + \left(\ln(J_{tr}) + \frac{\alpha_i}{\Gamma g_0}\right) = A\frac{1}{L} + B \qquad 5.13$$

Rearranging the equation in the linear form, $\ln(J_{th})$ becomes a function of the reciprocal cavity length. Based on the obtained parameters outlined in table 5.1 the slope, A, and intercept, B, can be found. Furthermore, these parameters can be used to find the modal gain and transparent current density. These parameters are necessary to verify that

the cavity length is enough to compensate for the losses as well as establish the transparent current density necessary for device pumping.

$$\Gamma g_0 = \frac{\ln\left(\frac{1}{R}\right)}{A}$$

5.14

$$\ln(J_{th}) = B - \frac{\alpha_i}{\Gamma g_0}$$

5.15

Figure 5.3 shows the linear plots described by equation 5.13 based on the parameters achieved earlier in table 5.1 and figure 5.2, α_i of 3.6 and 1.5 cm^{-1}, R=32%. Calculating modal gain and transparent current, we get J_{th}=58.8 A/cm^{2} and Γg_0=24 cm^{-1} for 100μm stripe device and J_{th}=67.6 A/cm^{2} and Γg_0=22.4 cm^{-1} for 30 μm stripe devices. Narrow-stripe emitters exhibit higher internal loss and enlarged transparent current density due to higher optical loss in lateral direction and carrier diffusion outside the stripe. This information is compatible to that achieved by other epi-structures and will be used in further sections of the characterization chapter.

(a)　　　　　　　　　　　(b)
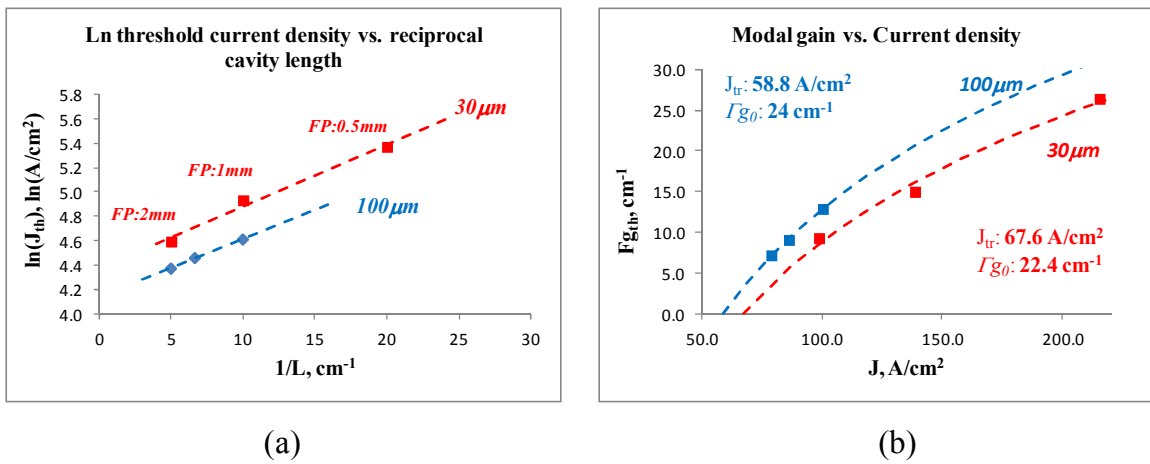
Figure 5.3 Modal Gain and Transparent current density calculation plots for 30μm and 100μm stripe devices. (a) Linear function plot of natural log of current density vs. reciprocal of the cavity length. (b) Modal gain vs. current density

5.3 Additional testing for GCSE characterization

5.3.1 Free-Carrier Absorption

Another important parameter of the GaAs semiconductor is free carrier absorption. For the wavelength outside the fundamental absorption band (less than approximately 800nm), light propagated through GaAs has an optical loss, which is related with free-carrier absorption. A simple experiment was performed to measure the absorption parameter, illustrated in figure 5.4(a). The losses were estimated using blank GaAs wafers of various thicknesses with surfaces polished to a mirror finish. The GaAs wafer used for the experiment has the same doping levels as the wafer with epi-grown layers. The following formula can be used for power transmission:

$$P_1 = P_0(1-R)^2 e^{-\alpha_{GaAs}d} \qquad\qquad 5.16$$

P_0 is the incident, P_1 is the transmitted optical powers, R is the surface reflection, d is wafer thickness, and α_{GaAs} is the unknown absorption. The transmission ratio is output power divided by total input power, so dividing both sides by P_0 and taking a natural logarithm of both sides, the equation becomes:

$$\ln\left(\frac{P_1}{P_0}\right) = \ln(T) = -\alpha_{GaAs}L + 2\ln(1-R) \qquad\qquad 5.17$$

By using the logarithmic function, a linear equation is achieved with free-carrier absorption being a slope and therefore R parameter becomes a not required value. Fig. 5.4 (b) shows plots natural log of transmitted power ratio vs. wafer length. This is a linear equation where the absorption coefficient is the slope, so plotting the linear equation and finding the slope comes to α_{GaAs} =8.5 cm^{-1}. This is an important parameter in estimating

grating outcoupler efficiency along with GCSELs with output light propagated through the GaAs wafer.

(a) (b)
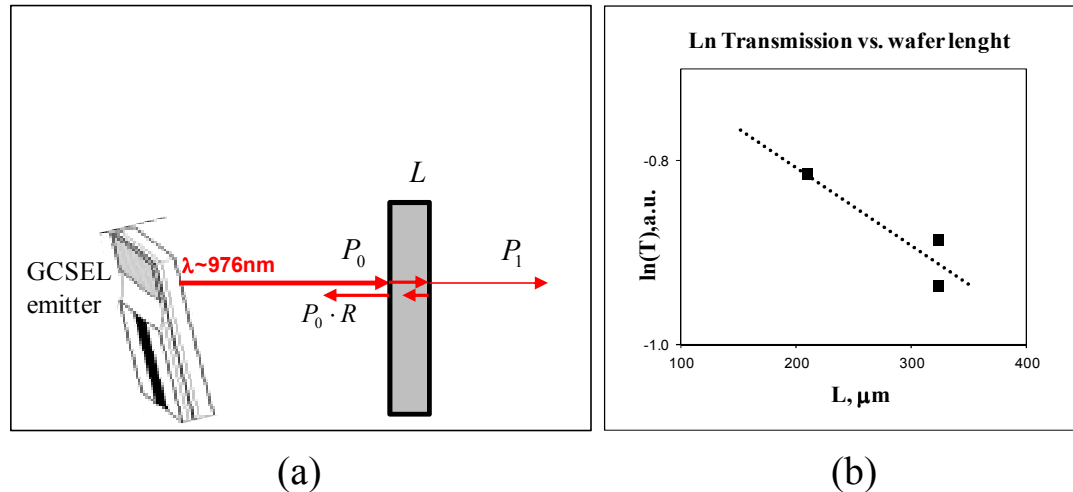
Figure 5.4 Optical transmission measurement by using a GCSEL emitter (a) Schematic of the experiment (b) Natural log of transmissions vs. GaAs wafer thickness

5.3.2 Grating reflectivity and Grating Efficiency

Along with the epi-performance characteristics, the grating outcoupler strength must also be experimentally measured. This parameter evaluation was done by an analysis of the optical output power characteristics measured from the GCSEL device. The GCSEL devices used in the experiments had one grating outcoupler, and the lasing cavity was formed by reflection from a cleaved facet and the effective reflection from the grating side as shown in Fig 5.5. Given the internal optical loss, internal quantum efficiency, active length section, and measurements obtained for the differential efficiency slope, the grating coupling efficiency can be estimated. For a GCSEL with a 2 mm-long active section, the optical output power from the grating and cleaved facet were measured. From the obtained L-I characteristics, the optical power ratio, ξ of total optical

output power from the grating, $P^{out}_{grating}$ to optical power output from the facet, P^{out}_{facet} taking in account of the absorption losses in the substrate, $e^{\alpha_{GaAs}d}$ was ~12.

$$\xi = \frac{P^{out}_{grating}e^{\alpha_{GaAs}d}}{P^{out}_{facet}} \cong 12 \qquad 5.18$$

To estimate the effective reflectivity from the grating side, depicted in figure 5.5, the ratio used an equation coming from the analysis of the cavity with two reflection values on each side:

$$\xi = \left(\frac{R_{facet}}{R^{eff}_{grat}}\right)^2 \left(\frac{1-R^{eff}_{grat}}{1-R_{facet}}\right) \qquad 5.19$$

Where ξ is the power ratio of grating output power and facet output power and facet reflection parameter for operating wavelength is known, $R_{facet} \approx 32\%$ for GaAs at $\lambda = 976nm$
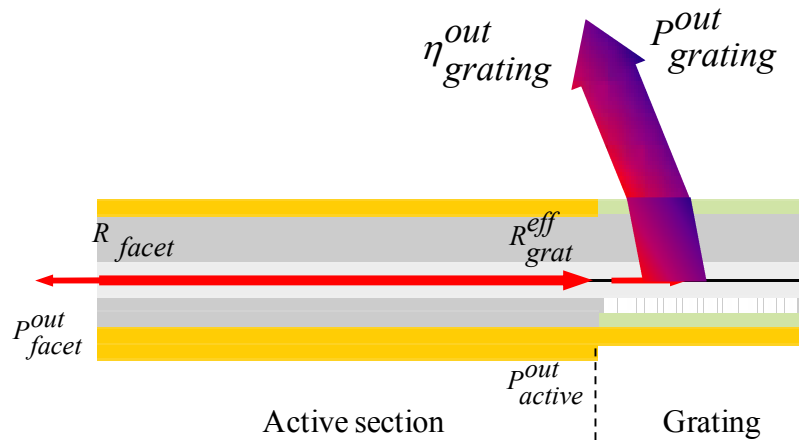
Figure 5.5: Broad-area GCSEL schematics with outline of facet and grating side reflections; facet and output powers

The Estimated effective reflectivity from the grating was $R^{eff}_{grat} \cong 0.46\%$. Knowing the internal optical loss, $\alpha_i = 1.5$ cm^{-1} and internal quantum efficiency,

$\eta_i = 85\%$, estimated from testing the broad area edge-emitters in section 5.2, the total differential efficiency can be calculated from:

$$\frac{1}{\eta_{active}} = \frac{1}{\eta_i} + \frac{2\alpha_i}{\eta_i \ln 1/(R_{facet}R_{grat}^{eff})} L \qquad 5.20$$

The total differential efficiency for a 2 mm long active section is then estimated to be η_{active}=78% (0.99W/A). The calculation of the corresponding grating output differential quantum efficiency is then:

$$\eta_{grat}^{estimated} = \eta_{active} \frac{\xi}{1+\xi} e^{-\alpha_{GaAs}d} \qquad 5.21$$

The evaluated differential efficiency for the grating output is then $\eta_{grat}^{estimated}$=63%. From the measured L-I-V curves output slope from the grating region was measured of 0.73W/A corresponding to $\eta_{grating}^{measured} = 57\%$. Therefore, the estimated grating outcoupling efficiency including the QW losses and the grating optical losses is:

$$\eta_{grat}^{out} = \frac{\eta_{grat}^{measured}}{\eta_{grat}^{estimated}} = \frac{57\%}{63\%} = 91\% \qquad 5.22$$

5.3.3 Near Field – grating outcoupling length

The Grating outcoupling length parameter, defined as 1/e falloff point, was evaluated from Near-Field analysis of the GCSEL's emitting area. Near-Field images were taken by Sony IR camera and recorded by Spiricon software. Extrapolating the intensity profile, a fit for $e^{-x/L}$ was performed and the estimated parameter was $L_{measured}^{out}$=110µm, which was close to that expected from the numerical modeling, section 3.2. Fig. 5.6 shows the fall-off plot of the intensity vs. longitudinal position with inserted near-field (NF) image of the reading.

NF Intensity Profile

$e^{-x/L}$

L=110 μm

Position, mm
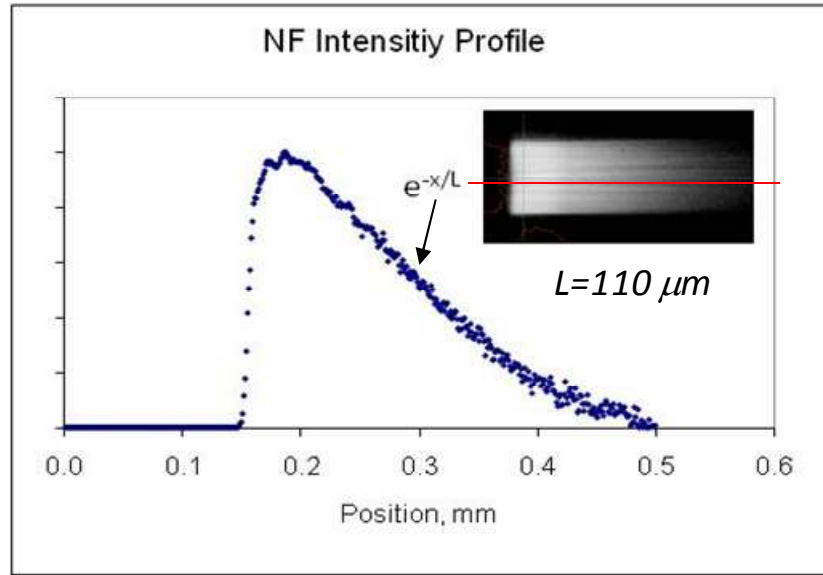
Figure 5.6: Broad-area GCSEL schematics with outline of reflections; facet and output powers

In the evaluation of the grating outcoupling length, the optical loss at the grating section should also be taken into account. An inverse of decaying energy across the emitting grating is defined

$$\alpha_{grat}^{out} = \frac{1}{L_{grat}^{out}} \qquad 5.23$$

Optical loss is then what plays a role in outcoupling efficiency, expressed in equation 5.24

$$\eta_{grat}^{out} = \frac{\alpha_{grat}^{out}}{\alpha_{grat}^{out} + \alpha_i + \alpha_{QW}} = 91\% \qquad 5.24$$

Where $\alpha_i + \alpha_{QW}$ is the total grating optical loss related to the waveguide loss and absorption in the unpumped QW. Overall power dissipation is defined as:

$$\alpha_{measured}^{out} = \alpha_{grat}^{out} + \alpha_i + \alpha_{QW} = \frac{1}{L_{measured}^{out}} \qquad 5.25$$

$$\frac{1}{L_{grat}^{out}} = \frac{\eta_{grat}^{out}}{L_{measured}^{out}} \qquad 5.26$$

The actual outcoupling length parameter is then estimated at 120μm, or:

$$L_{grat}^{out} = \frac{L_{measured}^{out}}{\eta_{grat}^{out}} = \frac{110\mu m}{0.91} = 120\mu m \qquad 5.27$$

5.4 Uniform Outcoupler Testing

Similar to standard GCSEL devices, a grating coupler with uniform profile was assembled and characterized. The device L-I-V performance was similar to that of a standard GCSEL with the same stripe width, shown in figure 5.7(a). Threshold values were the same while slope efficiency in the modified grating was dropped from 0.69W/A to 0.51W/A. That is mostly due to a shorter uniform grating, which length was 200μm versus 500 μm for the standard grating design. Fig. 5.7(b) shows the Near Field profile of the intensity distribution in of a 100μm stripe width with a standard outcoupling grating (top) and with a modified uniform output profile from outcoupling grating (bottom). To estimate the output power as a function of x (longitudinal direction), the following formulas were used.

$$P_{out} = P_{in} \frac{\Delta y}{w} \frac{\alpha_{out}}{\alpha_i + \alpha_{out}} (1 - e^{-(\alpha_i + \alpha_{out})\Delta x}) \qquad 5.28$$

$$P_{in}^x = P_{in}^{x-1} e^{-(\alpha_i + \alpha_{out})\Delta x} \qquad 5.29$$

From there, a table was constructed for the grating duty cycle vs. position (x) and written into the CAD file to be patterned on the e-beam. The longitudinal profile of the latter does not show a clear uniform output. That was because the design concentrated on the assumption that the etch-depth would be uniform, taking into consideration only Duty

Cycle vs. Outcoupling length given etch depth is 250nm. In reality, however, an effect called microloading must be taken into consideration. Chapter 2 described a modified version of the grating to be fabricated to achieve the "next-level" uniformity in the output.
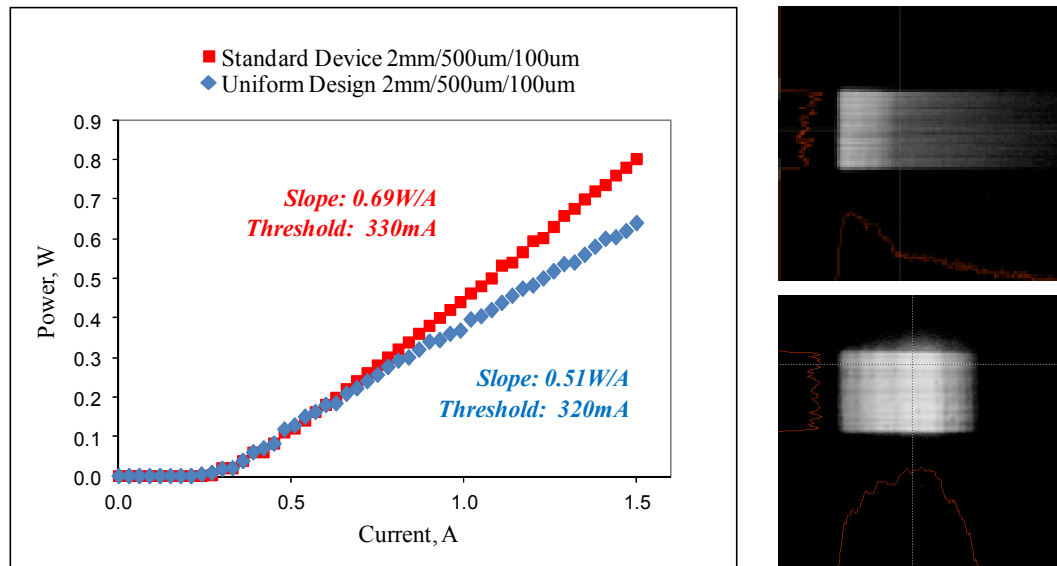
Figure 5.7 (a) Grating L-I comparison of two 100μm devices from same wafer; (b) Near Field of Standard GCSEL (c) Near Field of GCSEL with uniform grating design

5.5 2D Splitting Grating Outcoupling

The design of the two dimensional splitting grating was presented in Chapter 2.4. Gratings were e-beam patterned according to the design along with the rest of the processed devices lot. As shown in Fig. 5.8, an active gain section was surrounded by a standard grating outcoupler on one side and by an eight by eight sectioned grating splitter. A single section of the grating splitter patch has dimensions of 25 μm by 25 μm

with the total 2D grating outcoupler dimensions of 200 μm by 200 μm. The grating coupler on the other side of the gain section was used for the in-coupling of a beam from an external laser to achieve the best spectral and spatial properties of the beam outcoupled by the 2D splitter. A commercially available butterfly-packaged fiber-coupled laser was used as an external source operating at λ=976nm (Innovative Photonic Solutions, Inc.). Figure 5.8 (a) depicts a schematic of the device from p-side. Figure 5.8 (b) presents the experimental setup configuration used in this experiment. As illustrated, the light from the external source was coupled into the SOA waveguide using a mirror adjusted at the outcoupling angle. The external laser pumping current was driven at 50mA providing 8mW of output optical power. The Near- and Far-Field of the splitting grating output were investigated using Sony camera and a Spiricon frame grabber. The multi-spots beam from the 2D grating splitter was measured on a diffraction plane at a propagated distance of 35mm from the emitting area, still at the Fresnel range. The recorded images along with the obtained NF&FF profiles are presented in Chapter 2.4. Fig. 2.5 presents the achieved experimental results. The experimentally estimated outcoupling angles differ by ~2 degrees for the splitter's neighboring sections in both perpendicular directions, matching the design of the 2D splitter.

(a)

(b)
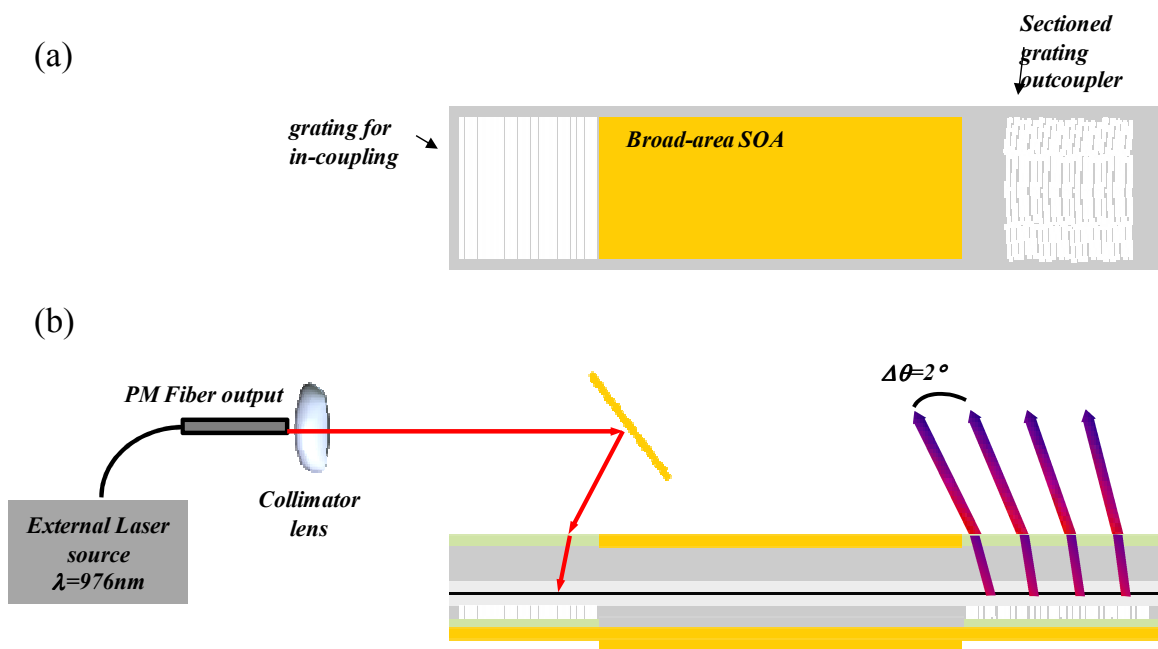
Figure 5.8. Experimental 2D multisection splitting grating (a) p-side schematic layout (b) experimental setup with external laser source and a cross-section schematic of the device

5.6 1D Array Testing, MOPA

5.6.1 The 1D Array Description and Experiment Setup

To extend the optical outcoupling field in the longitudinal direction, a 1D multi-emitter array device was designed based on the Master Oscillator Power Amplifier (MOPA) approach. The fabricated linear array consisted of a 2 mm-long Pre-Amplifier section and four 300 μm-long Semiconductor Optical Amplifiers (SOAs) spaced by grating outcouplers. The device layout is shown in Figure 5.9 (a). The active stripe width was of 30 μm and SOA length was chosen to be long enough to compensate for the absorption and outcoupling losses within a single element of the array. Outcoupling gratings with 260 nm periods detuned from the Bragg condition were patterned on each side of the SOA in the longitudinal direction. The Pre-Amplifier was coupled with a 50

μm long grating coupler on one side while SOA sections were surrounded with 30μm long grating outcouplers. A long grating outcoupler, on the side of entire array, along with an external mirror was used for wavelength locking of the Pre-Amplifier gain element. In this case, the Pre-Amplifier acted as a Master Oscillator (MO) providing a single line lasing while each SOA section acted as Power Amplifiers (PAs). Fig. 5.9 (a) presents a schematic of the assembled device with an external mirror aligned in the experimental setup. Fig. 5.9 (b) illustrates the device mounted onto a submount and holder with an external mirror aligned by a separate stage and Fig. 5.9 (c) shows the device in operation under low CW pumping conditions.
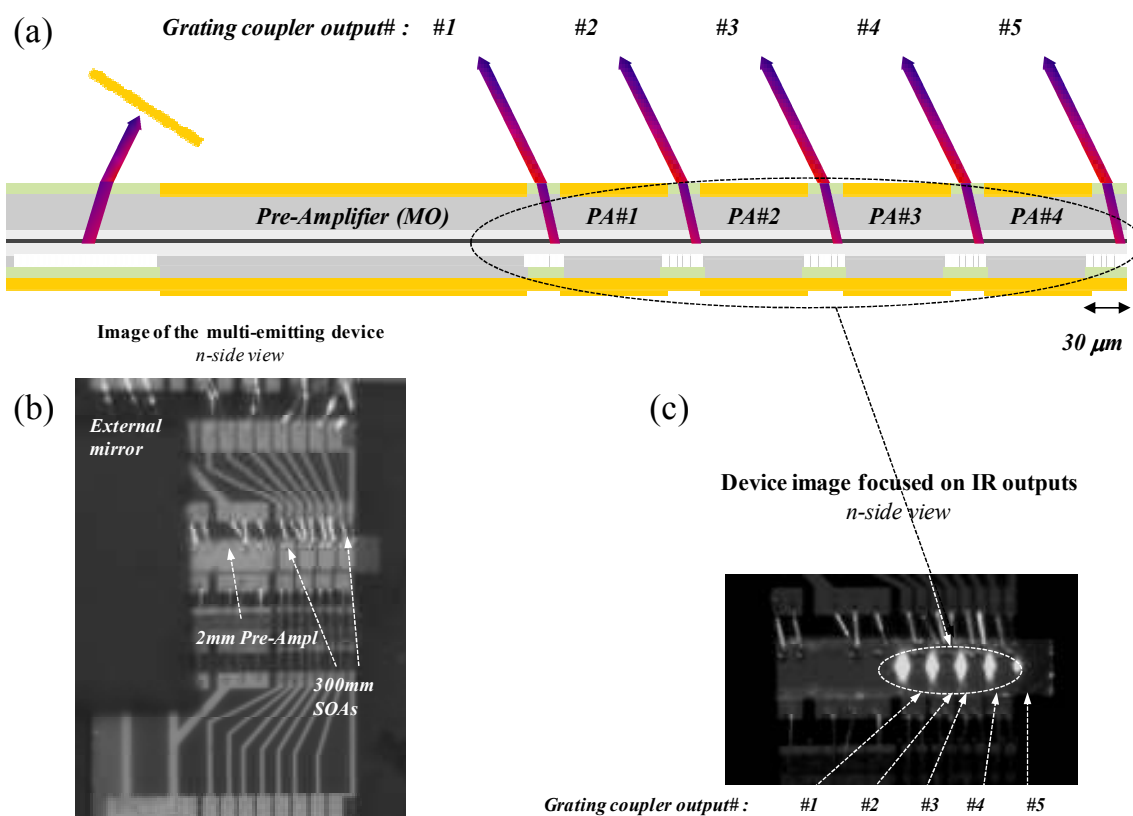
Figure 5.9. Illustration of a 1D MOPA array. (a) Schematic of a fabricated 1D array with Pre-Amplifier as the MO coupled with four PAs sections and grating outcouplers. (b) Actual device setup for experimental evaluation (c) Device in operation under low CW pumping

Alignment of the external mirror provided optical feedback through the grating into the Pre-Amplifier gain section. This external mirror reflector, along with a weak effective reflection from the grating outcoupler on the other side of the Pre-Amplifier, form a laser cavity for the MO. Figure 5.10 shows LIV plot measured from output #1, the 50 μm long outcoupler, while driving only the Pre-Amplifier section. The obtained characteristics look similar to those from a conventional diode laser with a threshold current of 125 mA, example in Table 5.1. For a driving current greater than the threshold, the emitting light has a single spectral line due to spectral selectivity of the external

reflection through the grating coupler. With an angular tilt of the external mirror of 24°, the emitting wavelength was λ=973.9 nm as shown in section 5.6.2, figure 5.11 (b) output #1.
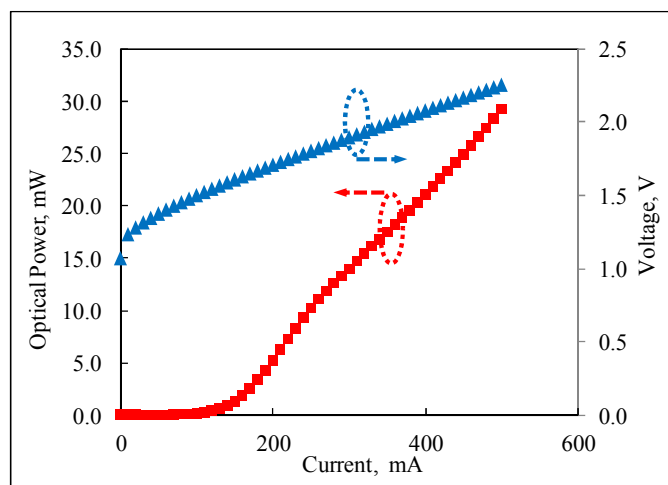
Figure 5.10 Measured L-I-V from output #1 in the 1D MOPA array with external optical feedback and electrical driving of the Pre-Amplifier only.

5.6.2 Separate electrical driving of the MO and the multiple PAs

For the proper operation and testing of the multi-emitter array of MO and the multiple PAs, separate driving of individual gain sections was applied. For this reason, a custom designed AlN submount was fabricated to match the p-side layout patterned contacts with the 1D MOPA array allowing p-side down bonding. After bonding the multi-emitter chip on the submount, the n-side contacts of each gain sections of the array were wired to separate current stand-offs, see image of the bonded device in Figure 5.9 (b). A Newport 8008 modular controller with multiple drivers was used for separate pumping of the MO and the PAs individually.

As in section 5.6.1, the device was wavelength stabilized using an external mirror feedback element. With the MO operation above the threshold, optical power

measurements were done for individual grating outputs of the 1D array with simultaneous driving the corresponding PA. By adjusting the driving current through each amplifier section, uniform optical power outputs were established. Figure 5.11(a) presents two cases for PAs driving conditions demonstrating the optical power distribution from each array outputs. An optical output variation less than 15% was achieved with a driving current of 195mA though the MO and 15mA for each PA. The observed variation of the optical power per individual outputs in the experiment was related to non-equal performance of the array's elements due to the fabrication quality of the narrow-stripe gain elements as well as the grating outcouplers. The averaged experimental data of the optical output power versus driving current through a single PA, while the MO is driven with a constant current, is presented in the Figure 5.13 (a) and discussed further in section 5.6.3.

Figure 5.11 presents the spectral plots measured from the five individual (#1-#5) outputs of the 1D MOPA array. Pumping conditions were of 195 mA for the MO and 15 mA of an individual PA. The lasing wavelengths measured from each grating outcoupler integrated with the PA (outputs# 2-5) match the lasing line of the MO (output#1). That fact is clear evidence of injection locking of the PAs as the light propagates from the MO section through the gain elements of the array.

(a)   (b)
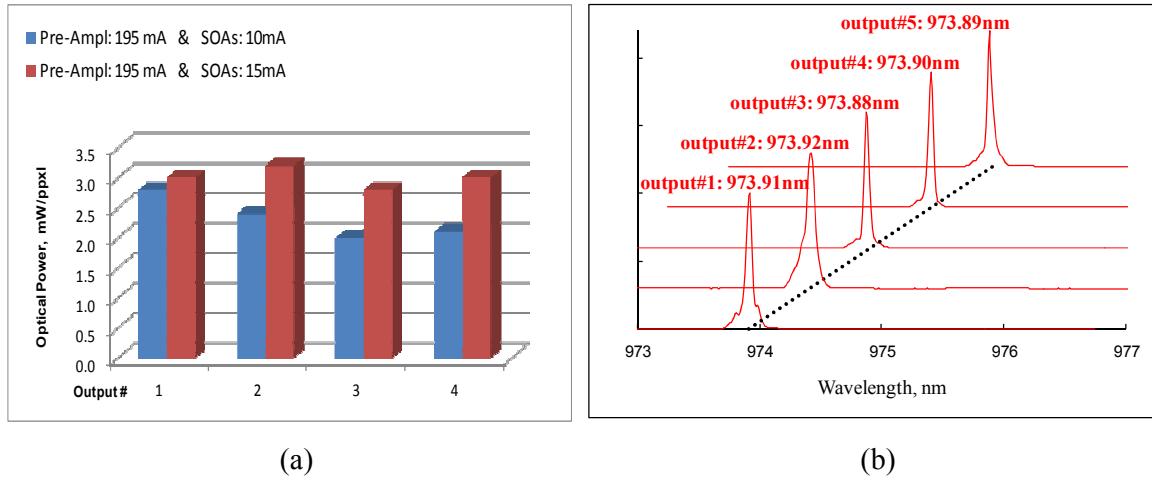
Figure 5.11 (a) Optical power distribution of the array's outputs for specified driving currents of the Pre-Amplifier (MO) & SOAs (PAs) (b) Normalized spectrum reading from each individual output (#1-#5) of 1D MOPA array.

5.6.3 Single Section PA/GCSE gain/loss analysis.

This section's emphasis is placed on the operational analysis of a single amplifier element of the 1D MOPA array. The gain/loss analysis is based on the power distribution of a single SOA section surrounded by grating outcouplers, the schematic of which is presented in Fig. 5.12. For the theoretical study, the following experimental data were used: the gain/loss epi parameters obtained from testing the 30 μm-wide stripe edge-emitters that is described in section 5.2; free-carrier absorption and grating quality parameters described in section 5.3.
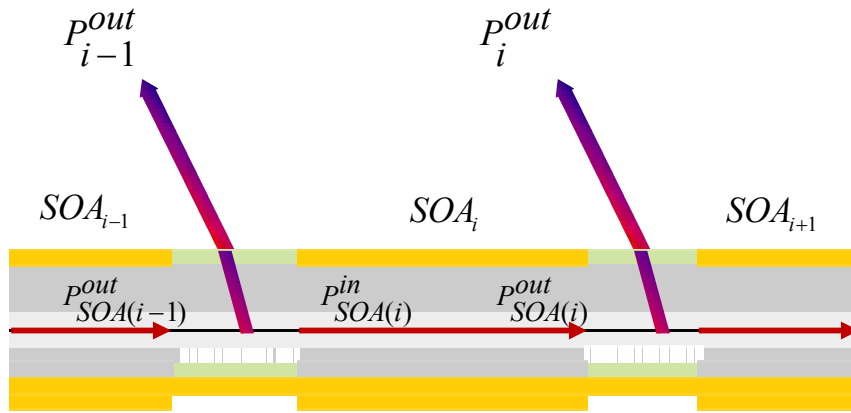
Figure 5.12 Single Section SOA/GCSE schematic for power amplification analysis

For estimating the outcoupling rate for the grating with a fixed length, the following equation was used:

$$\xi_{grat}^{outcoupl} = \eta_{grat}^{out}\left(1 - e^{-\left(L_{grat}/L_{grat}^{out}\right)}\right)$$

5.30

where $\eta_{grat}^{out} = 91\%$ is the grating outcoupling efficiency including QW loss and grating optical loss (section 5.3.2), $L_{grat}^{outcoupl} = 120$ µm grating outcoupling length parameter (section 5.3.3) and L_{grat} is the patterned length of the grating. With this data, the outcoupling rate, $\xi_{grat}^{outcoupl}$ for the 30 µm-long grating, L_{grat} is 20%. Taking in to account the free-carrier absorption in the 150µm-thick GaAs substrate with absorption loss parameter, of $\alpha_{GaAs} = 8.5$ cm^{-1} (section 5.3.1), and assuming no reflection from the n-side, the total output from the grating outcoupler comes to

$$\xi_{grat}^{OUTPUT} = \frac{P_i^{out}}{P_{SOA(i)}^{out}} = \xi_{grat}^{outcoupl} e^{-(\alpha_{GaAs} d_{GaAs})} \tag{5.31}$$

where P_i^{out} and $P_{SOA(i)}^{out}$ are output power from the coupler and output from SOA

gain section inside the waveguide, respectively, and d_{GaAs} is the thickness of the wafer.

From the schematic in Fig. 5.12, the general equation for the output power, P_i^{out}

propagated through the SOA_i gain section and outcoupled by the grating though the GaAs

substrate is

$$P_i^{out} = P_{SOA(i)}^{in} G_{SOA(i)} \xi_{grat}^{OUTPUT} \tag{5.32}$$

where $P_{SOA(i)}^{in}$ is the input power for SOA inside the waveguide and

$G_{SOA(i)} = \frac{P_{SOA}^{out}}{P_{SOA}^{in}} = e^{(\Gamma g - \alpha_i) L_{SOA}}$ is the SOA amplification factor. Here, $\Gamma g =$

$\Gamma g_0 ln \left(\frac{J_{SOA}}{J_{tr}} \right)$, SQW modal gain for the 30mm-wide stripe emitters is known $\Gamma g_0 =$

22.4 cm^{-1}, and transparent current density, J_{th}=67.6 A/cm^2 from section 5.2

Using equations 5.30 and 5.31 and the schematic on Figure 5.12, equations for

calculation the $P_{SOA(i)}^{in}$ power can be written as

$$P_{SOA(i-1)}^{out} = \frac{P_{(i-1)}^{out}}{\xi_{grat}^{OUTPUT}} \tag{5.33}$$

$$P_{SOA(i)}^{in} = P_{SOA(i-1)}^{out} \left(1 - \xi_{grat}^{outcoupl} \right) \tag{5.34}$$

Using the equations 5.32, 5.33 and 5.34, the relationship of the output power from

the grating coupler P_i^{out} can be established with the power from previous output P_{i-1}^{out} by

$$P_i^{out} = P_{(i-1)}^{out} \left(1 - \xi_{grat}^{outcoupl} \right) G_{SOA(i)} \tag{5.35}$$

Figure 5.13 (a) shows the data plots of the optical power output from single grating coupler versus the SOA driving current. The red line resulted from theoretical analysis of the SOA/GCSE operation by using equations 5.30-5.35 and applying the gain/loss parameters obtained in sections 5.2-5.3. Black markers represent the average experimental data achieved by taking the optical power readings from the individual outputs under the same SOA driving conditions as described in section 5.6.2.

The experimental results were fitted to theoretical data within standard error of the mean bars that evidences close match of the used operation analysis of a single element of 1D MOPA array along with gain/loss parameters used in calculation. Figure 5.13 (b) illustrates a power budget diagram for the optimal operating conditions of the SOA driven with current of 10 mA. The corresponding optical power output from the neighbored grating is 2.5 mW.
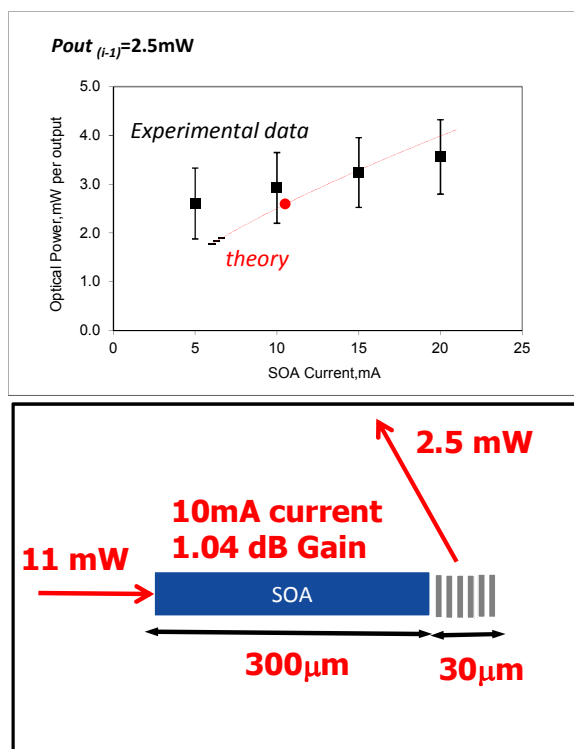
Figure 5.13 (a) Optical power outcoupled from the grating vs SOA driving current (theory and experiment) (b) Optical power budget diagram for the SOA operation condition market by red spot on left plot.

5.7 2D Array testing, MOPA

5.7.1 The 2D Array Description and Experimental Setup

Similar to the purpose of a 1D element, extending the optical in longitudinal field, a 2D MOPA based array device was designed and fabricated to extend the optical outcoupling field in the lateral direction. As shown in Fig.5.14 (a) the 2D multi-emitter consisted of a single 2mm-long Pre-Amplifier section with a 900 μm stripe width. Following the broad area Pre-Amplifier, multiple narrow stripe gain waveguides with a 2D array of the grating coupled emitters were fabricated. The 2D grating coupler emitter array is tilted at 18° to the stripe direction to increase the Fill-Factor (33%) of the gain waveguides after the Pre-Amplifier. This design allows 100 μm spacing between emitting

sections, while increasing individual SOA length to ~285 μm given stripe width of 8 μm. Gratings were patterned at a detuned 260nm period with in-coupler grating dimensions of 900x500 μm^2 and each GCSE element of 10x30 μm^2. Figure 5.14(a) illustrates the fabricated MOPA configuration, while fig. 5.14(b) shows the tilt of the 2D array allowing for (8x8) square array of emitters configuration and a SOA amplifier length increase.
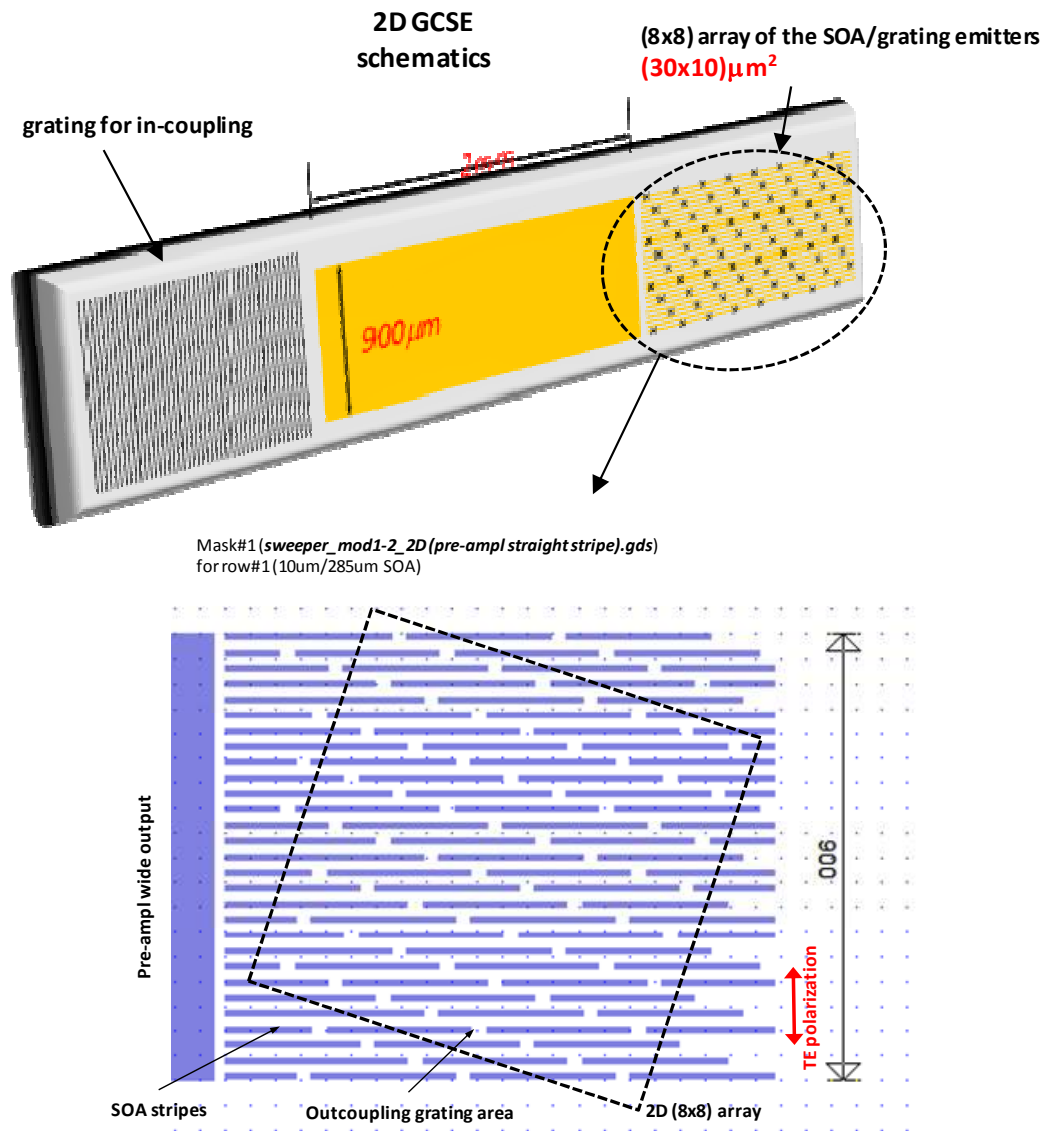
Figure 5.14 (a) Schematic of a 2D MOPA array device consisting of in-coupler grating, broad area Pre-Amplifier and two dimensional SOA/GCSE section. (b) Multiple waveguides schematics of the 2D emitters section.

For the experimental evaluation of the device performance, the 2D MOPA chip, cleaved from the processed wafer was bonded p-side down on an AlN submount with patterned contacts to allow separate driving of the Pre-Amplifier and 2D SOAs sections. Because of the extremely wide pre-amplifier section, the element is expected to lase with

multiple lateral modes applying wavelength stabilization by external mirror as was used for the MO of 1D array. Such multimode lasing of the MO will significantly reduce the mutual coherency of the 2D emitters, especially in the lateral direction. To improve the lateral coherence of the 2D emitters, the broad area amplifier was fed by a high quality beam from a commercial single-wavelength 976-nm-wavelength diode laser (Innovative Photonic Solutions, Inc.). The laser provided a lasing line at 976nm and a narrow spectral bandwidth of 0.04nm. The output from the single-mode fiber was collimated using a microscope objective lens for a 1 mm diameter beam, followed by a cylindrical lens f = 15 mm to shape the beam in the longitudinal direction. The focused beam size was measured at 1 mm in lateral and 200 μm in longitudinal direction on the plane close to the in-coupling grating of the 2D array chip. As shown in figure 5.15, the focused beam was directed on the chip's input area with the mirror by adjusting the in-coupling angle. This optical scheme was not ideal in obtaining high in-coupling efficiency of the external beam into the Pre-Amplifier waveguide. The optimization routine is described in section 5.8. As it will be shown later, the portion of the in-coupled light was ~5% so a high driving current equal to or greater than 4 A for the Pre-Amplifier to obtain a mW-scale output from single emitter of the 2D array was required. To prevent a thermal roll-over of the emitting characteristics, both the Pre-Amplifier and the 2D SOA sections were driven with short electrical pulses using two PCX-7410 Quasi-CW Laser Diode Drivers synchronized with each other while operating. External beam in-coupling was applied through the mirror and grating coupler, the Pre-Amplifier was wavelength locked and all 2D MOPA array components were operated under the following driving currents:

external laser at 100mA (CW), Pre-Amplifier at 4A (500nsec 50kHz pulse) and 2D SOAs at 2A (500nsec 50kHz pulse).
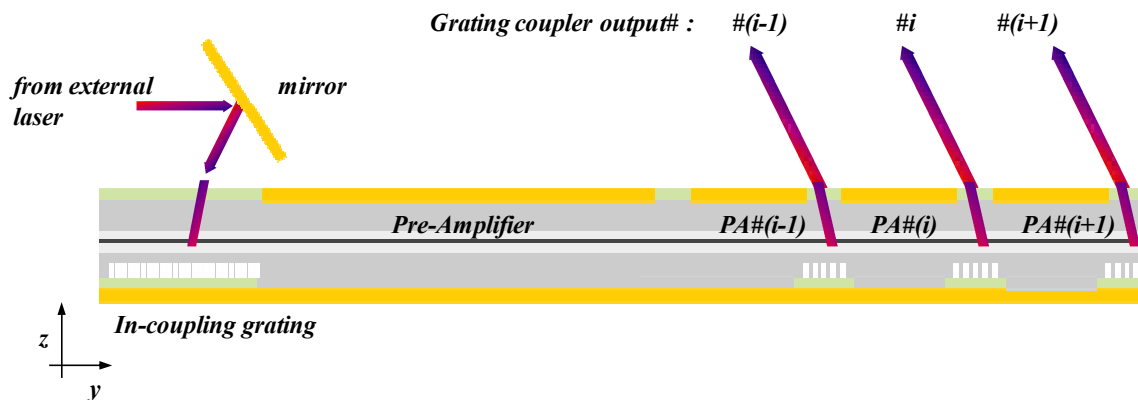
Figure 5.15 Experimental setup of the

The Optical Spectral Analyzer (OSA) was used with the optical fiber input; an 100 μm core diameter fiber with an FC connector was used in the experiments. The cleaved bare end of the fiber was aligned to the three randomly selected outputs at 2D array sections matching lateral and longitudinal directions. Figure 5.16 shows the spectral plots measured from the selected emitters as well as from the external laser. The measured spectral line from the single emitter matches with the other spectral lines measured directly from the external laser. This is clear evidence of spectral locking of the 2D emitters.
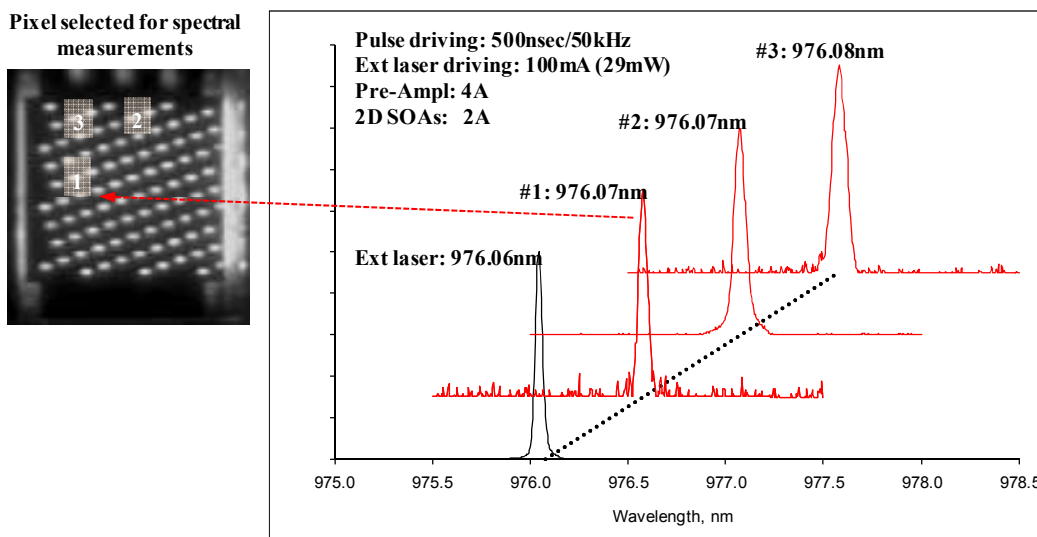
Figure 5.16 Normalized spectral measurements from the selected outputs shown on the left (1,2,3) with respect to lasing from the external laser source.

5.7.2 2D MOPA Array Test data and optical link budget for array's components

The 2D array with the external laser operating as the MO was tested with combined driving conditions – CW and pulsed, as described in the section 5.7.1. Figure 5.17 (a) illustrates the L-I characteristics of the optical power output obtained from the 2D section, normalized to the individual pixel. The external laser was pumped at a constant current of 100mA, while the pre-amplifier section was chosen to operate at 2 A, 4 A, and 6 A 500 ns/50 kHz Quasi-CW pumping. A two dimensional PA array was driven with a source synchronized to the pre-amplifier. The measured results show that an individual pixel optical power output of 0.3 mW/pixel may be achieved prior to thermal roll-over. The total power output was also studied in terms of L-I by sweeping pumping of the external laser, depicted in figure 5.17 (b). Again, the pre-amplifier and PAs were set at constant synchronized pulse currents of 4A and 1A respectively. The L-I

performance demonstrates individual optical pixel power saturating in the neighborhood of 0.3 mW/pixel. These pumping conditions were used to optimize the operating currents of the laser source, Pre-Amplifier, and the 2D PA array for the study of the coherence strength between the selected pixels. These interference results were discussed in Chapter 2.8
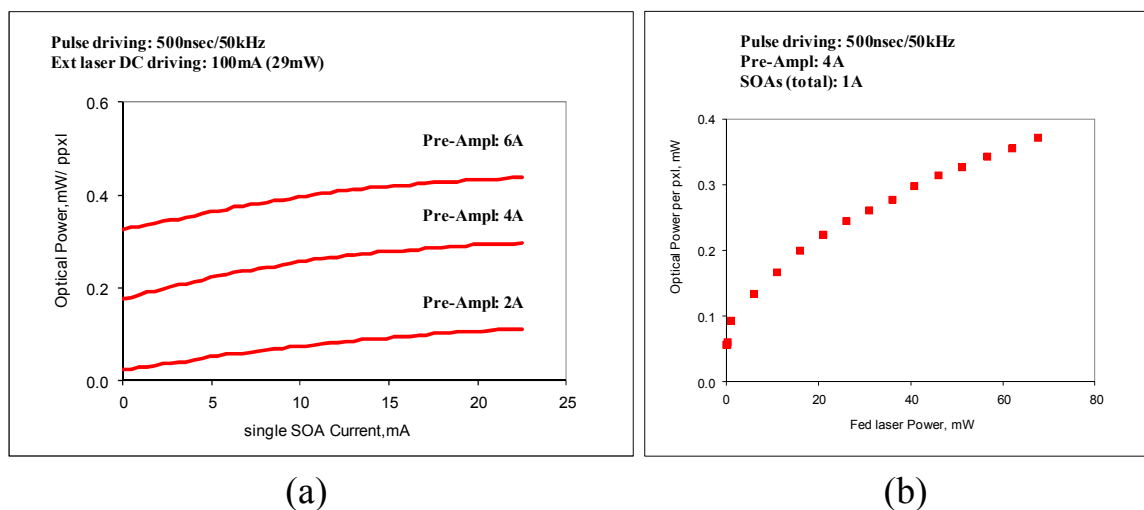
Figure 5.17 2D MOPA array characterization: (a) Averaged optical power output from single emitter vs. single PA driving current for different Pre-Ampl driving; (b) Averaged single emitter output vs. External Laser power for fixed driving the 2D array chip.

From the LI characteristics obtained in figure 5.17 and the basic semiconductor properties measured in this chapter, an optical budget link can be evaluated. There are several factors that were not optimized in this evaluation and therefore only an estimate of the optical budget can be performed. This is due to a smaller stripe width used for the power amplifier section and so the modal gain and losses are different from that of in 1D array. Also, some discrepancies in the PA amplification factor estimation may occur because of the operation in pulse pumping conditions. The external beam optical in-coupling did not operate at optimal conditions; optimization of which will be discussed

further in section 5.8. The improved beam coupling efficiency from ~5% by a factor of ten to ~50% will lead to the reduced Pre-Amplifier driving currents and allow operation of the devices in continuous wave (CW) condition. Following the basic approach described in section 5.6.3, a rough estimation of the optical link budget for the components of the 2D MOPA array was performed.

Figure 5.18 shows the budget link diagram for the seeded laser with a pre-amplifier and a single SOA section. The figure gives an optical gain/loss power budget to achieve a 1mW optical output from an individual pixel in the array. For this condition, the operating currents chosen are 40mW for the external laser source, 4A for the pre-amplifier section, and 1A for the 2D PA section. This gives a current distribution to the individual SOA in the PA of 8mA. In summary, due to high in-coupling loss (~15dB), high current pumping is required for power loss compensation. To improve the device performance, further in-coupling optimization should be implemented. Section 5.8 explains those experiments and their corresponding results.
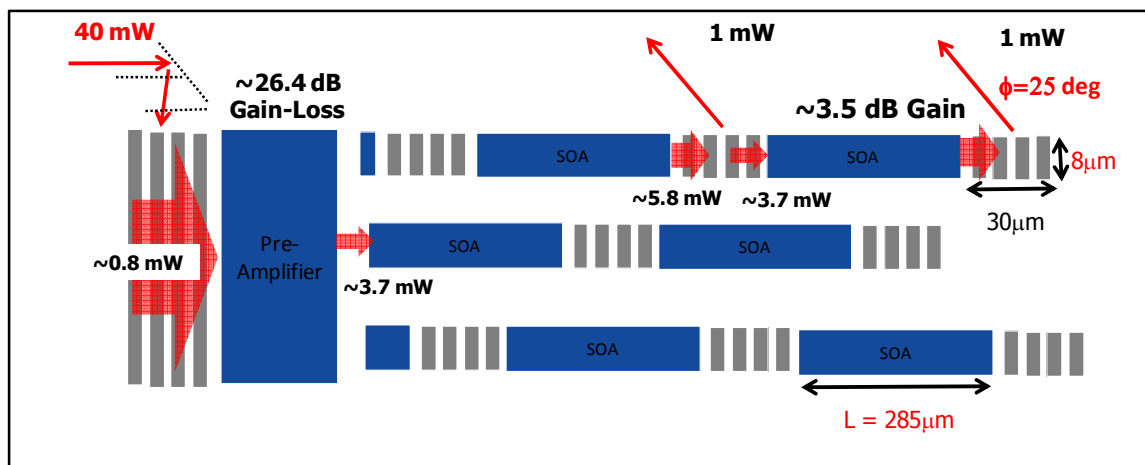
Figure 5.18 Rough optical power budget is done for one operation point, see on the right. Gain&loss parameters for narrow-stripe SOAs are estimated assuming constant lateral carrier diffusion;

Figure 5.19 (a) shows the assembled device on the AlN submount, and the device under low current operation is depicted in Figure 5.19 (b). Figure 5.19 (c) shows the optical power distribution of the individual coupler elements with the intensity parameters measured and normalized to the highest intensity. The intensity variation shows a pixel-to-pixel variation of less than ±20%.
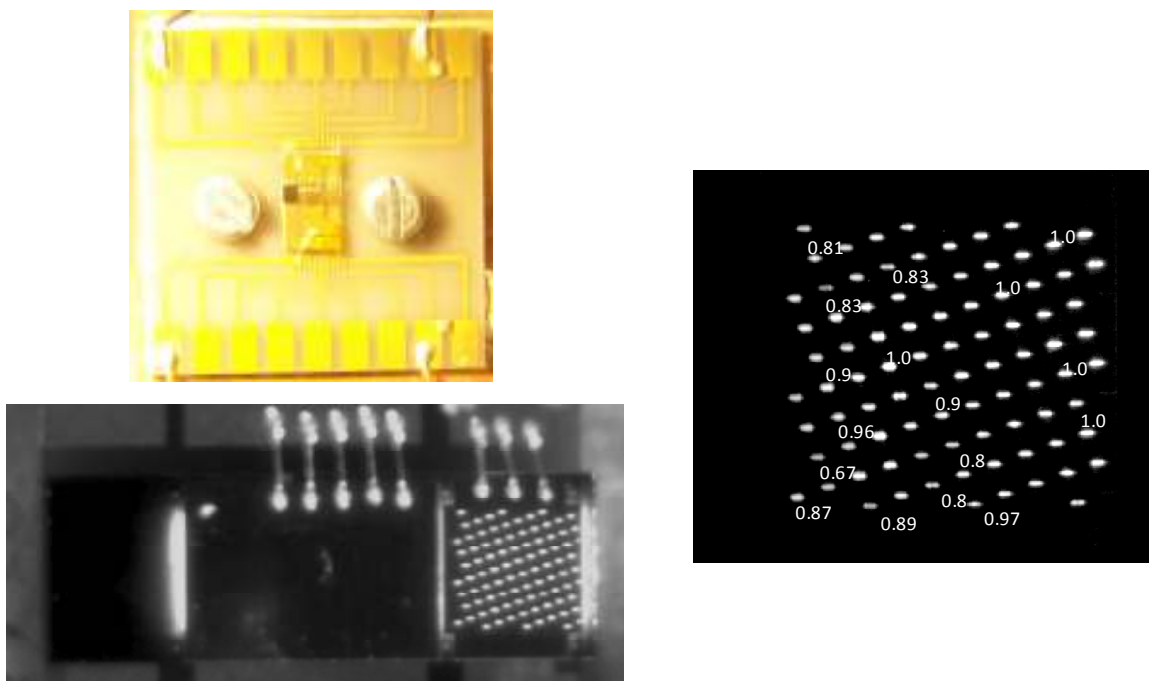
Figure 5.19. (a) Pre-Amplifier 2D GCSE assembly on AlN submount (b) device in operation under low pumping conditions (c) Intensity distribution within the 2D SOA array under uniform pumping (Pixel-to-pixel intensity variation: <20%)

5.8 In-Coupling Improvement Experiment

Efficient coupling of the external beam in a broad area pre-amplifier waveguide is a nontrivial task. This is due to a narrow spectral bandwidth, the acceptance angle of the coupling grating is very small since grating dispersion is

$$D = \frac{d\theta}{d\lambda} = \frac{m}{nd \cos(\theta)} \qquad\qquad 5.36$$

Where, n is the refractive index of the substrate, d is the grating period, and θ is the incidence angle and m – order. The refractive index from chapter 3.1 is $n = 3.317$, $m = 1$ $d = 260$ nm, $\theta = 24°$. The dispersion parameter is calculated to be relatively small, of $D \cong 0.001$ rad/nm. Therefore the acceptance angle of the grating is very small, in the order of 0.3°. To match the acceptance angle, for a 5mm diameter beam, the focusing distance to achieve such small angle is estimated at ~450 mm.

The input beam to the grating coupler must match the device stripe and grating coupling length parameters. Those are 900 μm by 120 μm in an elliptical shape. Two cylindrical lenses must then be used to focus in x and y direction. To compensate for the acceptance angle, a large focal length must be chosen for the longitudinal focusing, providing a small divergence angle.

To evaluate in-coupling efficiency, the chip with the in-coupling grating must be identical to those used for the 2D-array device, and was fabricated especially for this experiment. A chip consisting of a 900 mm stripe width and the same grating coupler as in Section 5.7.1 was used for the in-coupling. Proper focusing parameters should be obtained to achieve high in-coupling efficiency into the waveguide. This effort is required to reduce the driving current though the 2D-array pre-amplifier which will allow a CW operation of the pre-amplifier and SOA's (PA's). To achieve a focusing spot with a small angle in the longitudinal direction, a lens with long focal length is required. It is estimated that a focal length to match the acceptance angle should be ~450 mm or greater. Fig. 5.20 shows an experimental setup schematic for phase and beam shape

matching to in-coupling grating incorporating three different lenses. A 5x microscope lens was used to collimate a beam with a 5 mm diameter spot followed by two cylindrical lenses of f=500mm and f=50mm to focus the beam in the longitudinal and lateral dimensions, respectively. The established beam size was focused to 1mm in the lateral and 200um in the longitudinal direction, with a divergence angle of ~0.4° to compensate for the grating acceptance angle. Figure 5.21 depicts an image of actual setup performed on an optical table.
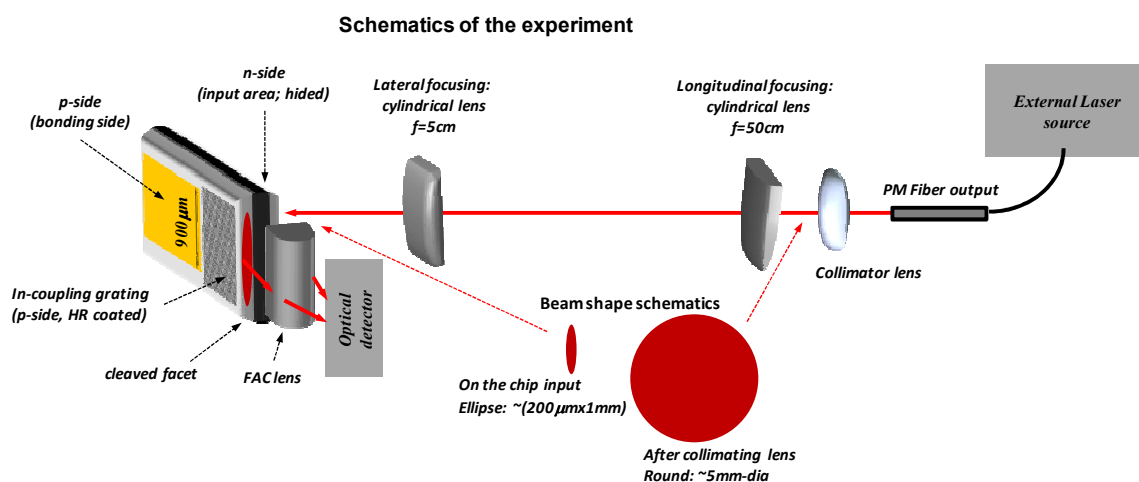
Figure 5.20. Advanced setup for improving coupling-in efficiency.
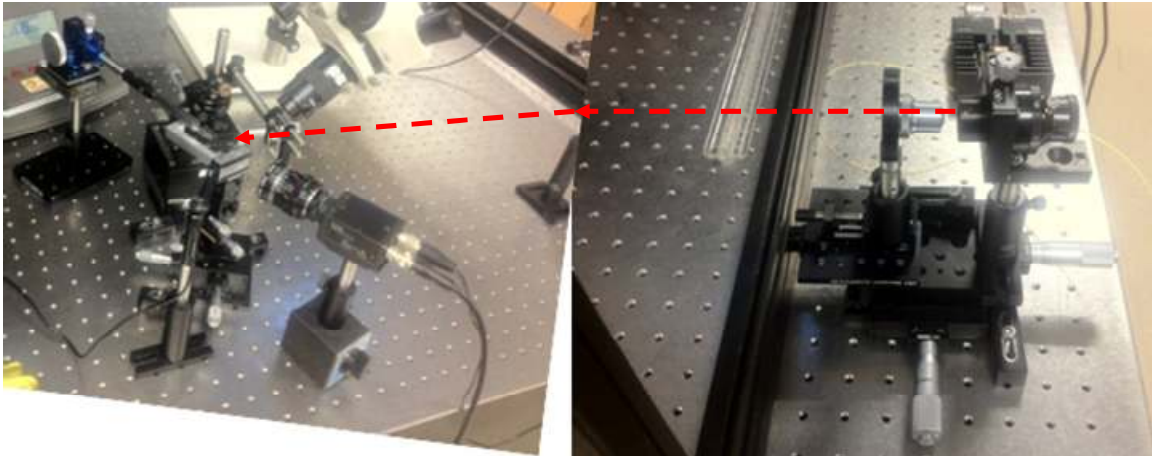
Figure 5.21Actual Image of the experimental setup with collimated 5mm diameter input source (right image), two cylindrical focusing lenses and a 900µm stripe device for testing

Optical power measurements from the facet, marked as cleaved facet in figure 5.20, were performed after proper alignment of the system components. Table 5.2 provides a summary of the optical power measured given the current pumping conditions of the external laser, 100 mA, 150 mA and 190 mA. The grating in-coupling efficiency calculation was performed given the reflection, wafer absorption, facet reflection, and beam edge clipping. The general efficiency formula can be expressed as

$$\eta_{grating}^{in} = \frac{P_{WG}^{in}}{P_{grat}^{in}} = \frac{P_{facet}^{out}\big/(1 - R_{GaAs})}{P_{laser}^{out}(1 - \alpha_{ellipse})(1 - R_{GaAs})(1 - \alpha_{GaAs}^{loss})} \qquad 5.37$$

The free-carrier absorption due to the GaAs substrate, $\alpha_{GaAs} = 8.5$ cm^{-1}, leads to a $\alpha_{GaAs}^{loss} = 12\%$ substrate loss. The reflection from the input surface, R_{GaAs} (n-side of GaAs) is 32%; the mirror reflection, R_{GaAs} from the cleaved facet is 32%. Also, there is a lateral focusing clipping factor due to the over sizing of the elliptical beam measured by

cutting off 1mm effective device width from the beam at the same location $\alpha_{cut-off} =$

9%.

Table 5.3 Coupling efficiency to the grating coupler using External Laser source with
collimating and focusing lenses

External Laser		Facet output Power	Calculated Coupling IN Efficiency
Drive current	Optical Power		
mA	mW	mW	
100	35	6.5	50.1%
150	63	11.9	51.5%
190	80	15.0	51.3%
		Averaged:	51.0%

Figure 5.22 presents an illustration of the power distribution prior outcoupling

from the facet. In-coupling efficiency of ~5% was estimated for the initial testing

performed in section 5.7 for the 2D-array performance. A 50% efficiency (10X increase)

of optical coupling into the waveguide was achieved by optimizing the optical coupling

optics. The optical system described in this section can be further employed for the 2D

array. Improved in-coupling efficiency will allow CW operation of the pre-amplifier and

SOA sections for high optical powers. Significant improvements in the interference

pattern experiment from described in chapter 2.8 can lead in clearer fringe patterns for

further mutual coherency analysis.
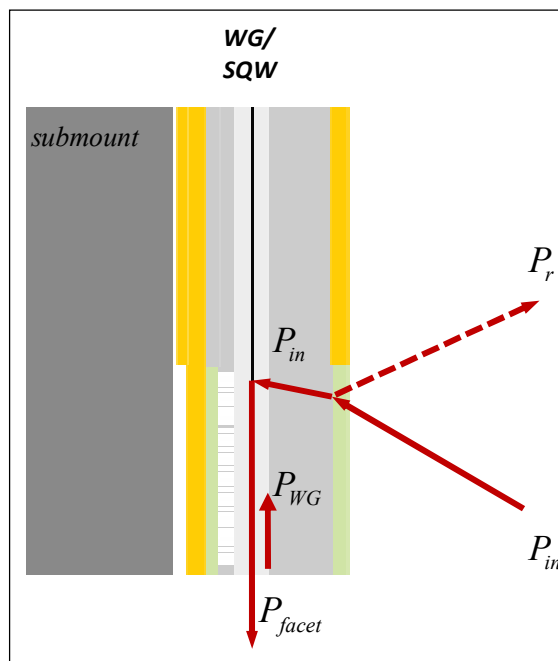
Figure 5.22. Schematic of in-coupling experiment with reflections and transmission parameters.

CHAPTER 6: CONCLUSION

The scope of this defense covered topics on grating coupled surface emitters with several implementations. Monolithic integration of the in-plane broad area active section with grating couplers detuned from Bragg condition provided minimal residual optical feedback significantly broadening the applications of semiconductor-based light emitters. Different novel designs of the grating as an optical component were developed and experimentally evaluated. Wavelength selection and stabilization was performed by incorporating integrated grating couplers with external elements, such as a feedback mirror and a high quality fiber coupled light source. Near field and far field properties of the GCSEL were studied in terms of variations of the grating outcoupler parameters: periodicity, duty cycle, etch depth, and groove angle tilt.

Using e-beam pattering and RIE etching, duty cycle and etch depth parameters were spatially varied, controlling the intensity distribution in the near field (NF). The detailed analysis of a device design for intensity distribution in a longitudinal direction was performed and novel device designs for a uniform and a bell-shaped intensity distribution in the near field were found. A practical example of a device with a smooth variation of the grating duty cycle in the longitudinal direction was fabricated and compared to that of the standard grating outcoupler. The microloading effect, associated with the proposed method of the NF control, was experimentally investigated in detail.

By applying a variation of the grating periodicity and groove tilt angles, a novel design was introduced for optical splitting using grating couplers integrated with broad

area active sections. This work introduced a multi-sectioned grating design along with an experimental evaluation of the concept. An 8x8 array of 25x25 μm^2 grating pixels were designed to distribute the optical output in lateral and longitudinal directions with a ±2° spread. The concept device was fabricated and tested demonstrating a good agreement between the measured experimental results and the designed optical output features.

Furthermore, grating couplers can be utilized in multi-dimensional array applications. The 1D and 2D arrays implementing a long pre-amplifier section and distributed power amplifiers spaced by grating couplers are suitable for wavelength and phase locking of multiple emitters in both the lateral and longitudinal directions. The concept was based on the use of one master oscillator (MO) component common between multiple power-amplifier/grating pairs. As a result of the performed research, phase-locked multi-emitter sources based on a MOPA array approach and surface-emission provided by grating outcouplers have been experimentally demonstrated. A high degree of coherence was achieved from 1D-array outputs in the longitudinal direction and the coherence has been experimentally evaluated by measuring the high fringe visibility of the interference pattern from the selected output pairs.

In the scope of the MOPA array study, a 2D phase-locked multi-emitter incorporating a single MO and the 2D array of the PAs/Gratings was also designed and experimentally evaluated. The study consisted of selecting several arbitrary outputs from two dimensions – lateral and longitudinal. This experiment demonstrated and observed the coherence between emitters located in different lateral waveguides of the 2D MOPA array. The quantitative analysis was compromised by weak beam in-coupling efficiency leading to low optical intensity from the individual outputs. A separate experiment

aiming to maximize the optical in-coupling from an external laser source was performed demonstrating the achieved efficiency of 50% with an optimal optical scheme. The measured results show a pathway to improved design of the 2D MOPA array with higher output power characteristics.

Future research would involve optimization of the structure to increase the output power from the individual emitters. For example, introduce an improved master oscillator active section incorporating a grating coupler designed to match the external laser source; this would lead to an improved electrical link budget. The 2D PA/grating section can also be improved by extending the amplification section dimensions resulting in an increase in the optical power from the emitters. In addition, optimization of the structural parameters of the gratings will increase their outcoupling efficiency. These concepts can be applied to different wavelength regimes though scaling of the structural parameters of the MO, PAs, and grating outcouplers depending on application requirements.

REFERENCES

Zh. I. Alferov, D. Z. Garbuzov, V. S. Grigor'eva, Yu. V. Zhilyaev, L. V. Kradinova, V. I. Korol'kov, E. P. Morozov, O. A. Ninua, E. L. Portnoi, V. D. Prochukhan, and M. K. Trukan, Fiz. Tverd. Tela ~Leningrad! **9**, 279 (1967) [Sov. Phys. Solid State **9**, 208 (1967)]

Zh. I. Alferov, V. M. Andreev, D. Z. Garbuzov, Yu. V. Zhilyaev, E. P. Morozov, E. L. Portnoi, and V. G. Trofim, Fiz. Tekh. Poluprovodn. **4**, 1826 (1970) [Sov. Phys. Semicond. **4**, 1573 (1970)]

Zh. I. Alferov, V. M. Andreev, R. F. Kazarinov, E. L. Portnoi, and R. A. Suris, Inventor's Certificate No. 392875 [in Russian], Application No. 1677436, priority as of July 19, 1971.

G. A. Antipas, R. L. Moon, L. W. James, J. Edgecumbe, and R. L. Bell, *Institute of Physics Conference Series*, No. 17 (IOP Publ., Bristol, 1973), p. 48.

Bates K. A., Li L., Roncone R. L., and Burke J. J., "Gaussian beams from variable groove depth grating couplers in planar waveguides," Appl. Optics, 32(12), 2112–2116 (1993).

O'Brien S., Welch D. F., Parke R. A., Mehuys D., Dzurko K., Lang R. J., Waarts R., and Scifres D., *"Operating Characteristics of a High-Power Monolithically Integrated Flared Amplifier Master Oscillator Power Amplifier,"* IEEE J. of Quant. Elec., vol. 29, pp. 2052-2057, June 1993

Burnham R., ScifresD., and Streifer W., IEEE J. Quant. Electron., Vol. 11, p. 439, (1975)

N. W. Carlson, V. J. Masin, M. Lurie, B. Goldstein, and G. A. Evans, "Measurement of the coherence of a single-mode phase-locked diode laser array," *Applied Physics Letters*, vol. 51, pp. 643-645, 1987.

N.W. Carlson, J.H. Abeles, D.P. Bour, S.K. Liew, W.F. Reichert, P.S.D. Lin, A.S. Gozdz, , "Demonstration of monolithic, grating-surface-emitting laser master oscillator-cascaded power amplifier array," *IEEE Photon. Technol. Lett.*, vol. 2, no. 10, pp. 708–710, Oct. 1990.

Chi M., Jensen O. B., Holm J., Pedersen C., Andersen P. E., Erbert G., Sumpf B., and Petersen P. M., *"Tunable high-power narrow-linewidth semiconductor laser based on an external-cavity tapered amplifier,"* Opt. Expr., vol. 13, pp. 10589-10596, Dec. 2005

Coldren L.A., Corzine S.W., *Diode Lasers and Photonic Intergrated Circuits*. Wiley-Interscience, 1995

J. O'Daniel, O. Smolski, M. Moharam, and E. Johnson, "Integrated wavelength stabilization of in-plane semiconductor lasers by use of a dual-grating reflector," Opt. Lett. 31, 211-213 (2006).

O'Daniel "Intergrated wavelength stabilization of broad area semiconductor lasers using a dual grating reflector" PhD Dissertation, CREOL, The College of Optics and Photonics, 2006

R. Diehl, Topics in Applied Physics, High-Power Diode-Laser Fundamentals, Technology, Applications, 78 ed: Springer-Verlag, Berlin, 2000.

G.A. Evans, D.P. Bour, N.W. Carlson, R. Amantea, J.M. Hammer, H. Lee, M. Lurie, R.C. Lai, P.F. Pelka, R.E. Farkas, J.B. Kirk, S.K. Liew, W.F. Reichert, C.A. Wang, H.K. Choi, J.N. Walpole, J.K. Butler, W.F. Ferguson, Jr., R.K. DeFreez, M. Felisky, , "Characteristics of coherent two-dimensional grating surface emitting diode laser arrays during CW operation," *IEEE J. Quantum Electron*., vol. 27, no. 6, pp. 1594–1608, June 1991.

Dzurko K. M., Hardy A., Scifres D. R., Welch D. F., Waarts R. G., and Lang R. J., *"Distributed Bragg Reflector Ring Oscillators: A Large Aperture Source of High Single-Mode Optical Power,"* IEEE J. of Quant. Elec., vol. 29, pp. 1895-1905, June 1993

Evans G. M. and Hammer J. M., Survace Emitting Semiconductor Lasers and Arrays, (Academic Press, Inc., 1993) San Diego, CA, Ch. 4, 5.

T. Y. Fan, "Laser Beam Combining for High-Power, High-Radiance Sources," *IEEE J. Sel. Topics Quantum Electron*., vol. 11, no. 3, pp. 567–577, May/June 2005.

J. W. Goodman, "Introduction to Fourier Optics", 2nd ed., McGraw-Hill, New York, 1996.

Hagberg M., Eriksson N., and Larsson A., "High efficiency surface emitting lasers using blazed grating outcouplers," Applied Physics Letters, vol. 67, pp. 3685-3687, 1995.

Hall, Robert N.; G. E. Fenner, J. D. Kingsley, T. J. Soltys, and R. O. Carlson (November 1962). "Coherent Light Emission From GaAs Junctions". Physical Review Letters 9 (9): 366–368. Bibcode 1962PhRvL...9..366H. doi:10.1103/PhysRevLett.9.366.

Hayashi, M. B. Panish, P. W. Foy, and S. Sumski, Appl. Phys. Lett. 17, 109 (1970)
Zh. I. Alferov, V. M. Andreev, S. G. Konnikov, V. G. Nikitin, and D. N. Tret'yakov, in *Proceedings of the International Conference on the Physics and Chemistry of Semiconductor Heterojunctions and Layer Structures*, Budapest, October, 1970, Vol. 1, edited by G. Szigeti (Acade´miai Kiado´, Budapest, 1971), p. 93.

Higuchi M., Journal of the Electrochemical Society, Vol. 136, p. 2710, 1989.

Kawano K. and Kitho T., *Introduction to Optical Waveguide Analysis: Solving Maxwell's equation and the Schrodinger equation*. Wiley-Interscience, 2001.

Kristj´ansson, S., Li, M., Eriksson, N., Hagberg, M., Killius, K.-J., and Larsson, A., "Circular grating coupled DBR laser with integrated focusing outcoupler," IEEE Photon. Technol. Lett. 9, 416–418 (1997).

Kristj´ansson, S., Eriksson, N., Modh, P., and Larsson, A., "Surface-Emitting Tapered Unstable Resonator Laser with Integrated Focusing Grating Coupler," IEEE Photon. Technol. Lett. 12(10), 1319–1321 (2000).

Li, M., Bengtsson, J., Hagberg, M., Larsson, A., and Suhara, T., "Off-plane computer-generated waveguide hologram", IEEE J. of Sel. Top. in Quantum Electronics 2(2), 226-235 (1996).

L. J. Mawst, D. Boetz, M. Jansen, C. Zmudzinski, S. S. Ou, M. Sergant, C. A. Tu, T. J. Roth, G. Peterson, M. Valley, and J. J. Yang, "Two-Dimensional Surface-Emitting Leaky-Wave Coupled Laser Arrays," *IEEE J. Quantum Electron.*, vol. 29, no. 6, pp. 1906–1917, June 1993.

Miller, M.; Grabherr, M.; Jager, R.; Ebeling, K.J.; , "High-power VCSEL arrays for emission in the watt regime at room temperature," Photonics Technology Letters, IEEE , vol.13, no.3, pp.173-175, Mar 2001

Miyanaga, S., and Asakura, T., "Intensity profile of outgoing beams from uniform and linearly tapered grating couplers," Appl. Optics, 20(4), 688–695 (1981).

Modh, P., Backlund, J., Eriksson, N., Bengtsson, J., Kristjánsson, S., and Larsson, A., "Effects of feedback from collimating, focusing, and spot-array generating outcoupler gratings in surface-emitting semiconductor lasers", Opt. Lett. 27(8), 574-576 (2002).

Modh, P., Backlund, J., Bengtsson, J., Larsson, A., Shimada, N., and Suhara, T., "Multifunctional gratings for surface-emitting lasers: design and implementation", Appl. Opt. 42(24), 4847-4854 (2003)

Nathan, Marshall I.; Dumke, William P.; Burns, Gerald; Dill, Frederick H.; Lasher, Gordon (1962). "Stimulated Emission of Radiation from GaAs p-n Junctions". Applied Physics Letters 1 (3): 62. Bibcode 1962ApPhL...1...62N. doi:10.1063/1.1777371.

J. S . Osinski, D. Mehuys, D. F. Welch, K. M. Dzurko, and R. J. Lang, "Laser Beam Combining for High-Power, High-Radiance Sources," *IEEE Photon. Technol. Lett.*, vol. 6, no. 10, pp. 1185–1187, Oct. 1994.

Paschke K., Güther R., Fricke J., Bugge F., Erbert G., and Tränkle G., *"High power and high spectral brightness in 1060nm α-DFB lasers with long resonators,"* Elec. Lett., vol. 39, pp. 369-370, Feb. 2003

Smolski, O.V.; O'Daniel, J.K.; Johnson, E.G.; , "Compact Vertically Stacked Master Oscillator Power Amplifier Based on Grating Coupled Laser Diodes," *Photonics Technology Letters, IEEE* , vol.18, no.18, pp.1931-1933, Sept.15, 2006

Smolski, O., Smolski, V., Yilmaz, Y., and Johnson, E., "Modal Control of Broad Area Semiconductor Laser with Monolithically Integrated Feedback Gratings" OSA Integrated Photonics Research, Silicon and Nanophotonics (IPRSN) Techn. Digest Paper: JTuB16 (2010)

O. V. Smolski, V. O. Smolski, E. C. Browy, E. G. Johnson, Z. A. Shellenbarger, "Design and experimental study on the grating outcouplers providing the controlled 2D-intensity profile of the output beam from a broad area laser diode" in *Proc. SPIE* vol. 8267, p. 826712, Feb. 2012.

Soda H., Iga K., Kitahara C., and Suematsu Y., *Japan Journal of Applied Physics*, vol. 18, pp. 2329, 1979
Stelmakh, N.; Flowers, M.;, "Measurement of spatial modes of broad-area diode lasers with 1-GHz resolution grating spectrometer," *Photonics Technology Letters, IEEE* , vol.18, no.15, pp.1618-1620, Aug. 2006

Touam, T., and Najafi, S., "Symmetric profile beams from waveguides with asymmetric grating couplers," Appl. Optics, 36(12), 2554–2558 (1997).

Tsang, w. T.: 'Extremely low threshold (AlGa)As graded-index waveguide separate-confinement heterostructure lasers grown by molecular beam epitaxy', *ibid.,* 1982, 40, pp. 217-219

L. Vaissié, W. Mohammed, and E. Johnson, "Monolithic integration of dual-layer optics into broad-area semiconductorlaser diodes," Opt. Lett. 28, 651-653 (2003).

Vassie "Monolithic integration of dual optical elements on high power semiconductor lasers" PhD Dissertation, CREOL, The College of Optics and Photonics, 2004

Vaissié, L., Smolski, O., Mehta, A., and Johnson, E., "High efficiency surface-emitting laser with subwavelength antireflection structure," IEEE Photon. Technol. Lett., 17(4), 732–734 (2005).

L. Vaissié, O. Smolski, E. Johnson, "Crossed-beam superluminescent diode," *Opt. Lett*., vol. 30, no. 13, pp. 1608–1610, 2005.

D.F. Welch, D. Mehuys, R. Parke, R. Waarts, D. Scifres, W. Streifer, "Coherent operation of monolithically integrated master oscillator amplifiers," *Electron. Lett.*, vol. 26, no. 17, pp. 1327–1329, Aug. 1990.

D. FL Wight, J. M. Heaton, B. T. Hughes, J. C. H. Birbeck, K. P. Hilton, and D. J. Taylor, "Novel phased array optical scanning device implemented using GaAs/AlGaAs technology," *Appl. Phys. Lett.*, vol. 59, no. 8, pp. 899–577, Aug. 1991.

Yilmaz, Y.O.; Smolski, O.V.; Smolski, V.O.; Johnson, E.G.; , "Spectral stabilization of external dual grating reflector coupled surface emitter array," *IEEE Photonics Society, 2010 23rd Annual Meeting of the* , vol., no., pp.700-701, 7-11 Nov. 2010

Yilmaz, Y.O.; Smolski, O.V.; Smolski, V.O.; Lockerman, J.K.; Johnson, E.G.; , "2-D Stacked External Cavity Multiwavelength Surface-Emitting Laser Array," *Photonics Technology Letters, IEEE* , vol.23, no.5, pp.323-325, March1, 2011